FEDERAL UNIVERSITY OF TECHNOLOGY – PARANÁ
GRADUATE SCHOOL OF ELECTRICAL ENGINEERING AND APPLIED COMPUTER
SCIENCE

ROBERSON ASSIS DE OLIVEIRA

CHARACTERIZATION AND NEW APPLICATIONS OF THE ACOUSTO-OPTIC EFFECT IN FIBER GRATINGS

THESIS

CURITIBA
2011

ROBERSON ASSIS DE OLIVEIRA

CHARACTERIZATION AND NEW APPLICATIONS OF THE ACOUSTO-OPTIC EFFECT IN FIBER GRATINGS

Thesis submitted to the Graduate School of Electrical Engineering and Applied Computer Science of the Federal University of Technology – Parana, as requisite for obtaining the degree of "Doctor of Science" - Area of concentration: Telematics.

Supervisor: Prof. Dr. Alexandre de Almeida Prado Pohl

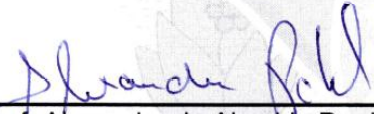**Co-supervisor:** Prof. Dr. Jucélio Tomás Pereira (UFPR)

CURITIBA
2011

Título da Tese Nº. 66

"Caracterização e Novas Aplicações do Efeito Acusto-óptico em Redes a Fibra"

por

Roberson Assis de Oliveira

Esta tese foi apresentada como requisito parcial à obtenção do título de Doutor EM CIÊNCIAS – Área de Concentração: Telemática, pelo Programa de Pós-Graduação em Engenharia Elétrica e Informática Industrial – CPGEI – da Universidade Tecnológica Federal do Paraná – UTFPR – Campus Curitiba, às 09h30min do dia 27 de maio de 2011. O trabalho foi aprovado pela Banca Examinadora, composta pelos professores:

Prof. Alexandre de Almeida Prado Pohl, Dr.
(Presidente – UTFPR)

Prof. Murilo Araújo Romero, Dr.
(USP)

Prof. Marcos Antonio Ruggiéri Franco, Dr.
(IEAv)

Prof. Aleksander Sade Paterno, Dr.
(UDESC)

Prof. Cícero Martelli, Dr.
(UTFPR)

Prof. Joaquim Miguel Maia, Dr.
(UTFPR)

Visto da coordenação:

Prof. Fábio Kurt Schneider, Dr.
(Coordenador do CPGEI)

To my beloved parents, Nadir and Terezinha, and my brother Moab

ACKNOWLEDGMENTS

All things work together for the good of those who love God…

Todas as coisas contribuem para o bem daqueles que amam a Deus…

Romans 8:28

RESUMO

OLIVEIRA, Roberson Assis de. Caracterização e novas aplicações do efeito acusto-óptico em redes a fibra. 180 f. Tese de Doutorado – Programa de Pós-Graduação em Engenharia Elétrica e Informática Industrial, Universidade Tecnológica Federal do Paraná. Curitiba, 2011.

Neste trabalho, os fundamentos da modulação acusto-óptica em redes de difração são apresentados. Através de uma análise detalhada dos modos de excitação mecânicos, mostrou-se que dois tipos predominantes de excitação acústica podem ser encontrados na fibra óptica dependendo da frequência acústica aplicada. Através da caracterização do modulador acusto-óptico, foi possível desenvolver novas aplicações, dentre as quais pode-se citar um dispositivo de inserção e retirada de canais em links ópticos cuja velocidade de chaveamento é uma das maiores apresentadas até agora na literatura, um compensador de dispersão sintonizável de banda estreita, um filtro óptico baseado na modulação acusto-óptica de uma rede de Bragg com uma diferença de fase, um novo método para controlar a escrita de redes de Bragg durante o processo de gravação utilizando-se da técnica da máscara de fase e um sensor de viscosidade, cuja aplicação pode ser considerada a mais promissora.

Palavras-chave: Modulação acusto-óptica. Redes de Bragg em fibra. Redes de período longo. Dispositivos sintonizáveis a fibra óptica. Sensor de viscosidade.

ABSTRACT

OLIVEIRA, Roberson Assis de. Characterization and new applications of the acousto-optic effect in fiber gratings. 180 f. PhD Thesis - Graduate School of Electrical Engineering and Applied Computer Science, Federal University of Technology – Parana, Curitiba, 2011.

In this work, the fundamentals of the acousto-optic modulation in diffraction gratings are presented. By means of a detailed analysis of the mechanical excitation modes applied to the modulator set, it was noticed that two predominant modes of acoustic excitation can be found in the optical fiber depending on the applied acoustic frequency. Through this characterization, it was possible to develop new applications, such as a fast acousto-optic add-drop multiplexing for optical channels, which produces one of the fastest switching device presented in the literature, a narrow tunable single channel dispersion compensator, a tunable optical filter based on the acousto-optic modulation of a phase-shifted fiber Bragg grating, a new method to control the spectrum of Bragg gratings during the writing process and a viscosity sensor, whose application can be considered the most promising.

Keywords: Acousto-optic modulation. Fiber Bragg gratings. Long period grating. Tunable all-fiber devices. Viscosity sensor.

LIST OF FIGURES

LIST OF TABLES

LIST OF ABREVIATIONS

ADM	Add-Drop Multiplexer
AMM	Assumed Modes Method
AOM	Acousto-Optic Modulator
AO-ADM	Acousto-Optic Add-Drop Multiplexer
AOSLM	Acousto-Optic Superlattice Modulator
ASE	Amplified Spontaneous Emission
AWG	Arrayed Waveguide Gratings
BG-AOM	Bragg Grating Acousto-Optic Modulator
CFRP	Carbon Fiber-Reinforced Polymer
EDFA	Erbium Doped Fiber Amplifier
EFPI	Extrinsic Fabry-Perot Interferometer
FBG	Fiber Bragg Grating
FEM	Finite Element Method
FLRDS	Fiber-Loop Ring-Down Spectroscopy
F-P	Fabry-Perot
GDR	Group Delay Ripple
LPG	Long Period Grating
ONA	Optical Network Analyzer
OSA	Optical Spectrum Analyzer
PS-FBG	Phase-Shifted Fiber Bragg Grating
PZT	Piezoelectric Transducer
RF	Radio Frequency
SMF	Single Mode Fiber
SSMF	Standard Single Mode Fiber
TMM	Transfer Matrix Method
UV	Ultra Violet
WDM	Wavelength Division Multiplexing

LIST OF SYMBOLS

$[C_6H_{12}O_6]$	Glucose concentration
$\{f(t)\}$	Generalized excitation vector
A	Area
a	Fiber cladding radius
C	Grating modulation depth
c	Speed of light in vacuum
c_{ext}	Speed of extensional mechanical waves in silica
D	Dispersion coefficient
d	Dispersion parameter
d_f	Fiber diameter
d_{PZT}	PZT diameter
d_{sh}	Silica horn base diameter
d_{sht}	Silica horn tip diameter
e	Local node
E	Young's modulus
f	Acoustic frequency
f_s	Flexural acoustic wave frequency
J_n	Bessel function coefficients
$\mathbf{K}$	Stiffness matrix
k_s	Acoustic wave number
L_i	Interaction length
l_g	Gratings length
L_b	Intermodal beat length
LP_{0m}	Cladding modes
l_{sh}	Silica horn length
l_t	Total length of the AOM
$\mathbf{M}$	Mass matrix
n	Refractive index
n_{eff}	Effective refractive index
p	Acoustic wave propagation phase
$P(t)$	External excitation
p_e	Strain-optic coefficient
p_{ij}	Components of the strain optic tensor
P_s	Acoustic power
q_j	Generalized coordinates
s	LPG sensitivities to the external media refractive indexes
S_η	Viscosity sensitivity
t	Time
$t_=$	Bar transmission
t_{GDR}	Group delay ripple coefficient
T^m	Minimum transmission of LPG at λ_m
t_{PZT}	PZT thick
t_s	Switching time
t_x	Cross transmission
u	Displacement

u	Nodal displacement vector
u_∞	mth root of the Bessel function
v	Grating contrast
V_{PZT}	PZT load
α_{neff}	Thermo-optic coefficient
α_Λ	Thermal expansion coefficient
δn_0	"dc" index change
$\Delta\beta$	Phase difference
$\Delta\varphi$	Phase shift
ε	Longitudinal strain
ζ	Reflected amplitude
$\hat\zeta$	Reflected power
η	Viscosity
ϑ	"ac" coupling coefficient
θ	Phase
Θ	Temperature
κ_m	Coupling coefficient for the mth cladding mode
λ	Wavelength
λ_B	Bragg wavelength
λ_{BS}	FBG switched wavelength generated by acoustic wave
λ_D	Design wavelength
λ_m	Dip wavelength
λ_s	Acoustic wavelength
Λ	Bragg grating pitch
Λ_{pm}	Phase mask pitch
ξ	Detuning
o	Thermal-optic coefficient
ϖ	Optical frequency
ρ	Density
σ	Poisson's ratio
ς	Wavelength-tuning rate
$\hat\tau$	Transmitted power
τ	Transmitted amplitude
τ_f	Fall time
τ_r	Transition time
τ_s	Full relaxation time
υ_{gs}	Acoustic group velocity
$\phi(z)$	Grating chirp
$\varphi(z)$	Trial or assumed modes function
χ	Stress-optical coefficient
ψ	"dc" coupling coefficient
$\hat\psi$	General "dc" self-coupling coefficient
ω	Harmonic load frequency
ω_s	Angular frequency

SUMMARY

1   INTRODUCTION

One of the most challenging issues for scientists is to understand the nature, and through numerical methods, reproduce and/or predict physical phenomena. Hopefully, with the development of computational capabilities, in the near future, it will be possible to study complex systems quite accurately without any expensive experimental setup. Additionally, the ability of using proven technology to construct new devices is also a challenge. Thus, the interaction between simulation and experimentation approaches together with the development of new ideas emerges as the most promising field of science.

1.1   MOTIVATION

The development of the optical fiber technology allowed scientists to develop long haul telecommunications links as well as construct various all-fiber devices, such as filters, switches, modulators, among others. These devices were built particularly for data transfer applications, using the technology of the wavelength division multiplexing (WDM). However, the range of optical fiber application is not restricted only to telecommunications, but also to a vast area of photonics, including lasers, sensing and medical sciences.

The possibility of writing diffraction gratings in optical fiber opens up a vast field of research. It has been considered by many scientists as one of the most active fields in optics. In the same way, the study of the interaction between sound and light arises as an alternative for increasing the range of optical fiber technology applications. This interaction, known as acousto-optic interaction, is the key to construct several all-fiber photonic devices. In this thesis, experimental and simulated results of the modulation of diffraction gratings using the acousto-optic effect in fiber are presented. Applications of this effect in the communications and sensing fields are also described.

1.2   OBJECTIVES

The main objectives of this work is to study the acousto-optic interaction in diffraction gratings, specifically in Bragg and long period gratings, and demonstrate how different effects are achieved depending on the acoustic excitation. Once the phenomenon is understood, applications in telecommunications and sensing can be introduced.

1.3   THESIS HISTORY AND OUTLINE

This PhD thesis is a progression of a master dissertation which explores the simulation of the acousto-optic effect in fiber Bragg grating using a numerical approach based on the finite element and transfer matrix methods (OLIVEIRA *et al*, 2008a; OLIVEIRA 2008b). Based on the results of the numerical simulations, new applications not reported before in literature could be proposed. The first step was to assemble the experimental setup according to the simulation parameters and generate an acoustic wave within a fiber using a piezoelectric ceramic and a silica horn. The silica horn was the critical part of the assembly because there were no manufacturers in the world that could fabricate a small number of pieces at a reasonable price. Consequently, the need for cooperation with other research groups arose. The first collaboration started with the research visit of Prof. Dr. Alexandre A. P. Pohl to the group of Prof. Dr. John Canning at The University of Sydney – Australia in 2007. With the help of Mr. Peter Henry, at the time an employee of the Optical Fiber Technology Center (OFTC), the first silica horn for the experiments was constructed. Although some good experiments with this silica horn were carried out, it was not adequate in yielding a considerable acoustic effect in the gratings. Another cooperation started in 2009 with the *Instituto de Telecomunicações* of the University of Aveiro – Portugal, where a more efficient silica horn was fabricated. It was made by Mr. Pedro Miguel Roque Alves, from the chemistry department of the University of Aveiro. Following the production of the silica horn, a proper piezoelectric ceramic had to be acquired. Initially the chosen piezoelectric ceramic was purchased from *Physick Instrumente* (www.physikinstrumente.com), and later on, from Piezomechanik (www.piezomechanik.com), both companies from Germany. The chosen disc dimensions were based on the resonance frequency necessary for producing the acoustic effects predicted by the numerical simulations.

Following the assembly of the modulator, some experiments were performed and the results concerning the control of the grating properties, called the attention regarding their potential for new applications. Using the developed modulator, it was noticed that two different kinds of acoustic waves could be excited in the fiber (flexural and longitudinal) depending on the acoustic resonance of the piezo disc. The result was reported for the first time in literature and published in Optics Communications in 2010 (Oliveira *et al*, 2010a). Following the first development, an add-drop was built (OLIVEIRA *et al*, 2009a) in collaboration with the *Instituto de Telecomunicações*. At the same time a chromatic dispersion

compensator (OLIVEIRA *et al*, 2010b) and phase-shifted controllers (MARQUES *et al*, 2011) were also developed.

During the one year research time spent at the Interdisciplinary Photonics Laboratories (*i*PL) of The University of Sydney in 2009/2010, the characterization of the acousto-optic device was completed and two important developments in the field of acousto-optic modulation were achieved. The first was a method for controlling the grating properties during the writing process using the acousto-optic effect while sweeping the UV laser beam through the phase mask. This work, published in Applied Physics Letters (OLIVEIRA *et al*, 2010d), describes the successful attempt of writing a fiber Bragg grating in an acoustically excited fiber. The second development was a viscosity sensor, whose conception and innovation was awarded the best student paper prize in the 2nd Asia-Pacific Optical Sensors Conference (APOS 2010) held in Guangzhou – China (OLIVEIRA *et al*, 2010f).

This thesis is outlined in several topics as follows:

2. State of the Art – The chapter addresses optical fiber diffraction gratings (in special fiber Bragg gratings and long period gratings) and their acousto-optic modulation. A topic about the viscosity sensing is also presented.

3. Methodology – The methods used to simulate the mechanical structure and the experimental assembly are presented in this chapter.

4. Characterization of the Modulator – In this chapter, the experimental characterization of the modulator is presented. Numerical simulations and experimental evidences are used to verify the way acoustic waves modulates the diffraction grating spectra.

5. Applications – Applications are described and their respective experimental assemblies detailed. The devices performance are also presented and discussed in this chapter.

6. Conclusions – General conclusions regarding the development and theoretical modeling of the modulator along with specific conclusions concerning the performance of the devices are addressed in this chapter.

2   STATE OF THE ART

2.1   OPTICAL FIBER DIFFRACTION GRATINGS

Fiber diffraction gratings are basically layered gratings, which can be understood as a periodic pile of thin films in the core of the fiber with a modulated refractive index (LI, 1996). The discovery of the photosensitivity in optical fiber happened in 1978 at the Communications Research Center Canada (CRC), during experiments of non-linear effects. At the time a photoinduced permanent change was observed in the refractive index of the fiber core through an intense exposure to core-launched visible light from an argon ion laser (HILL *et al*, 1978). Since then, the study of fiber gratings started to call the attention of the scientific community. Fiber devices such as optical filters (KAWASAKI *et al*, 1978), optical sensors (BHATIA and VENGSARKAR, 1996), distributed Bragg reflector fiber lasers (DBR) (KRINGLEBOTN *et al*, 1994) were fabricated, making this technology a crucial solution for all-fiber communication and sensing devices.

In 1988 Meltz *et al* reported the fabrication of a fiber diffraction grating by exposing the fiber core externally to an intense UV interference pattern (MELTZ *et al*, 1989). This was an important advance in the fiber grating fabrication technology (HILL *et al*, 1993a). As the research in the field evolved, two kinds of fiber gratings were developed: one based on the reflection of the light, with short-period modulation, similar to those written by Hill *et al* (1978, 1993a), the so called fiber Bragg grating (FBG), and the other formed by long periods of modulation, known as long period fiber grating (LPG) (VENGSARKAR, 1996).

2.1.1   Fiber Bragg grating

When Hill *et al* (1978) launched an intense Argon-ion laser radiation at 488 nm into a Germania-doped fiber they observed a reflected light, whose power grew until almost all the light incident was reflected back from the fiber. After spectral measurements, they confirmed that a very narrowband Bragg grating filter had been formed over the entire length of the fiber (around 1 m). This grating was found to be tunable with temperature and strain, which enlarged the possibility of application of that technology. This grating was subsequently called Hill grating, and it sparked a vigorous research on the photosensitivity of germanium doped silica fibers (KAWASAKI, 1978). Advanced studies done by Lam and Garside (1981) showed that the grating strength increases as the square of the light intensity, suggesting a

two-photon process as the mechanism. However, a single photon process proved to be more efficient (LAM and GARSIDE, 1981, MELTZ, *et al*, 1989). Hosono *et al* (1992) and Nishii *et al* (1995) showed that the absorption band of the Germane-silicate glass is centered in the 240 nm wavelength. Therefore, irradiation with a wavelength coincident with this band shows to result in bleaching and the creation of other absorption bands, leading to a refractive index change that was described through the Kramers-Kronig relation (RUSSELL *et al*, 1991; OTHONOS and KALLI, 1999). It was then discovered that photosensitivity could be improved by up two orders of magnitude through hydrogenation of the optical fiber core before grating inscription, and in some cases without variation of the 240 nm absorption band (LEMAIRE *et al*, 1993). It has been suggested from the photoinduced index growth obtained in high- and low-germanium content fiber that photosensitivity at 193 nm obeys one-photon dynamics in high-germanium content fiber, and two-photon dynamics in low-germanium content fiber. The current consensus explains photosensitivity as being initiated though the formation of color-centers (HAND and RUSSELL, 1990) that gives way to compaction of the UV-irradiated glass (LIMBERGER *et al*, 1996; POUMELLEC, *et al*, 1996; OTHONOS and KALLI, 1999; CANNING, 2008).

In the work by Meltz *et al* (1989), they introduced a methodology to write FBGs, irradiating the core of the fiber from the side with two coherent ultraviolet light beams at 244 nm. The two light beams interfere, producing a periodic interference pattern that induces a periodic change in the refractive index of the fiber core. The technique is called the transverse holographic technique. It works because the fiber cladding is transparent to the UV light whereas the fiber core is highly absorbing instead. This makes it possible to write Bragg gratings in the core without removing the glass cladding. Furthermore, by using the technique, the angle between the two interfering beams can be varied causing the period of the generated grating to be changed, which leads to gratings that work at much longer wavelengths in a spectral region of interest for devices in fiber optic communications and optical sensors (HILL and MELTZ, 1997). Alternatively, one of the most effective methods for inscription of Bragg gratings in photosensitive fiber is the phase-mask technique, introduced by Hill *et al* (1993b) and Anderson *et al* (1993), where a diffractive optical element is employed to spatially modulate the UV writing beam.

The effect of permanently inducing changes in the refractive index (δn) of the fiber depends on several different factors such as the irradiation conditions (wavelength, intensity, beam fluency, etc.), the composition of the fiber core (dopants) and any processing of the fiber prior to irradiation, such as the hydrogenation of the fiber to enhance the

photosensitivity, called the hydrogen-loading technique (OTHONOS and KALLI, 1999; LEMAIRE *et al*, 1993; KASHYAP, 1999). According to Canning (2008), although mainstream grating writing using single photon excitation of germane-silicate based defects with UV light at 244 nm light remains the key technology for complex devices, it is now being complemented by a whole set of processes which can enhance and tailor the properties of both conventional and not-so-conventional fiber Bragg gratings. Canning presents an up to date review on photosensitivity, fiber gratings and devices for sensor and lasers (CANNING, 2008).

The FBG is characterized by three main parameters: reflectivity, period and length. These parameters can be controlled in order to, depending on the proper set of these characteristics, obtain gratings for a variety of special applications. The length of a uniform grating is limited by the dimension of the writing system (even though, demonstration of gratings longer than $l_g = 1$ m was already achieved), which normally is used to be in the order of millimeters or few centimeters. On the same way, the spectral bandwidth is conditioned by its length, as the reflection band of a uniform grating depends on its distance end to end. The chirped Bragg grating, one of the most interesting Bragg grating structures, is characterized by having a monotonically varying period, i.e. a non-periodic index modulation profile. This characteristic enhances the spectral bandwidth of the conventional FBG, allowing the FBG to achieve broadband reflectors (SUGDEN *et al*, 1997).

2.1.1.1 Writing process

Historically, FBGs were firstly recorded using internal writing (HILL *et al*, 1978) and the transversal holographic technique (MELTZ, *et al*, 1989). Both these methods have been superseded by the phase mask technique, which is schematically described in the diagram of figure 2.1. The phase mask is placed in contact or near contact with the fiber, and the UV beam impinges normally to the fiber axis. The beam passes through the mask and is spatially diffracted to form an interference pattern with pitch Λ along the fiber axis (HILL *et al*, 1993b). Since the period of the phase mask (Λ_{pm}) and the effective index of the fiber are known, the wavelength reflected by the grating can be estimated according to the Bragg condition for the *zero*th order

$$\lambda_B = n_{eff}\Lambda_{pm} = 2n_{eff}\Lambda,\qquad(2.1)$$

where λ_B is the Bragg wavelength and n_{eff} is the effective mode index at the grating.
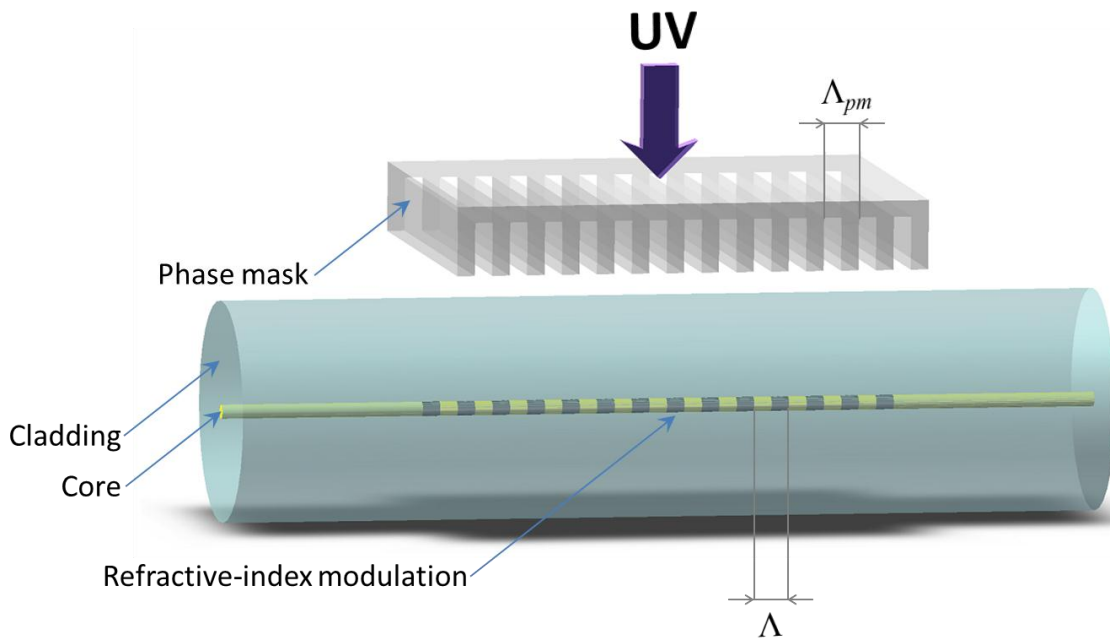
Figure 2.1 - Bragg grating fabrication apparatus based on the phase mask technique.

2.1.1.2 Fundamental properties of fiber Bragg gratings

The index modulation in the core represents a periodic structure that acts as a stop band filter. A narrow band of the incident optical field in the fiber is reflected successively and coherently by the planes that represent the index variations. For a simple case, the strongest interaction of energy between the co-propagating and counter-propagating modes occurs at the Bragg wavelength. This condition is also called the "phase match" condition. The grating is a device which changes the spectrum of an incident signal by coupling energy to other fiber modes. It can also be considered an intrinsic sensor because any change in fiber properties, such as strain, temperature or polarization which varies the modal index or grating pitch, will change the Bragg wavelength. The reflected band is constructed because each reflection from a crest in the index perturbation is in phase with the next one at λ_B, as shown in figure 2.2.
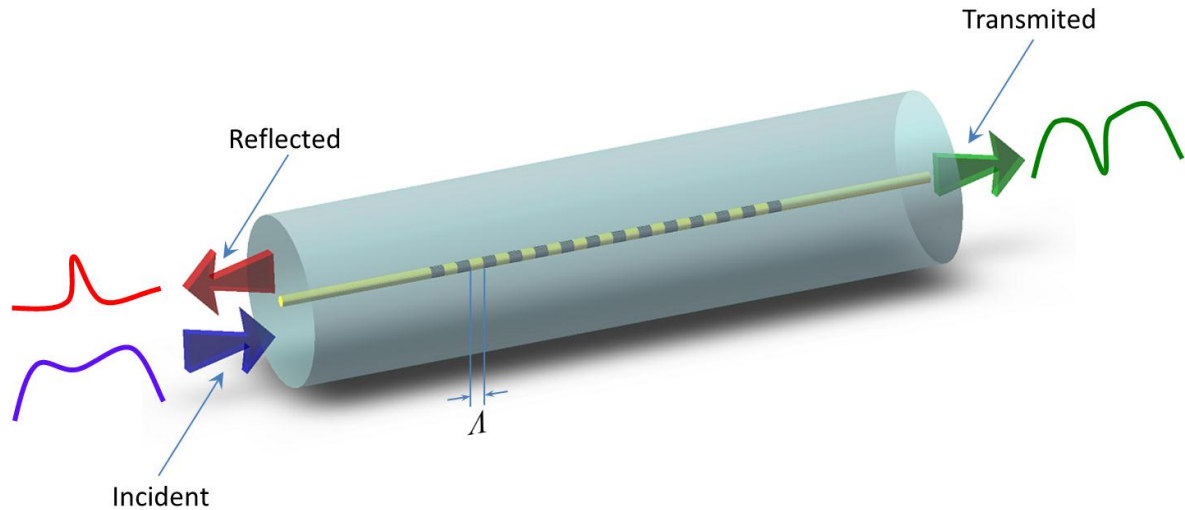
Figure 2.2 - Schematic diagram of the incident light in a FBG and its reflected and transmitted spectrum.

The grating characteristics can be understood and modeled by several approaches, such as the ones proposed by Kogelnick (1976), Weller-Brophy and Hall (1985) and Yamada and Sakoda (1987). However, the coupled-mode theory is often the foundation for many of these models (HILL and MELTZ, 1997). The resultant change in the refractive index, δn, due to the photo-induction is written as

$$\delta n(z) = \delta n_0 \left[1 + v \cos\left(\frac{2\pi}{\Lambda} z + \phi(z) \right) \right],$$ (2.2)

where δn_0 is the "dc" index change spatially averaged over a grating period, v is the contrast, determined by the visibility of the UV pattern, Λ is the nominal grating period and $\phi(z)$ describes the grating chirp. Figure 2.3 shows the observed index modulation in the core of a fiber showing the grating written by Malo *et al* (1993). One can see the index perturbation through optical microscope photography. In this case, the Bragg wavelength is $\lambda_B = 1535$ nm, considering the second-order reflection ($m\lambda_{resonance} = 3070$ nm, $m = 1, 2, 3, \ldots$), and correspond to the sharp dip in the transmission spectrum of the grating (MALO *et al*, 1993).
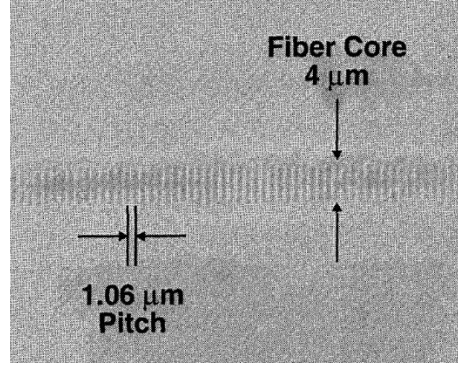
Figure 2.3 - Photoinduced perturbations (dark parallel fringes) as seen through an optical microscope. Spacing between lines in image corresponds to the 1060-nm period of the phase grating (MALO *et al*, 1993).

The most useful property of the FBGs is the possibility of making its Bragg wavelength tunable, which enables the application in a wide range of devices in communications and sensing. Any change in the gratings parameters, such as the effective refractive index and/or period will modify the reflected wavelength. The sensitivity of the FBGs to changes in these parameters is governed by the strain-optic and thermo-optic properties (KASHYAP, 1999; IOCCO *et al*, 1997; NEVES JR, 2008). The Bragg wavelength dependence with the effective index and the pitch of the grating is given as

$$\lambda_B = 2n_{eff}\Lambda. \tag{2.3}$$

The shift of the Bragg wavelength due to changes in the temperature and longitudinal deformation is derived as

$$\Delta\lambda_B = 2\left[\Lambda\frac{\partial n_{eff}}{\partial\varepsilon} + n_{eff}\frac{\partial\Lambda}{\partial\varepsilon}\right]\Delta\varepsilon + 2\left[\Lambda\frac{\partial n_{eff}}{\partial\Theta} + n_{eff}\frac{\partial\Lambda}{\partial\Theta}\right]\Delta\Theta, \tag{2.4}$$

where $\Delta\varepsilon$ is the applied longitudinal strain of the grating and $\Delta\Theta$ is the change in temperature. $\partial n_{eff}/\partial\varepsilon$ represents the longitudinal stress optic coefficient (strain-optic property) and $\partial n_{eff}/\partial\Theta$ the temperature coefficient of the refractive index (thermo-optic property). Since the Bragg wavelength is a function of n_{eff} and Λ, the simplest method of altering the transfer characteristics of a FBG is to impose a temperature and/or strain profile along the length of the grating (KASHYAP, 1999).

The term $\partial\Lambda/\partial\varepsilon$ corresponds to a change in the grating period and the strain-optic coefficient induced change in the refractive index. The strain effect term can be also expressed as (MELTZ and MOREY, 1991; HILL and MELTZ, 1997)

$$\Delta\lambda_B = \lambda_B(1 - p_e)\varepsilon_z, \tag{2.5}$$

where

$$p_e = \frac{n_{eff}^2}{2}\left[p_{12} - \sigma(p_{11} + p_{12})\right] \tag{2.6}$$

is the effective strain-optic constant. In this equation, p_{11} and p_{12} are the components of the strain optic tensor, and σ is the Poisson's ratio (OTHONOS and KALLI, 1999). Table 2.1 shows the values for some of these coefficients, depending on the wavelength and effective refractive index.

Table 2.1 - Values for p_{11}, p_{12} and σ of silica-based materials found in literature.

Reference	λ (nm)	n_{eff}	p_{11}	p_{12}	σ	Material
YARIV and YEH, 1984	630	1,46	0,121	0,27	0,21	Fused silica
PRIMAK and POST, 1959	589,2	1,458	0,121	0,27	0,164	Silica glass
BERTHOLDS and DÄNDLIKER, 1988	633	1,458	0,113	0,252	0,16	Optical fiber
BORELLI and MILLER, 1968	632,8	1,457	0,126	0,26	0,168	Fused silica
XU *et al*, 1993	1533,3	1,465	0,121	0,17	0,17	Optical fiber
HOCKER, 1979	633	1,456	0,121	0,17	0,17	Optical fiber

In the same way, the term that represents the effect of temperature can be written as

$$\Delta\lambda_B = \lambda_B\left(\alpha_\Lambda + \alpha_{n_{eff}}\right)\Delta\Theta, \tag{2.7}$$

where

$$\alpha_\Lambda = \frac{1}{\Lambda}\frac{\partial\Lambda}{\partial\Theta} \tag{2.8}$$

is the thermal expansion coefficient for the fiber and the quantity

$$\alpha_{n_{eff}} = \frac{1}{n_{eff}}\frac{\partial n_{eff}}{\partial\Theta} \tag{2.9}$$

represents the thermo-optic coefficient.

Finally, considering only longitudinal strain and temperature variation, (2.4) can be rewritten as

$$\Delta\lambda_B = 2\lambda_B\left[\left(1 - p_e\right)\varepsilon_z + \left(\alpha_\Lambda + \alpha_{n_{eff}}\right)\Delta\Theta\right]. \tag{2.10}$$

Therefore, any external perturbation of the grating, either by longitudinal strain or by temperature, will change the reflection wavelength making sensing applications potentially

and practically interesting. However, only one perturbation at a time is of interest, so, the deconvolution of strain and temperature becomes necessary (XU *et al*, 1994; XU *et al*, 1995; JAMES *et al*, 1996). The range of applications of the tunability property of FBG is very wide, and goes from broadband tunable optical filters (MOKHTAR *et al*, 2003) to fiber lasers (BALL and GLENN, 1992).

Gratings that have a nonuniform period along their length are known as chirped. Chirped gratings, which present the term $\phi(z)$ in (2.2) different from zero, are useful for many applications and can be generated in a number of ways, including the application of varying strain after fabrication (BYRON *et al*, 1993; KRUG *et al*, 1995), writing using a multi-step technique (KASHYAP *et al*, 1994) or using a continuously chirped phase mask. More details on continuous chirped gratings can be found in Kashyap (1999).

FBGs can be used for correcting chromatic dispersion, exploring the capability of pulse compressing in optical links (TREACY, 1969; NAKATSUKA *et al*, 1981). Figure 2.4 shows the reflection spectrum and group delay behavior of a uniform FBG written directly using phase mask (UV light @ 248 nm) with $l_g = 25$ mm length. The green circle represents the useful range for application in chromatic dispersion. This grating in particular presents a quadratic behavior for the dispersion compensation, and the group delay dispersion parameter has the value $d \sim 3312$ ps/nm, over $\Delta\lambda = 0{,}078$ nm bandwidth.
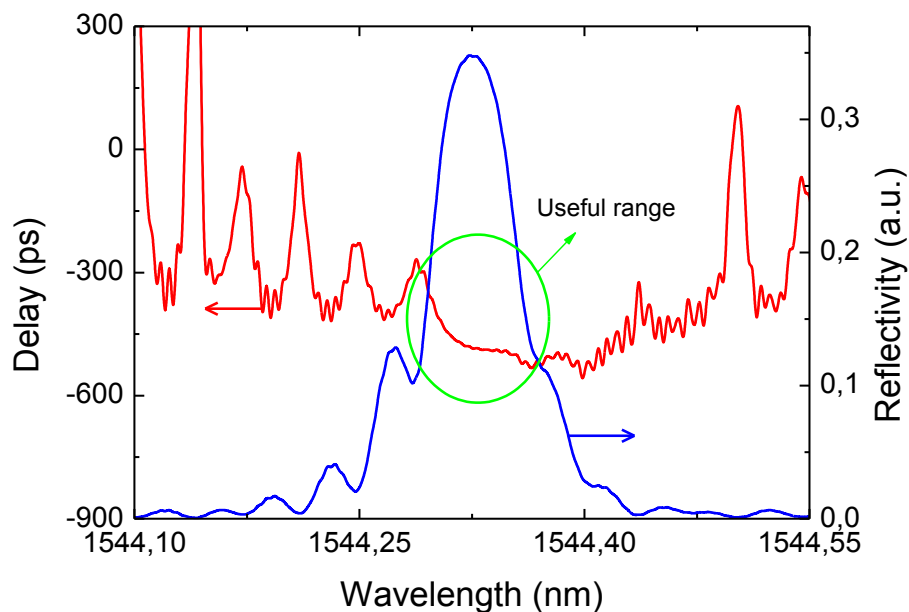
Figure 2.4 - Reflection spectrum and group delay characteristics of a uniform FBG. The green circle represents the useful range for chromatic dispersion.

2.1.2 Long period gratings

A long period grating (LPG) is a special optical fiber diffraction grating first reported by Vengsarkar *et al* in 1995 (VENGSARKAR *et al*, 1996). The LPG refractive index modulation, in contrast to the FBG, is in order of hundreds of micrometers, and is chosen to couple light from the guided fundamental mode of the fiber into the forward propagating cladding modes. The wavelength-dependent phase-matching condition in LPGs is governed by the relationship

$$\lambda_m = \left(n_{eff} - n_{cl}^m\right)\Lambda, \tag{2.11}$$

where λ_m is the dip wavelength of the *m*th attenuation band, n_{eff} and n_{cl}^m represent the effective indices of the fundamental guided mode and the *m*th LP_{0m} cladding mode, respectively, and Λ is the grating period. Around λ_m, the energy of the propagating cladding modes is lost due to absorption and scattering in the surrounding environment, creating a rejection band in the transmission spectrum, strongly dependent of the external medium (temperature, refractive index, pressure and so on). The high sensitivity of LPGs to the refractive index of the surrounding material shows great potential in applications such as chemical detectors (FALATE *et al*, 2005) and humidity sensor (TAN *et al*, 2005).

The minimum transmission at λ_m is given by the expression

$$T^m = 1 - \sin^2\left(\kappa_m l_g\right), \tag{2.12}$$

where l_g is the length of the LPG and κ_m is the coupling coefficient for the *m*th cladding mode, which is determined by the overlap integral of the core and respective cladding mode and by the amplitude of the periodic modulation of the mode propagation constants (JAMES and TATAM, 2003).

2.1.2.1 Writing process

The most used inscription techniques of LPGs are based on induced changes in the refractive index of the fiber core through electric discharge (REGO *et al*, 2005), exposure to 193 nm UV light (GUAN *et al*, 2000) or 10,6 µm (CO_2) laser radiation (WANG *et al*, 2009). Another technique uses the formation of microbends in the fiber through transversal pressure of the fiber axis (BLAKE *et al*, 1986). The desired grating can easily be fabricated by use of inexpensive amplitude masks of different periods (BHATIA and VENGSARKAR, 1996).

2.1.2.2 Properties of LPG

Long period gratings present the advantage of, depending on the order of cladding mode to which coupling takes place (BHATIA, 1999), and on the refractive index of the optical fiber (SHIMA *et al*, 1997), a range of responses to a particular measurand. For example, an LPG may have one attenuation band that has a positive sensitivity, another that presents a negative sensitivity and even one band that is insensitive (JAMES and TATAM, 2003). LPG transmission spectrum, which presents five attenuation bands, is shown in figure 2.5 (BHATIA *et al*, 1997). Each one of these bands can be used to measure a specific measurand.
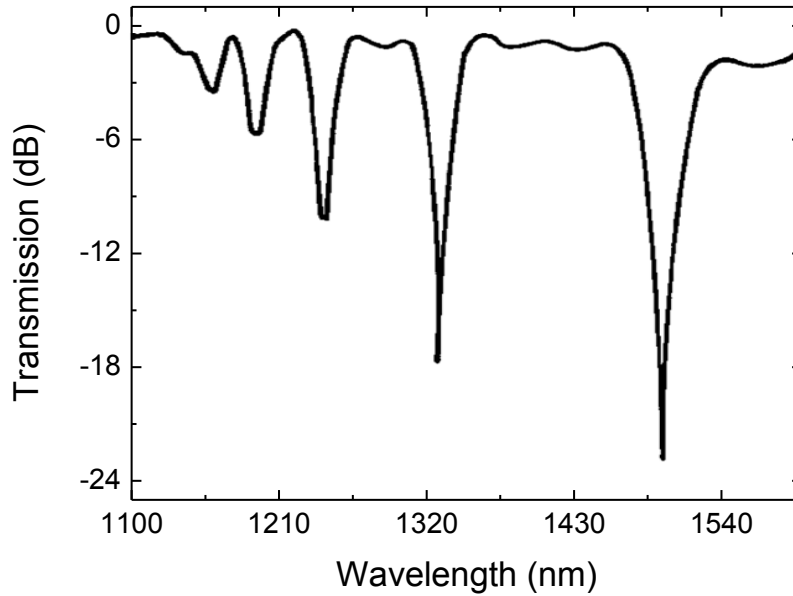
Figure 2.5 - Transmission spectrum of an LPG written in a SMF-28 fiber with period 320 μm, by Bhatia *et al* (1997).

The sensitivity of long period gratings to temperature and strain can be understood in the same way as the FBGs. From (2.11), the sensitivity to temperature and strain is written as

$$\Delta\lambda_m = \frac{\partial\lambda_m}{\partial\left(\delta n_{eff}^m\right)} + \frac{\partial\lambda_m}{\partial\Lambda}$$

$$= \left[\frac{\partial\left(\delta n_{eff}^m\right)}{\partial\Theta} + \frac{\partial\left(\delta n_{eff}^m\right)}{\partial\varepsilon}\right]\Lambda + \left[\frac{\partial\Lambda}{\partial\Theta} + \frac{\partial\Lambda}{\partial\varepsilon}\right]\delta n_{eff}^m,$$

$$(2.13)$$

where $\delta n_{eff}^m = n_{eff} - n_{cl}^m$. In this equation, the first term on the right is the material contribution, and is related to changes in the differential refractive index of the core and the cladding arising from the thermo-optic and strain optic effects. This contribution is dependent upon the composition of the fiber (SHIMA *et al*, 1997) and is strongly dependent upon the order *m* of the cladding mode. The second term on the right is related with the waveguide effect contribution as it results from changes in the period of the LPG. Different effects are achieved if considering different gratings. For example, for coupling to low order cladding modes (achieved with longer periods, $\Lambda > 100$ μm), the material effects dominates, while for coupling to higher-order cladding modes (achieved using shorter periods, $\Lambda < 100$ μm), the material effect can be negligible (BHATIA, 1997). Appropriate choice of grating period and fiber composition will thus allow the generation of attenuation bands with positive, negative or zero sensitivity to strain or temperature. This property presents several advantages if comparing with fiber Bragg gratings.

By differentiating (2.11), (2.13) can be simplified as

$$\frac{\Delta\lambda_m}{\lambda_m} = \left[\frac{1}{\Lambda}\frac{\partial\Lambda}{\partial\Theta} + \frac{1}{\delta n_{eff}^m}\frac{\partial\left(\delta n_{eff}^m\right)}{\partial\Theta}\right]\Delta\Theta + \left[\frac{1}{\Lambda}\frac{\partial\Lambda}{\partial\varepsilon} + \frac{1}{\delta n_{eff}^m}\frac{\partial\left(\delta n_{eff}^m\right)}{\partial\varepsilon}\right]\Delta\varepsilon \tag{2.14}$$

$$= \left(\alpha + o\right)\Delta\Theta + \left(1 + p\right)\Delta\varepsilon$$

where

$$\alpha = \left(\frac{1}{\Lambda}\frac{\partial\Lambda}{\partial\Theta}\right) \tag{2.15}$$

is the thermal-expansion coefficient,

$$o = \frac{1}{\delta n_{eff}}\frac{\partial\delta n_{eff}^m}{\partial\Theta} \tag{2.16}$$

is the thermal-optic coefficient, and

$$p = \frac{1}{\delta n_{eff}^m}\frac{\Delta\left(\delta n_{eff}^m\right)}{\Delta\varepsilon} \tag{2.17}$$

is the strain-optic coefficient. The thermal-expansion coefficient α_Λ has its value around 5×10^{-5} / °C, while *o*, which is variable and related to the grating period and the coupled cladding mode order, generally varies from 2 to 4×10^{-5} / °C for the gratings written in standard SMF-28 fiber. Consequently, as $o \gg \alpha_\Lambda$, the temperature term $(\alpha_\Lambda + o)$ of LPGs mostly depends on the thermal-optic coefficient *o*. The strain coefficient $(1 + p)$ is negative

and varies slightly (from -0,5 to -0,7) with the grating period and the coupled cladding mode order.

In the case of the sensitivity to external refractive index, the analytical expression derived by Chiang *et al* (2000), which describe the dip wavelength shift ($\delta\lambda_0$) when the external refractive index changes from n_{ex0} to n_{ex} is written as

$$\delta\lambda_0 \approx \frac{u_\infty^2 \lambda_0^3 \Lambda}{8\pi^3 n_{cl} a^3} \left[\frac{1}{\sqrt{n_{cl}^2 - n_{ex0}^2}} - \frac{1}{\sqrt{n_{cl}^2 - n_{ex}^2}} \right], \tag{2.18}$$

where u_∞ is the *m*th root of the Bessel function J_0 and *a* is the cladding radius. From (2.18) one notes that the refractive index sensitivity presents a nonlinear behavior that is more pronounced when the external refractive index is close to the cladding refractive index. Differentiating (2.18) with respect to n_{ex}, an expression for the LPG sensitivities *s* to the external media refractive indices can be written as (KAMIKAWASHI, 2007)

$$s = \frac{\partial \lambda}{\partial n_{ex}} = \frac{u_\infty^2 \lambda_0^3 \Lambda}{8\pi^3 n_{cl} a^3} \left[\frac{n_{ex}}{\left(n_{cl}^2 - n_{ex}^2\right)^{3/2}} \right]. \tag{2.19}$$

2.2   ACOUSTO-OPTIC MODULATION IN DIFFRACTION GRATINGS

In 1922, León N. Brillouin proved that when a liquid, excited by a mechanical wave with short wavelength, is irradiated with visible light, a diffraction pattern is generated, similar to that obtained with a diffraction grating (BORN and WOLF, 1980). The first experimental work on the interaction between mechanical waves and electromagnetic radiation was done by Brillouin, who studied the *x*-rays diffraction in a homogeneous transparent solid excited by thermic vibration, which generates elastic waves. In 1932, experiments carried out by Lucas and Biquard in France and Debye and Sears in the United States studied the optical properties of solids excited by ultra-sound waves and demonstrated the scattering of light by them. Both experiments demonstrated that the dielectric properties of a medium are modified by acoustic waves causing variation in the propagating electric field. The acousto-optic effect can be understood as a phenomenon of diffraction of electromagnetic radiation firstly observed in liquids and later on solid materials. This effect, for example, was used to measure the speed and attenuation of mechanical waves in transparent media. In 1978, Thurston presented the theory of propagation of mechanical waves in homogeneous cylindrical waveguides formed by cladding and core (clad rods), which was consequently used to model optical fibers. Thurston showed a complete description of the mechanical

resonant modes in these waveguides, and also pointed out the limitations of each case, i.e. considering guides without cladding, thin cladding, infinite cladding, etc. (THURSTON, 1978).

After the invention of the laser and high frequency piezoelectric transducers (in the range of hundreds of MHz), the acousto-optic interaction attracted attention, and a new and interesting research topic raised up as a promising area for telecommunications and sensing. Roy *et al* (1987) showed that, through the use of elastic waves, it is possible to rapidly change some properties of light, such as intensity and frequency (MACLENNAN *et al*, 2007). The interaction between laser beams and bulk elastic waves gave rise to new components, such as modulators (ROY *et al*, 1987; PALDUS *et al*, 1997), optical deflectors (WARNER *et al*, 1972; GOTTLIEB *et al*, 1983), optical spectrum analyzers (GOTTLIEB *et al*, 1992), tunable optical filters (GIRUTS and KOPYLOV, 1991), among others. On the other hand, the same effect can be used to sense properties of a specific solid or used in acoustic emission sensors (PEREZ *et al*, 2001; BETZ *et al*, 2003).

2.2.1 The effect

The basic structure of the fiber acousto-optic modulator is based on the device patented by Zemon and Dakss (1978) in the United States (US6068191). Such modulator is able to modulate the intensity of light through the application of an acoustic wave. Figure 2.6 shows the schematic diagram of the device:
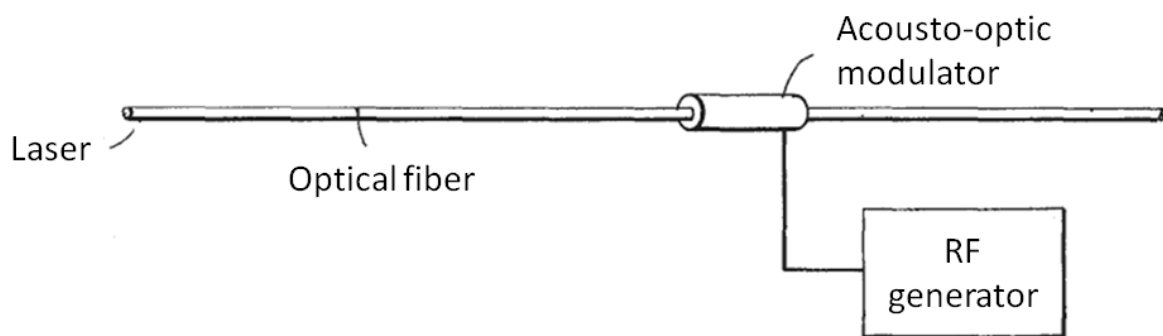
Figure 2.6 - Acousto-optic modulator, patent number 6.068.191 (1978) – The United States (ZEMON and DAKSS, 1978).

In 1986, Russell showed that the planes of a fiber Bragg grating can be modulated with the use of acoustic waves. He called this effect acousto-optic superlattice modulation (AOSLM), which is based on the Bragg-type Floquet-Bloch waves (RUSSELL, 1986a). The Floquet-Bloch waves are the simplest complete solutions of Maxwell's equations that exist in

a periodically stratified medium such as, for example, a single-mode fiber with a diffraction grating written in it (RUSSELL, 1986b). In AOSLM the counter-propagating optical modes are generated by the fine pitch Bragg grating and the coarse-pitch, generated by the acoustic wave, which forms the superlattice. Coupling is maximum when the inter-Bloch-wave beat period matches the acoustic wavelength (LIU *et al*, 1997).

Even though various mechanical modes can be generated in fibers (for example, radial, torsional, longitudinal or flexural), effects in gratings are achieved manly through longitudinal and flexural excitation. Therefore, in this work two kinds of acoustic excitation are considered, one due to the propagation of longitudinal acoustic wave and the other due to the flexural vibration of the fiber.

2.2.1.1 Longitudinal acoustic waves

When longitudinally launched along the fiber, which contains the fiber Bragg grating, the acoustic wave causes a periodic compression and rarefaction strain field, causing a change in the effective refractive index of the fiber, through the photo-elastic constant, p_e (see equation 2.6), while moving the modulation planes of the grating. An analytical approach by Russell and Liu (2000) defined the resulting strain field in the form:

$$\begin{aligned} \varepsilon(p) &= \varepsilon(k_s z - \omega_s t) \\ &= \varepsilon_0 \cos(k_s z - \omega_s t) \end{aligned}$$

(2.20)

where $p = (k_s z - \omega_s t)$ is the propagation phase, $k_s = 2\pi/\lambda_s$ is the acoustic wave vector, λ_s is the acoustic wavelength, and ω_s is the angular frequency. For an acoustic beam of area A, carrying power P_s in a medium with Young's modulus E and acoustic group velocity v_{gs}, the peak strain has the value

$$\varepsilon_0 = \sqrt{\frac{2P_s}{EA v_{gs}}} .$$

(2.21)

The periodic strain field perturbs the grating in two ways. Firstly, the effective refractive index (n_{eff}) increases according to the elasto-optic effect, causing changes in the optical path length. Thus, the effective refractive index variation proportional to the elasto-optic changes can be expressed as

$$\Delta n_{eff} = (1 - \chi)\varepsilon(p),$$

(2.22)

where χ is the stress-optical coefficient of the fiber. Secondly, the grating pitch is periodically modulated, causing a spatial-frequency modulation. The resulting effective refractive change then given as

$$\Delta n_{eff}(p) = (1-\chi)\varepsilon(p) + n_0 \left\{ 1 + C\cos\left[K\left(z - \int \varepsilon(p)dz\right) \right] \right\}, \tag{2.23}$$

where C is the modulation depth of the effective refractive index n_0 in the unperturbed FBG, $K = 2\pi/\Lambda$ is the grating vector (RUSSELL and LIU, 2000).

Replacing (2.20) in (2.23), one shows that the pitch modulation produces a sequence of sidebands in spatial frequency whose amplitudes are given by a standard Bessel function expansion as

$$
\begin{aligned}
\cos\left[Kz - m\sin(p) \right] &= \\
&= J_0(m)\cos Kz + \sum_{n=1}^{\infty} J_n(m)\left[(-1)^n \cos(Kz+np) + \cos(Kz-np) \right], \\
&= J_0(m)\cos Kz + \sum_{n=1}^{\infty} J_n(m)\left\{ \begin{array}{l} (-1)^n \cos\left[(K+nk_s)z - n\omega_s t \right] + \\ + \cos\left[(K-nk_s)z + n\omega_s t \right] \end{array} \right\}
\end{aligned}
\tag{2.24}
$$

where

$$m = \frac{K\varepsilon_0}{k_s} = \frac{\lambda_s \varepsilon_0}{\Lambda}. \tag{2.25}$$

Note that m changes sign with the direction of the acoustic wave. It is clear that a sequence of ghosts of the original fiber grating form at spatial frequencies given by successive spatial sidebands of K. The amplitudes of these sidebands are given for small argument ($|m| \ll 1$), as

$$J_n(m) \cong \frac{m^n}{2^n n!}. \tag{2.26}$$

One can illustrate this formulation with the help of figure 2.7, which shows the forward (0) and backward (1) Bloch waves. Figure 2.7(*a*) shows the behavior of the Bloch waves for an unperturbed FBG, while figure 2.7(*b*) shows a longitudinal wave exciting the fiber, whose effect causes additional reflections band to appear in the FBG spectrum.
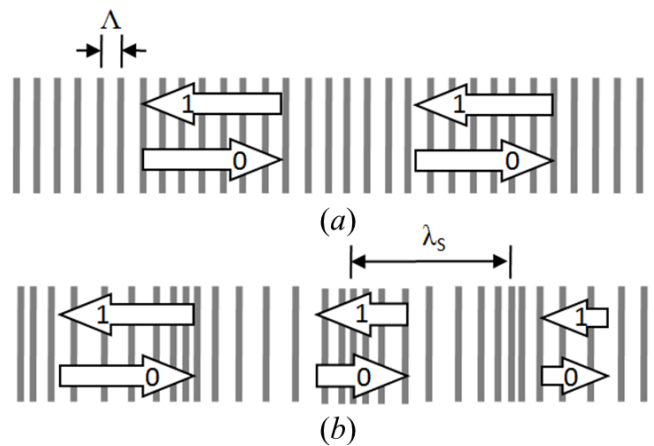
Figure 2.7 - Forward (0) and backward (1) Bloch waves of (*a*) unperturbed FBG and (*b*) longitudinally excited with acoustic wave of wavelength λ_s. A forward Bloch wave incident from the left-hand side is gradually converted into a backward Bloch wave traveling from the right-hand side.

The disadvantage of this analytical method is the absence of information about the strain field generated in the fiber by, for example, a modulator based on the silica horn technique using a piezoelectric transducer. This issue can be solved by means of numerical approaches, considering the real dimensions of the device and practical boundary conditions. Oliveira *et al* (2008a) showed the numerical simulation of the longitudinal acousto-optic effect in FBG using the finite element method (FEM) together with the transfer matrix method (TMM). The FEM approach allows the strain field caused by the acoustic wave to be completely characterized along the structure while the TMM is used to obtain the resulting spectrum generated by the corresponding deformed grating. Simulation results showed the formation of lateral lobules in the FBG reflection spectrum, caused by the displacement of the modulation planes of the FBG and a change of the effective refractive index, through the elasto-optic effect. Figure 2.8 shows the reflection spectrum obtained by numerical simulation of an FBG excited by a longitudinal acoustic wave with frequency $f_s = 1$ MHz and load $P_0 = 1$ N applied on the base of the silica horn (OLIVEIRA *et al*, 2008a).
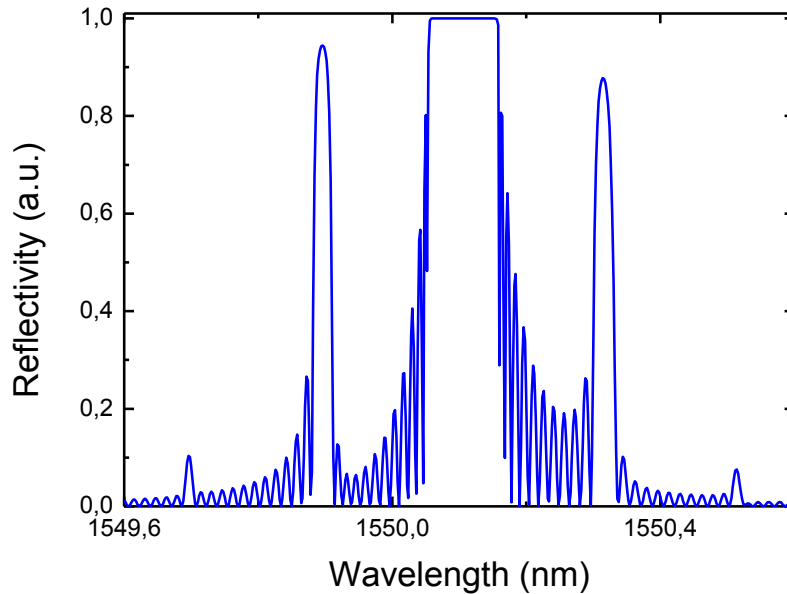
Figure 2.8 - Reflection spectrum of an FBG when excited by an acoustic wave at
f_s = 1 MHz and load P_0 = 1 N (OLIVEIRA *et al*, 2008a).

Figure 2.9 shows the schematic diagram of the acousto-optic modulator used in the numerical simulations, which is the base of the acousto-optic modulator used to carry out the experiments in this work. The Bragg grating acousto-optic modulator (BG-AOM) consists of a piezoelectric transducer (PZT), responsible for the generation of the acoustic wave, the silica horn, responsible for coupling the acoustic wave to the optical fiber, where the FBG is inscribed. At the end, a holder is used in order to allow the formation of a standing wave. In this model a tapered region is used in order to enhance the acousto-optic effect. However, along the work, Oliveira *et al* (2008a) showed that the presence of the taper can be neglected, and the same strain field can be obtained by changing the dimensions of the silica horn.
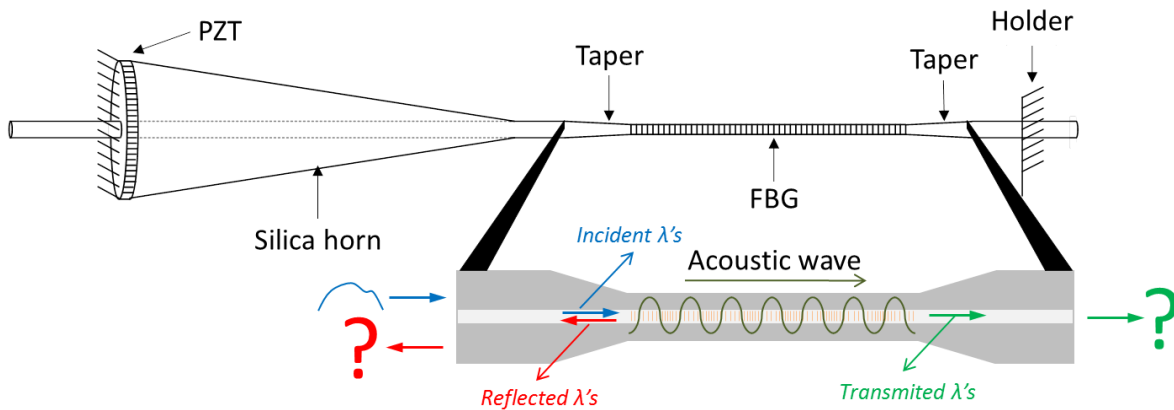
Figure 2.9 - Acousto-optic modulator used by Oliveira *et al* (2008a) to simulate the behavior of the FBG under acousto-optic modulation.

Oliveira *et al* (2010a) reported on the analysis and measurement of the acoustic vibration modes of an experimental assembly made of a silica horn with a length of silica fiber, in which the grating is inscribed (similar to the one showed in figure 2.9, except by the absence of the taper), and demonstrated, by controlling the excitation of a particular resonance mode, that either flexural or longitudinal acoustic waves are generated. Regarding the longitudinal case, figure 2.10 shows how acoustic wave with low and high frequency (comparing the acoustic wavelength with the grating length) changes the modulation planes of the grating. Figure 2.10(*a*) shows the behavior of the planes when no acoustic wave is applied, figure 2.10(*b*) the case for the excitation of an acoustic wave at low frequency and figure 2.10(*c*) the case for the excitation at high frequency. When the longitudinal acoustic wavelength is longer than the FBG length (low frequency regime), a compression and rarefaction strain field corresponding to less than one period extends over the entire grating and whose net result causes a small shift in the Bragg wavelength. Figure 2.10(*b*) exemplifies the case where the net result of the strain field is red shifting the Bragg wavelength. On the other hand, in the high frequency regime, the longitudinal acoustic wavelength is much shorter than the grating length and the resulting compression and rarefaction strain field acts on modulating the grating planes. This causes the side lobules to exist. However, in this case, no displacement of the wavelength occurs. This situation is depicted in figure 2.10(*c*).
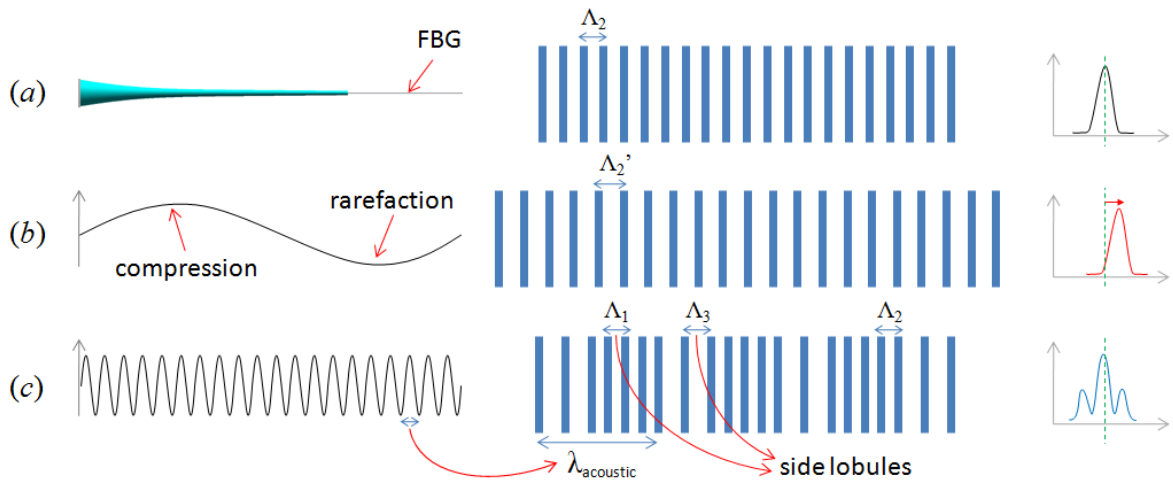
Figure 2.10 - Effect of the longitudinal acoustic wave in the FBG modulation planes when (*a*) no acoustic wave, (*b*) low frequency and (*c*) high frequency is applied in the fiber, respectively. The very right scheme shows the corresponding spectrum behavior.

Figure 2.11 shows the comparison of experimental and numerical simulation results under the excitation of a longitudinal wave at f_s = 1,089 MHz and V_{PZT} = 30 V, which correspond to a load P_0 = 3 N (Oliveira *et al*, 2010a). The FBG length is l_g = 50 mm, while the acoustic wavelength is $\lambda_{acoustic}$ = 5,27 mm.
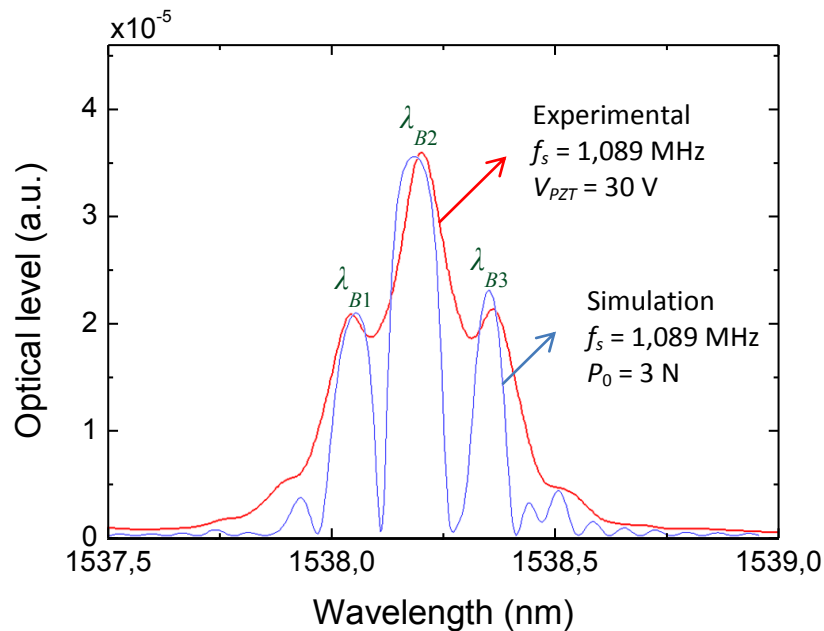
Figure 2.11 - Experimental and simulation of an FBG under excitation of a longitudinal acoustic wave at *f* = 1,089 MHz. Applying V_{PZT} = 30 V at the PZT corresponds to a load of P_0 = 3 N on the basis of the silica horn (OLIVEIRA *et al*, 2010a).

Regarding the applications of the longitudinal excitation of the FBG, Liu *et al* (1998) constructed a narrow band acousto-optic tunable reflector. The lateral lobules are assumed as correspondent to a weak version of permanent FBGs, also called previously as "ghost" gratings. These unique properties lead to important applications in Q-switching of lasers (DELGADO-PINAR *et al*, 2006), wavelength shifting (Liu *et al*, 2000), among others.

Minardo *et al* (2005) reports the use of the acousto-optic effect in FBG as an ultrasonic sensor, showing the response of the FBG subjected to the longitudinal acoustical field theoretically and numerically. Tsuda (2005), on the other hand, shows the practical application of such sensor for ultrasonic and damage detection in carbon fiber-reinforced polymer (CFRP).

2.2.1.2 Flexural acoustic waves

In the same way that longitudinal acoustic waves affects diffraction gratings in fibers, flexural acoustic waves can change the grating spectra. Flexural waves are basically bending fields that propagate along the fiber. Since the early 80's, bending effects in optical fibers have been studied. Taylor (1984) studied the bending effects in optical fibers, which cause power propagation in guided modes to be lost by coupling to radiation modes. These bends were caused by wrapping the fiber around mandrels or deploying it in flexible cables. Taylor also proposes the generation of microbendings in fiber using mechanical transducers to produce a periodic perturbation in the direction of the fiber's axis. However, in his experiments, Taylor used an apparatus illustrated in figure 2.12, where it is assumed that the fiber path is constrained by the mechanical comb only at the points of contact separated by a distance $\Lambda/2$ in the z direction. This device, according to Taylor, can be used as an efficient $LP_{01} \leftrightarrow LP_{11}$ mode converter.
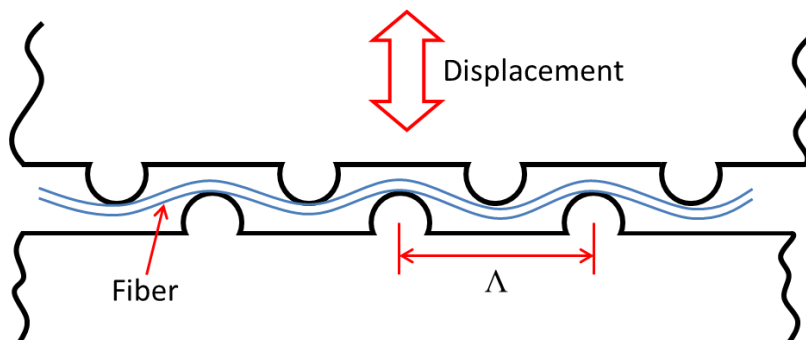
Figure 2.12 - Optical fiber subjected to spatially periodic bends (TAYLOR, 1984).

Dimmick *et al* (2000) designed a flexural acoustic wave generator in fiber, using a tapered optical fiber with l_g = 4 cm and d_f = 6,8 μm (See figure 2.13). When driven with a high frequency RF signal ($f_s \approx$ 30 MHz), a coaxial shear mode PZT transducer produces an acoustic vibration that is coupled to the optical fiber by a glass horn. The acoustic wave propagates as a flexural wave along the fiber. The flexural wave achieves its maximum amplitude at the tapered region. Light entering the tapered region of the fiber spreads out of the fiber core exciting the fundamental (LP_{01}) mode of the taper waist. In the absence of an acoustic wave this light travels through the taper region undisturbed and is coupled back to the fiber core as it propagates up the taper transition. When a flexural acoustic wave exists, periodic microbends in the taper region couple light from the LP_{01} mode to one or more higher order modes, which are not captured by the fiber core after the taper (DIMMICK *et al*, 2000).
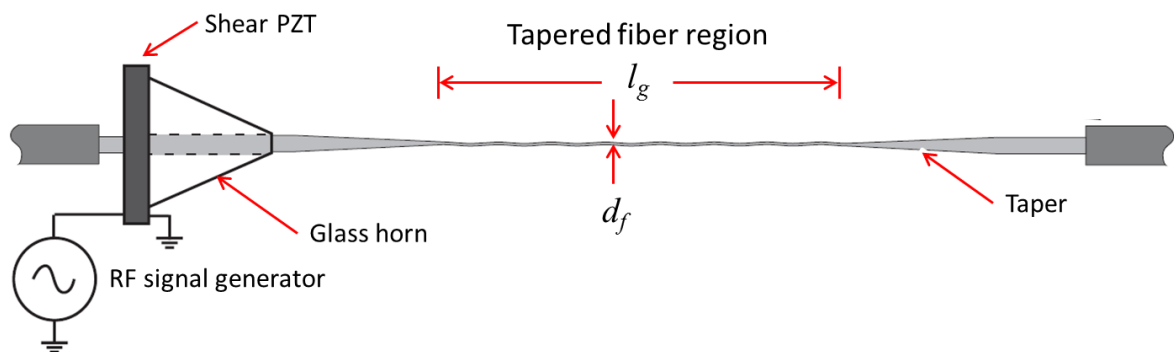
Figure 2.13 - Schematic diagram of tapered fiber acousto-optic tunable filter (DIMMICK *et al*, 2000).

Engan *et al* (1986) used the property of mode conversion through flexural acoustic wave to develop an optical frequency shifting in two-mode optical fibers, which basically converts one propagating mode to another, however, the flexural acoustic wave is generated positioning the glass horn transversally to the fiber axis, as shown in figure 2.14.
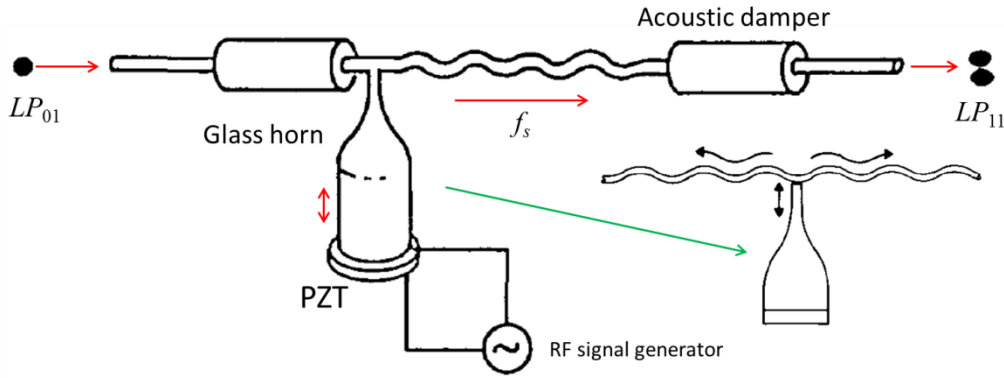
Figure 2.14 - Basic setup for generation of flexural acoustic waves. Using this particular device, Engan *et al* (1986) developed a frequency shifting in a two-mode fiber.

Considering the coupling between two optical modes, and denoting mode 1 as the fundamental mode, which contains all the energy before the acousto-optic interaction, and mode 2 as the one that carries a portion of the optical power after the interaction, the fraction of light coupled from mode 1 to mode 2 after the interaction length (L_i), can be written as

$$\eta = \frac{|\kappa|^2}{|\kappa|^2 + \left(\frac{\Delta\beta}{2}\right)^2} \sin^2 \left\{ \left[|\kappa|^2 + \left(\frac{\Delta\beta}{2}\right)^2 \right]^{\frac{1}{2}} L_i \right\},$$

(2.27)

where κ is the acousto-optic coupling coefficient and $\Delta\beta$ is the phase difference, defined as

$$\Delta\beta = 2\pi \left(\frac{1}{L_b(\lambda)} - \frac{1}{\lambda_s(f_s)} \right),$$

(2.28)

where λ_s is the flexural wavelength, L_b is the intermodal beat length, defined as the necessary length for mode 1 to acquire a phase shift of $\Delta\varphi = 2\pi$ when compared with mode 2. From equation (2.27) one notices that, if $\Delta\beta$ is much larger than $|\kappa|$, no light is coupled from mode 1 to mode 2, while if $\Delta\beta = 0$ all light is coupled to mode 2. Using these boundary conditions, the intermodal beat length can be calculated as

$$L_b = \frac{\pi}{2|\kappa|}.$$

(2.29)

From (2.28), when $\Delta\beta = 0$ the phase match condition is satisfied and can be expressed by

$$L_b(\lambda) \equiv \frac{\lambda}{n_1(\lambda) - n_2(\lambda)} = \lambda_s(f_s).$$

(2.30)

As L_b varies with λ, it can be assumed as a factor that determines the bandwidth of the acoustic coupling, for a given acoustic wavelength, i.e. (BLAKE *et al*, 1987)

$$\Delta\lambda L_i = 0{,}8 L_b^2(\lambda)\left|\frac{\partial L_b(\lambda)}{\partial\lambda}\right|^{-1}. \tag{2.31}$$

Calculations done by Blake *et al* (1987) have shown that flexural waves will couple light from one mode to the other with 100% efficiency over a length L_i given by

$$L_i = \frac{\pi}{2}L_b\frac{a_c}{u_f}, \tag{2.32}$$

where a_c is the fiber core radius and u_f is the transverse acoustic wave amplitude (ENGAN *et al*, 1988).

Most applications of flexural acoustic wave that causes changes in properties of optical fiber are based on the combination of the tapered optical fiber and the transverse excitation of a fiber. Birks *et al* (1994) introduced a low power acousto-optic device based on a tapered single-mode fiber. Unlike earlier designs, Birks *et al* (1994) optimized the device and the overlap between the acoustic and optical waves was complete, so very little acoustic power was required. The resonance condition for an optimum coupling can be written with the help of Blake *et al* (1988) formulation as

$$a^3 = \frac{\left(j_{11}^2 - j_{01}^2\right)^2}{64\pi^3}\frac{c_{ext}\lambda^2}{n_{eff}^2}, \tag{2.33}$$

where a is the fiber radius, j_{lm} is the *m*th zero of the Bessel function $J_{lm}(z)$ corresponding to the *lm*th mode of the fiber and $c_{ext} = 5740$ m/s is the speed of extensional waves in silica. The acousto-optic coupling coefficient can then be calculated as

$$\kappa = \frac{\left(j_{11}^2 - j_{01}^2\right)^2}{8\sqrt{2}\pi j_{01}j_{11}}\frac{c_{ext}}{(1+\chi)n_{eff}}\frac{\lambda}{L_i f_s}, \tag{2.34}$$

where $\chi = -0{,}22$. As a practical example let us consider a taper carrying light from an HeNe laser at $\lambda = 633$ nm. For resonance at $f_s = 2$ MHz, the required tapered diameter is $a = 3$ μm. If $l_g = 50$ mm, the acoustic amplitude required for 100% coupling is $u_f = 8$ nm. The expected FWHM optical bandwidth is $\Delta\lambda = 1{,}64$ nm. Figure 2.15 shows the schematic diagram of the acousto-optic device, showing the fundamental (LP_{01}) mode spreading from the core to match the cladding (LP_{11}) mode after the interaction length.
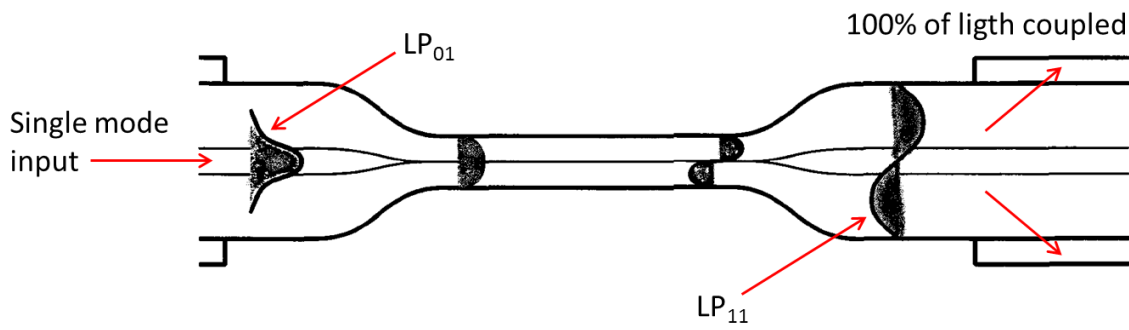
Figure 2.15 - Acousto-optic coupling in a single-mode fiber taper, when the acoustic amplitude is adjusted to give 100% efficient coupling from LP_{01} to LP_{11} modes (BIRKS _et al_, 1994).

The frequency f_s of a flexural acoustic wave is given by the RF signal driving the PZT transducer. However, the flexural acoustic wavelength λ_s is given by the dispersion relation for flexural waves on a cylindrical rod which, in the low frequency regime, is

$$\begin{aligned}
\lambda_s &\equiv \frac{2\pi}{k_s} \\
&= \sqrt{\frac{\pi a c_{ext}}{f_s}},
\end{aligned} \qquad (2.35)$$

where k_s is the acoustic wave number.

The use of flexural acoustic wave together with diffraction gratings has called the attention of scientists and a large number of effects were studied and devices developed, however, only applications in FBG are found in literature. Huang _et al_ (2000) acoustically generated transversal vibration of a fiber Bragg grating to control its reflectivity level and Liu _et al_ (2000) demonstrated the switching of the reflection band of a fiber Bragg grating through the application of a flexural acoustic wave to the fiber. In their work the acoustic wave is generated by positioning a silica-horn PZT set transversally to the fiber axis, causing microbends in the fiber ($f = 1,3$ MHz). The microbending served as a long period grating for coupling the core and cladding modes and switching the reflection band between the Bragg wavelength and the cladding mode wavelength. Such switching function can be applied to wavelength-division multiplexed add-drop operations in fiber communications. The phenomenon is illustrated in figure 2.16, in which couplings between the forward and back-propagating core and cladding modes with their phase-matching mechanisms are shown. The forward propagating core mode is coupled with the backward propagating core mode through grating phase matching, generating the optical band with center wavelength λ_B. When the acoustic wave is applied, the forward-propagating (backward-propagating) core mode is

coupled with forward-propagating (backward-propagating) cladding mode through the microbending phase matching mechanism (figure 2.16(*a*)). Although part of the signal power can be coupled back to the core modes after it is coupled into the cladding modes, most of it radiates through the propagation of cladding modes. Such a coupling process in either propagation direction leads to the reduction of reflectivity at this wavelength. On the other hand, for the signal at λ_{BS}, grating phase matching results in coupling between forward-propagating core mode and backward-propagating cladding mode. When microbending is generated, the coupling between backward-propagating cladding mode and backward-propagating core mode is phase matched and the outcoupled power at this wavelength is coupled back into the core mode and reflectivity is observed. This reflectivity increases with increasing of the microbending strength (ERDOGAN, 1997).
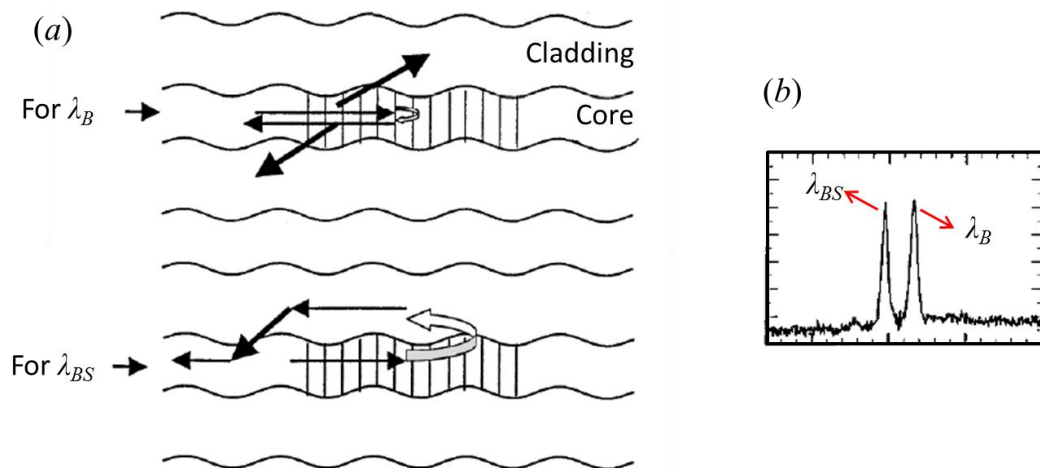
Figure 2.16 - (*a*) Schematic diagram showing the phase-matching mechanism for cladding to core modes coupling. (*b*) Bragg wavelength (λ_B) and λ_{BS} (LIU *et al*,2000).

Using tilted FBG, Chen and Fu (2004) experimentally demonstrated that the induced-wavelength reflection peak can be shifted by adjusting the frequency of the flexural acoustic wave launched into the fiber. Moreover, the acoustic wave can be used to switch the induced-wavelength peak with a wavelength-tuning rate of approximately 1 nm/MHz. Figure 2.17 shows the schematic diagram of the acousto-optic modulation in a tilted FBG.
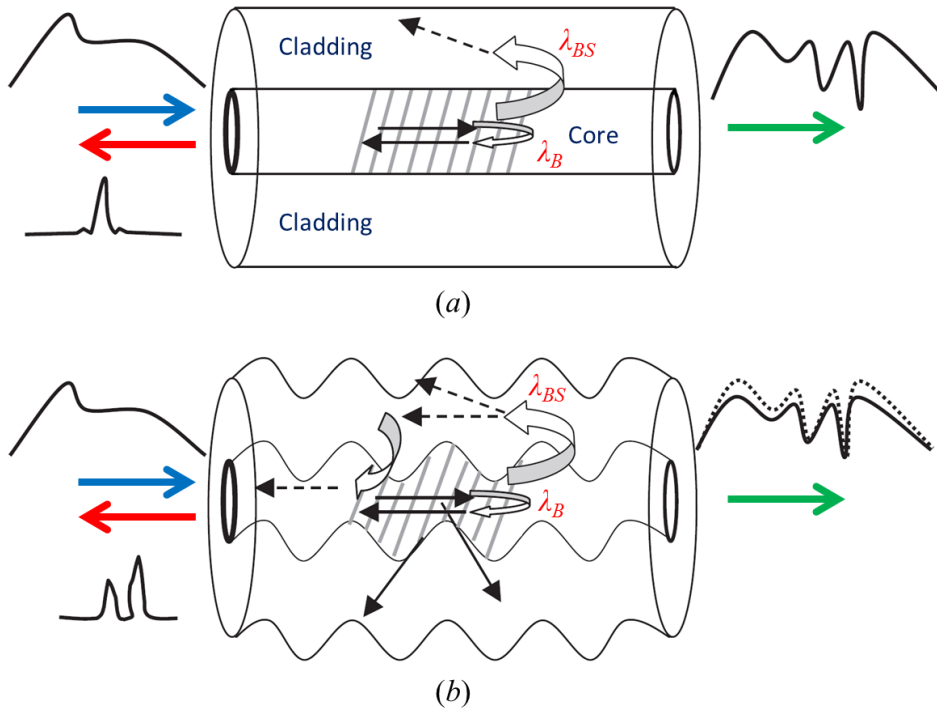
Figure 2.17 - Schematic diagram of the acousto-optic modulation in a tilted FBG: (*a*) without acoustic wave and (*b*) with acoustic wave.

Abrishamian *et al* (2005) presented a simple mathematical formulation to calculate the transmission and reflection spectra of propagating core and cladding modes through the acoustically induced FBG by solving multimode coupling equations. The formulation is based on the transfer matrix method (TMM), which splits the grating into short sectioned pieces so making the process of calculation the fastest for solving two coupled-mode equations (YAMADA and SAKUDA, 1987). The equation to calculate the switched wavelength generated by the acoustic wave in the FBG reflection spectrum (λ_{BS}) is written as

$$\lambda_{BS} = 2\Lambda \left[1 \pm m \left(\frac{\Lambda}{\lambda_s} \right) \right] n_{eff} \quad (m = 1, 2, 3, \ldots). \tag{2.36}$$

Other examples of the combined flexural waves and fiber diffraction gratings and/or acoustically generated gratings can be found in Haakestad and Egan (2006) and in Yeom *et al* (2007), where photonic crystal fibers were explored under acousto-optic interaction using flexural acoustic waves.

3   METHODOLOGY

Numerical simulations were performed to compare results obtained from experiments, to demonstrate the suitability of some numerical methods and develop a tool for design of acousto-optic modulators. Oliveira *et al* (2008a) showed the combination of the finite element (FEM) and transfer matrix (TMM) methods to calculate the acousto-optic modulation of fiber Bragg gratings. The simulation results were compared with literature data and found to be in good agreement. Neves Jr. (2008) introduced the combination of the TMM and the assumed modes method (AMM), which gives information for the transient and steady-state regime. In this work, these methods were used and experimental and practical results valued the combination of the employed numerical methods. Simulations using a commercial software package based on the FEM with a graphical interface were also performed in order to calculate the excited vibration modes of the silica horn-optical fiber set.

Both FEM and AMM are methods used to calculate the strain field experienced by the fiber when it is acoustically excited. However, there are some differences between the methods that should be clarified. FEM is a general method, used for a variety of problems such as static, dynamic, linear, nonlinear and so on. Its formulation is based on the construction of numerical matrices for each element, which causes the requirement of elevate computational performance. On the other hand, AMM is only applicable for dynamics problems where an orthonormal basis that satisfies all boundary conditions is known. This basis is composed by the natural vibration modes of the system, which are valid to the whole domain, in contrast with the interpolation equations used in FEM. As a consequence, in the AMM, the dimension of the generated matrices is smaller, because each variable is associated to a basis function, making the computational costs lower and the results achieved more accurate.

3.1   NUMERICAL MODELING

The dimensions of the structure employed in the calculation are shown in figure 3.1, which correspond to the ones of the assembled device. The length of the silica horn is $l_{sh} = 46$ mm, with a base diameter of $d_{sh} = 8$ mm and tip diameter of $d_{sht} = 0,8$ mm. The length of the fiber is taken as the FBG length, usually $l_g = 50$ mm.
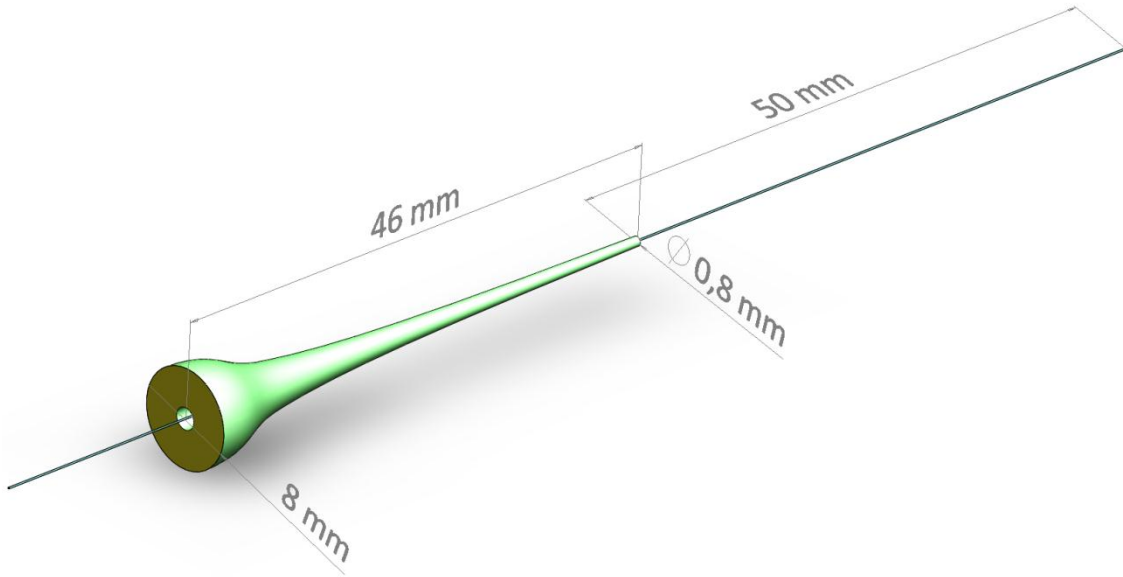
Figure 3.1 - Silica horn and FBG dimensions used in the numerical simulations.

3.1.1   Finite element method

The FEM was introduced in the late 1950s and presents several advantages, such as a widespread acceptance in the scientific and industrial community, the capability of modeling complex geometries, the consistent treatment of differential-type boundary conditions, and the possibility to be programmed in a flexible and general purpose format (HUGHES, 1987). Standard finite element approximations are based upon the Galerkin formulation of the weighted residuals method (ZIENKIEWICZ and TAYLOR, 2000).

The differential equation of motion that represents the acoustic wave propagation in the structure is given by

$$E\frac{\partial}{\partial z}\left(A(z)\frac{\partial u(z,t)}{\partial z}\right) - \rho A(z)\frac{\partial^2 u(z,t)}{\partial t^2} = 0, \tag{3.1}$$

where E is the Young´s modulus, u is the axial displacement, which is dependent on the position z and time t, $\frac{\partial u}{\partial z} = \varepsilon$ is the longitudinal strain and ρ is the density. The term $A(z)$ represents the variable size of the structure along the z-axis. In the current analysis, the damping of the acoustical wave in the structure is neglected.

The initial and boundary conditions are given by

$$\begin{cases} \left[AE\dfrac{du}{dz}\right]_{z=0} = P(t) = P_0\exp(j\omega t) \\ u(z=l_t,t) = 0 \end{cases}, \tag{3.2}$$

where $P(t)$ is the external excitation, composed by the harmonic load frequency ω and amplitude P_0 generated by the PZT transducer. l_t represents the total length of the device.

A classical linear basis approach for the finite elements is used in this work. After the one-dimensional discretization, the final matrix form of the problem is given by

$$\mathbf{M\ddot{u}} + \mathbf{Ku} = \mathbf{P}. \tag{3.3}$$

In this expression, $\mathbf{M}$ and $\mathbf{K}$ are the mass and stiffness matrices of the structure, obtained by the superposition of the mass and stiffness matrix of each element, which are given by

$$\mathbf{M} = \left[m_{ij}^e \right] = \frac{\rho A^e \Delta z}{2} \begin{bmatrix} 1 & 0 \\ 0 & 1 \end{bmatrix} \tag{3.4}$$

and

$$\mathbf{K} = \left[k_{ij}^e \right] = \frac{A^e E}{\Delta z} \begin{bmatrix} 1 & -1 \\ -1 & 1 \end{bmatrix} \tag{3.5}$$

respectively. The superscript e represents an element with particular properties. Furthermore, $\mathbf{u}$ and $\ddot{\mathbf{u}}$ in (3.3) represent the nodal displacement and acceleration vectors, respectively. The vector $\mathbf{P}$ is the nodal generalized force and has a null value, except for the first component, associated with the node at $z = 0$. Considering the excitation in the form of $\mathbf{P} = \mathbf{P}_0 \exp\left(j\omega t \right)$ and assuming that the system behaves linearly, the solution of the problem can be found solving the equation:

$$\mathbf{M\ddot{u}} + \mathbf{Ku} = \mathbf{P}_0 \exp\left(j\omega t \right). \tag{3.6}$$

Since the time dependent load generated by the piezoelectric is harmonic, the solution has the form $\mathbf{u} = \mathbf{u}_0 \exp\left(j\omega t \right)$. This way, (3.6) is reduced to

$$\left(-\omega^2 \mathbf{M} + \mathbf{K} \right) \mathbf{u}_0 = \mathbf{P}_0. \tag{3.7}$$

Note that $\mathbf{u}_0$, the displacement vector solution, is highly dependent on the amplitude $\mathbf{P}_0$ and frequency ω of the acoustic excitation.

Once the displacement field is obtained, the strain field in each one of the finite elements can be found by differentiation, as

$$\varepsilon^e = \frac{\partial u}{\partial z} \cong \frac{u^{e+1} - u^e}{\Delta z}. \tag{3.8}$$

In this case, as the properties of the finite element are linear, u^{e+1} and u^e are the displacements in the local nodes $e+1$ and e, respectively.

3.1.2 Assumed modes method

The AMM is based on the discretization of a system consisting of n elements and n degrees of freedom in order to find approximated solutions through numerical series (NEVES JR., 2008). For a particular case, where movement is only observed in one direction (for example, movements originated by pulling the fiber longitudinally), one can assume that the solution of a problem with known boundary conditions will be found through a product between a conveniently chosen spatial function and a temporal function. For a length of fiber treated as a thin cylindrical, linear, homogeneous bar, if one wishes to find the space-time dependent displacement behavior, the displacement function $u(z,t)$, and consequently the strain (ε), is obtained considering the solution for

$$u(z,t) = \sum_{j=1}^{n} \varphi_j(z) q_j(t),\qquad(3.9)$$

where $\varphi_j(z)$ is called the trial or assumed modes function, which is chosen in order to satisfy all boundary conditions of the problem and must be differentiable at least for half of the system order (MEIROVITCH, 1986). Thus, for a system described as a bar of length l_t with non-uniform transversal section, similar to the structure of the acousto-optic modulator showed in figure 2.9, an appropriate trial function could be

$$\varphi_j(z) = \sin\left[\frac{(2j-1)\pi z}{2l_t}\right]\qquad j = 1, 2, ..., n .\qquad(3.10)$$

In equation (3.9), $q_j(t)$ is the generalized coordinates vector of a system of differential equations described by

$$\mathbf{M}\{\ddot{q}(t)\} + \mathbf{K}\{q(t)\} = \{f(t)\},\qquad(3.11)$$

where $\mathbf{M}$ and $\mathbf{K}$ are the $n \times n$-order mass and stiffness matrixes respectively, and $\{f(t)\}$ is the generalized excitation vector. From equation (3.9), one can see that the solution is found as a linear combination of a base in the n-dimensional space. A solution for equation (3.11) can be found considering $f(t) = \sin(\omega t)$ either for transient or steady state regimes (NEVES JR., 2008). The strain field $\varepsilon(z,t)$, necessary for calculating the grating spectrum with the TMM, is simply found differentiating (3.9) with respect to z.

More details on the method formulation can be found in Appendix A, Neves, Jr. (2008) and Neves Jr. *et al* (2008).

3.1.3   Transfer matrix method

3.1.3.1   Reflection grating – The FBG case

Once the strain field for the steady-state regime is known along the fiber and, particularly, along the grating, one can calculate the optical response following the schematic diagram showed in figure 3.2. Note that the grating properties have to be adjusted to fit the simulated spectrum with the experimental one, in order to calculate the properties of the experimental grating.

As mentioned in section 2.1.1.2, for a uniform grating, the effective refractive index perturbation in the core is described by equation 2.2, and repeated here for convenience

$$\delta n_{eff}(z) = \delta n_0(z)\left[1 + v\cos\left(\frac{2\pi}{\Lambda}z + \phi(z)\right)\right]. \tag{3.12}$$

As the grating imposes a dielectric perturbation to the waveguide core, it forces coupling between the propagating modes. The formulation of the coupled-mode equations due to the index perturbation are found with the help of the "synchronous approximation" described by Kogelnick (1990), Hill and Meltz (1997) and Kashyap (1999). This approximation is represented by a set of coupled first-order differential equations written as

$$\frac{dR}{dz} = i\hat{\psi}R(z) + i\vartheta S(z) \tag{3.13}$$

$$\frac{dS}{dz} = -i\hat{\psi}S(z) - i\vartheta^* R(z), \tag{3.14}$$

where $R(z)$ and $S(z)$ represent the propagating and counter-propagating modes, respectively, which are given by

$$R(z) \equiv A(z)e^{\left(i\xi z - \frac{\phi}{2}\right)} \tag{3.15}$$

$$S(z) \equiv B(z)e^{\left(-i\xi z + \frac{\phi}{2}\right)}, \tag{3.16}$$

where $A(z)$ and $B(z)$ represents the amplitudes of the co-propagating and counter-propagating modes, respectively. In these equations $\hat{\psi}$ represents the general "dc" self-coupling coefficient, which is defined as

$$\hat{\psi} = \xi + \psi, \tag{3.17}$$

where ψ is the "dc" coupling coefficient, defined by

$$\psi = \frac{2\pi}{\lambda}\delta n_0, \tag{3.18}$$

and ϑ is the "ac" coupling coefficient given by

$$\vartheta = \frac{v}{2}\psi. \tag{3.19}$$

The term ξ, called detuning (ERDOGAN, 1997) is defined as

$$\xi = 2\pi n_{eff}\left(\frac{1}{\lambda} - \frac{1}{\lambda_D}\right), \tag{3.20}$$

where $\lambda_D \equiv 2n_{eff}\Lambda$ is the "design wavelength" for a Bragg scattering within an infinitesimal variation of the effective index $(\delta n_{eff} \to 0)$, i.e., a grating that is infinitely weak (ERDOGAN, 1997).

The amplitude and power reflection coefficients

$$\zeta = \frac{S\left(-\frac{l_g}{2}\right)}{R\left(-\frac{l_g}{2}\right)} \tag{3.21}$$

and

$$\hat{\zeta} = |\zeta|^2, \tag{3.22}$$

can be shown to be

$$\zeta = \frac{-\vartheta\sinh\left(\sqrt{\vartheta^2 - \hat{\psi}^2}\,l_g\right)}{\hat{\psi}\sinh\left(\sqrt{\vartheta^2 - \hat{\psi}^2}\,l_g\right) + i\sqrt{\vartheta^2 - \hat{\psi}^2}\,l_g\cosh\left(\sqrt{\vartheta^2 - \hat{\psi}^2}\,l_g\right)} \tag{3.23}$$

and

$$\hat{\zeta} = \frac{\sinh^2\left(\sqrt{\vartheta^2 - \hat{\psi}^2}\,l_g\right)}{\cosh^2\left(\sqrt{\vartheta^2 - \hat{\psi}^2}\,l_g\right) - \frac{\hat{\psi}^2}{\vartheta^2}}, \tag{3.24}$$

respectively. From (3.24), the maximum reflectivity $\hat{\zeta}_{max}$ for a Bragg grating is

$$\hat{\zeta}_{max} = \tanh^2\left(\vartheta l_g\right), \tag{3.25}$$

and it occurs when $\hat{\psi} = 0$, or at the wavelength

$$\lambda \cong \left(1 + \frac{\delta n_0}{n_{eff}}\right)\lambda_D, \tag{3.26}$$
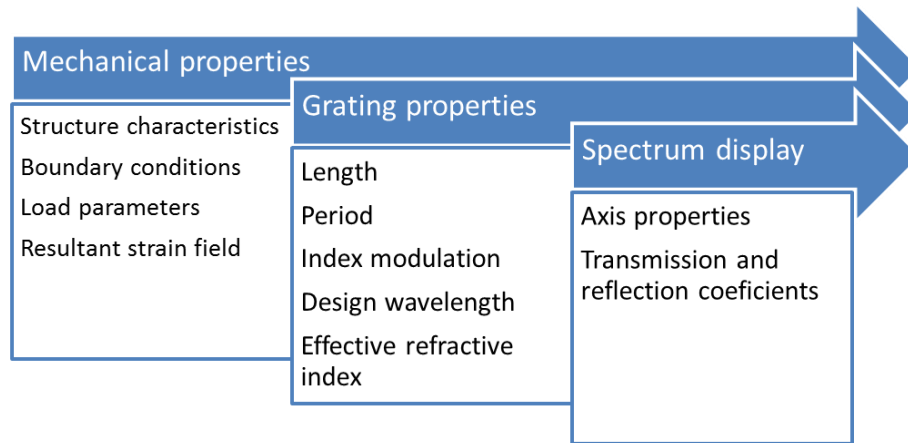
Figure 3.2 – Schematic diagram for the calculation of the resultant grating spectra.

This description represents the situation for a uniform grating, where the average refraction index change is constant. However, the onset of the acoustical wave causes a broadening in the grating, making its pitch non-uniform and changing the optical path. Considering the non-uniformity of the grating, the reflection and transmission spectra from the two-mode coupling can be calculated by considering a piecewise approach, whereby the grating is divided into discrete uniform sections that are individually represented by a matrix. The solution is found by multiplying the matrices associated with each one of the sections. The characteristic equation is solved by making the matrix determinant equal to zero and the resulting polynomial enables the eigenvalues to be found.

The FBG of length l_g can be treated as a quadrupole, as show in figure 3.3, where R and S represent the co-propagating and counter-propagating modes, respectively. For convenience, the amplitude $R(0)$ of the incident wave is normalized, in such a way that the maximum value is equal to unit at the origin ($z = 0$).
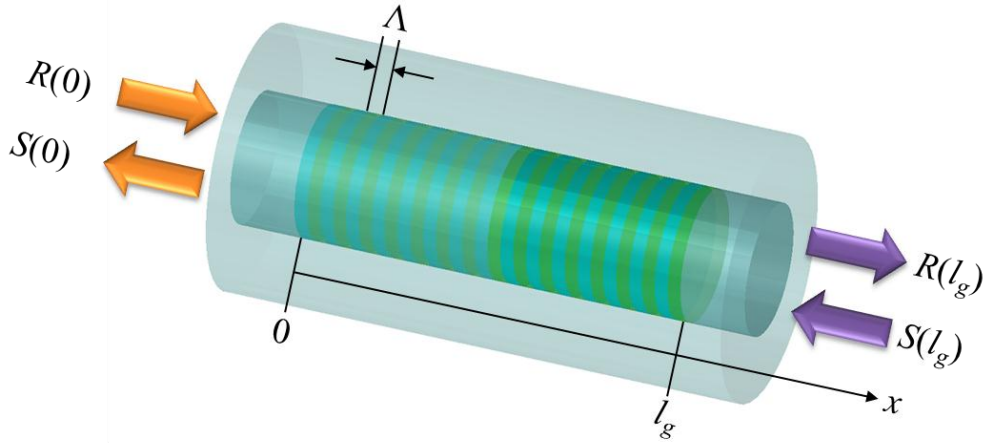
Figure 3.3 - Bragg grating schematic as a quadrupole. *R* and *S* represent the co-propagating and counter-propagating modes, respectively.

Splitting the grating in M uniform sections and defining R_j and S_m as amplitudes of the fields across the section j, the propagation through the section is described by the equation

$$\begin{bmatrix} R_j \\ S_j \end{bmatrix} = \mathbf{F}_j^B \begin{bmatrix} R_{j-1} \\ S_{j-1} \end{bmatrix},$$ (3.27)

where $\mathbf{F}_j^B$ is a 2×2 matrix given by (ERDOGAN, 1997)

$$\mathbf{F}_j^B = \begin{bmatrix} \cosh(\gamma_B \Delta z) - i\dfrac{\hat{\psi}}{\gamma_B}\sinh(\gamma_B \Delta z) & -i\dfrac{\vartheta}{\gamma_B}\sinh(\gamma_B \Delta z) \\ i\dfrac{\vartheta}{\gamma_B}\sinh(\gamma_B \Delta z) & \cosh(\gamma_B \Delta z) + i\dfrac{\hat{\psi}}{\gamma_B}\sinh(\gamma_B \Delta z) \end{bmatrix},$$ (3.28)

where Δz is the length of the j-th uniform section and

$$\gamma_B \equiv \sqrt{\vartheta^2 - \hat{\psi}^2} \,.$$ (3.29)

The coefficients $\hat{\psi}$ and ϑ have local values at the j-th section.

Since the matrices for each section are known, the application of the boundary conditions, $R(0)=1$ for $z \leq 0$ and $S(l_g)=0$ for $z \geq l_g$, allows the final equation to be described as

$$\begin{bmatrix} R(0) \\ S(0) \end{bmatrix} = \mathbf{F}^B \begin{bmatrix} R(L) \\ S(L) \end{bmatrix} \quad \Rightarrow \quad \begin{bmatrix} 1 \\ S(0) \end{bmatrix} = \mathbf{F}^B \begin{bmatrix} R(L) \\ 0 \end{bmatrix},$$ (3.30)

where

$$\mathbf{F}^B = \prod_{j=1}^{m} \mathbf{F}_j^B \,.$$ (3.31)

Writing $\mathbf{F}_j^B$ in the form of

$$F_j^B = \begin{bmatrix} f_{11} & f_{12} \\ f_{21} & f_{22} \end{bmatrix} \tag{3.32}$$

and substituting it in (3.30), the result is

$$\begin{bmatrix} 1 \\ S(0) \end{bmatrix} = \begin{bmatrix} f_{11}R(l_g) \\ f_{21}R(l_g) \end{bmatrix}. \tag{3.33}$$

From (3.33) one concludes that $R(l_g) = 1/f_{11}$. Therefore, the reflected amplitude for each wavelength can be found as

$$\varsigma(\lambda) = \frac{S(0)}{R(0)} = \frac{S(0)}{1} = \frac{f_{21}}{f_{11}}, \tag{3.34}$$

and the reflected power will be given by $\hat{\varsigma}(\lambda) = |\varsigma(\lambda)|^2$.

Similarly, the transmitted amplitude will be given by

$$\tau(\lambda) = \frac{R(L)}{R(0)} = \frac{R(L)}{1} = \frac{1}{f_{11}}, \tag{3.35}$$

and the transmitted power by $\hat{\tau}(\lambda) = |\tau(\lambda)|^2$.

In addition, the group delay and dispersion of the reflected light is determined from the phase, $\theta \equiv phase\ (\varsigma)$, of the amplitude reflection coefficient ς. Moreover, since the first derivative $d\theta/d\varpi$ is directly proportional to the optical frequency ϖ, it can be identified as the time delay t_{delay} (in ps). In this way, the dispersion coefficient D (in ps/nm) is defined as the rate of change of time delay with wavelength and is given by

$$D = \frac{dt_{delay}}{d\lambda} = -\frac{2\pi c}{\lambda^2} \frac{d^2\theta}{d\varpi^2}, \tag{3.36}$$

where c is the speed of light in vacuum. The dispersion slope, D_s (ps/nm^2), is given by

$$D_s = \frac{dD}{d\lambda}. \tag{3.37}$$

3.1.3.2 Transmission grating – The LPG case

The TMM formulation applied for transmission gratings is similar to the one presented for reflection grating. The change is that, instead of considering the energy coupled to a counter-propagating mode, the light is coupled to a co-propagating mode, for instance light propagating in mode "1" being coupled to a co-propagating mode "2". Figure 3.4 shows

the quadrupole characteristics of the LPG (figure 3.3 modified), where now R represents the amplitude of the forward propagating mode and S the amplitude of the co-propagating field to which the entering forward mode is coupled to, given by

$$R(z) \equiv A_1 e^{\left[-i\frac{(\psi_{11}+\psi_{22})z}{2} \right]} e^{\left(i\xi z - \frac{\phi}{2} \right)} \tag{3.38}$$

$$S(z) \equiv A_2 e^{\left[-i\frac{(\psi_{11}+\psi_{22})z}{2} \right]} e^{\left(-i\xi z + \frac{\phi}{2} \right)}. \tag{3.39}$$

In these equations, the "dc" coupling coefficients are defined by

$$\psi_{kj}(z) = \frac{\varpi n_{eff}}{2} \delta n_0(z) \iint\limits_{core} \vec{e}_{kt}(x,y) \cdot \vec{e}_{jt}^{\,*}(x,y) \, dx \, dy, \tag{3.40}$$

where $\vec{e}_{kt}$ represents the transverse mode fields (ERDOGAN, 1997). The general "dc" self-coupling coefficient $\hat{\psi}$ is defined as

$$\hat{\psi} \equiv \xi + \frac{(\psi_{11}-\psi_{22})}{2} - \frac{1}{2}\frac{d\phi}{dz}, \tag{3.41}$$

and the detuning coefficient, which is assumed to be constant along z, is

$$\xi = \pi \delta n_{eff} \left(\frac{1}{\lambda} - \frac{1}{\lambda_D} \right). \tag{3.42}$$

where $\lambda_D = \delta n_{eff} \Lambda$ is the design wavelength for an infinitesimally weak grating. As for Bragg gratings, $\xi = 0$ corresponds to the grating condition predicted by the qualitative picture of grating diffraction, or $\lambda = \delta n_{eff} \Lambda$ (ERDOGAN, 1997).
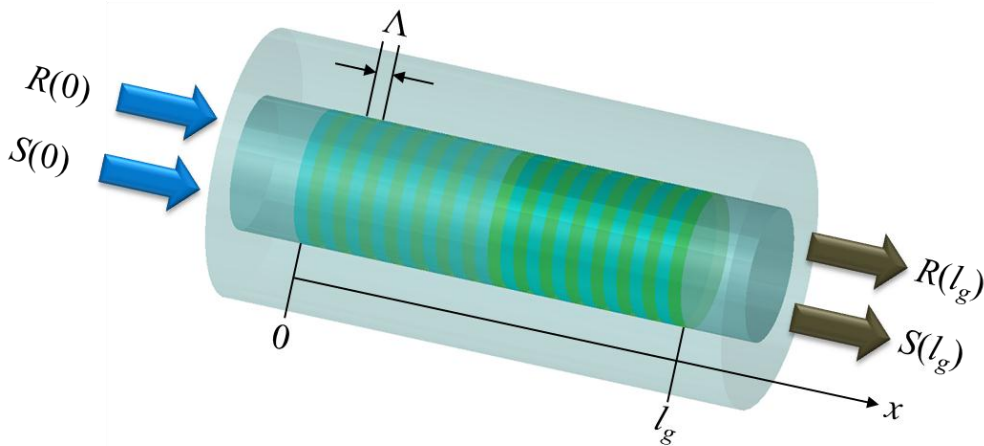
Figure 3.4 - LPG represented as a quadrupole in the TMM.

For a uniform long period grating $\hat{\psi}$ and ϑ are constants, however, ϑ cannot be written simply as in (3.19). For coupling between two different modes the overlap integral (3.40) must be evaluated numerically. Like the analogous Bragg-grating equations, (3.13) and (3.14) are coupled first-order ordinary differential equations with constant coefficients. Thus, closed-form solutions can be found when appropriate initial conditions are specified. The transmission can be found by assuming only one mode is incident from $z = -\infty$ (i.e. $R(0) = 1$ and $S(0) = 0$). The respective power bar and cross transmission

$$ t_= = \frac{|R(z)|^2}{|R(0)|^2} \tag{3.43} $$

and

$$ t_\times = \frac{|S(z)|^2}{|R(0)|^2}, \tag{3.44} $$

can be shown to be (YARIV, 1973)

$$ t_= = \cos^2\left(\sqrt{\vartheta^2 + \hat{\psi}^2}\, z\right) + \frac{1}{1 + \dfrac{\vartheta^2}{\hat{\psi}^2}} \sin^2\left(\sqrt{\vartheta^2 + \hat{\psi}^2}\, z\right) \tag{3.45} $$

and

$$ t_\times = \frac{1}{1 + \dfrac{\hat{\psi}^2}{\vartheta^2}} \sin^2\left(\sqrt{\vartheta^2 + \hat{\psi}^2}\, z\right), \tag{3.46} $$

respectively. The maximum cross transmission (which occurs when $\hat{\psi} = 0$) is found to be

$$ t_{\times,\max} = \sin^2\left(\vartheta l_g\right), \tag{3.47} $$

and it occurs at the wavelength

$$ \lambda = \frac{1}{1 - (\psi_{11} - \psi_{22})\dfrac{\Lambda}{2}} \lambda_D. \tag{3.48} $$

For coupling between a core mode and a cladding mode with an induced index change in the core only, $\psi_{11} = \psi$ from (3.40), $\psi_{22} \ll \psi_{11}$. Therefore, (3.48) can be approximated as

$$ \lambda \cong \left(1 + \frac{\delta n_0}{\delta n_{eff}}\right)\lambda_D, \tag{3.49} $$

where $\delta n_0 \ll \delta n_{eff}$.

The matrix formulation for the transmission grating case is similar to the one presented in section 3.1.3.1, differing only for some coefficients. For transmission gratings the matrix $\mathbf{F}_j^c$ is written as

$$\mathbf{F}_j^c = \begin{bmatrix} \cos\left(\gamma_c \Delta z\right) - i\dfrac{\hat{\psi}}{\gamma_c}\sin\left(\gamma_c \Delta z\right) & -i\dfrac{\vartheta}{\gamma_c}\sin\left(\gamma_c \Delta z\right) \\[2ex] i\dfrac{\vartheta}{\gamma_c}\sin\left(\gamma_c \Delta z\right) & \cos\left(\gamma_c \Delta z\right) + i\dfrac{\hat{\psi}}{\gamma_c}\sin\left(\gamma_c \Delta z\right) \end{bmatrix}, \tag{3.50}$$

where

$$\gamma_c \equiv \sqrt{\vartheta^2 + \hat{\psi}^2}\ . \tag{3.51}$$

3.1.4   The combination of the mechanical and optical methods

The combination of the numerical approaches, mechanical and optical, is made through the wavelength shift in every single segment of the fiber (element) submitted to the strain field ε, as written in equation (2.5) for the Bragg grating case and in equation (2.14) for the LPG case (QIN $et\ al$, 2000). These relations are found to be

$$\Delta\lambda_B\left(z\right) = \lambda_{B0}\left[1 + \left(1 - p_e\right)\varepsilon_z\right] \tag{3.52}$$

and

$$\Delta\lambda_m\left(\varepsilon_z\right) = \lambda_m\left[1 + \left(1 + p\right)\varepsilon_z\right] \tag{3.53}$$

for the FBG and LPG case, respectively. Equations (3.52) and (3.53) accounts for both the effect of the period variation and the change in the effective refractive indices due to the strain field in each point inside the grating through the strain-optic effect. However, in the FBG case, the predominant effect is the displacement of the modulation planes, while for the LPG, changes in the effective index and optical path are the main effects. These methods simulate the excitation of longitudinal and flexural modes in the fiber through the projection of the displacement field in the one dimensional space. A thorough description of how the numerical methods and TMM are used together is found in Oliveira $et\ al$ (2008a), Oliveira (2008b) and in Neves Jr. (2008).

3.1.5   3-D finite element simulation

The numerical approaches AMM, FEM and TMM help to calculate the optical spectra, but do not give information on the way the acoustic wave affects the fiber, i.e. which mechanical modes are generated. For this purpose a commercial finite element software

package with graphical interface is used in order to calculate and visualize the excited vibration modes of the silica horn / optical fiber set used in the experiments. The model was constructed based on the device real dimensions, similar to the one shown in figure 3.1. By means of this software, it is possible to access the natural vibration modes being excited in the fiber (flexural, longitudinal, torsional, or hybrid, i.e. a combination of them), depending on the acoustic frequency applied to the base of the silica horn (OLIVEIRA *et al*, 2010a; OLIVEIRA *et al*, 2009b).

3.2   EXPERIMENTAL SET-UP

This section describes the device and the experimental setup, which are the basis of all results obtained employing the acousto-optic modulation effect.

3.2.1   The Acousto-optic modulator

Each one of the components of the modulator presents its particular characteristics. The main portion of the modulator is shown in figure 3.5. The device consists of a piezoelectric (PZT) disc, a silica horn and a fiber, which contains the grating, so built that it allows the transmission and reflection spectra to be measured.
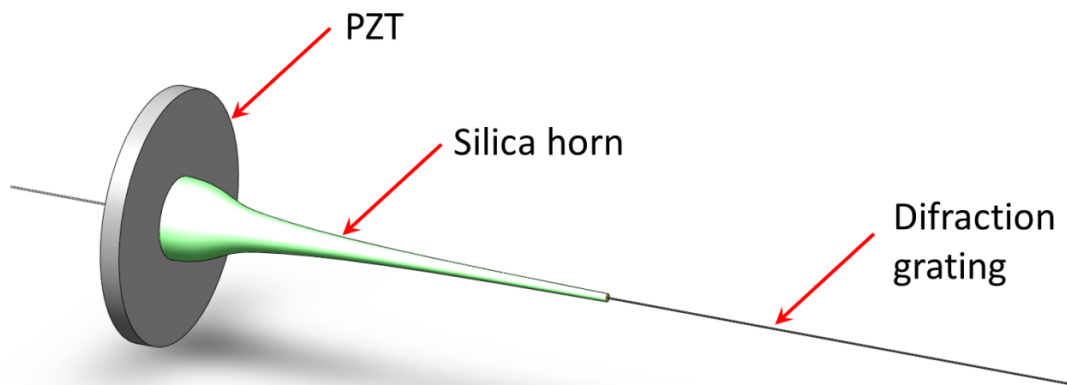
Figure 3.5 - The acousto-optic modulator.

Each part of the modulator is presented separately, and the whole experimental assembly is discussed at the end. This helps to understand the function of each one of the components.

3.2.1.1 The piezoelectric disc

In order to create an acoustic perturbation in the fiber it is essential to use an acoustic transducer or even an ultrasound transducer. The most common acoustic wave generator is the piezoelectric transducer (PZT), which is based on the piezoelectric effect, first reported by Pierre and Jacques Curie in 1880 (LIPPMAN, 1881; JAFFE, 1958). They described changes of the physical dimensions of specific materials when an electric field is applied on them. Additionally, the effect was found to be reversible (works the other way around), i.e. the application of strain to a piece of material generates an electrical field.

Usually, PZTs are made of a ceramic material, and it is shaped for specific applications. For example, the PZT used in this work is a ceramic disc with $d_{PZT} = 25$ mm diameter, and $t_{PZT} = 2$ mm thick, in order to achieve resonance frequencies around $f = 1$ MHz. A hole of diameter $d_h = 1$ mm was drilled in order to allow the fiber pass through the disc. Some of the discs were fabricated by *Physik Instrumente* (PI, 2010). The chosen element was the PIC 151, which is a part of the so called "soft" PZTs, composed by zirconate and titanate materials with high permittivity, so high coupling factor and high piezoelectric charge constant. This material is the standard composition of most actuators and employed in low-power ultrasonic transducers and low-frequency sound transducers (PI, 2010).

The resonance frequencies of one of the ceramics were measured with an impedance analyzer. The used instrument was an Agilent 4294A Precision Impedance Analyzer. Figure 3.6 shows graphs of impedance and phase over frequency for the PZT used in the work. Figure 3.6(*a*) shows the behavior considering the frequency range from 0 to 1,2 MHz, while figure 3.6(*b*) shows a zoom in low frequencies (50 to 100 kHz). Several resonances are observed, however, the most evident one is around $f = 1$ MHz (the condition of resonance is straightforward and it is characterized by minimum impedance and zero phase).
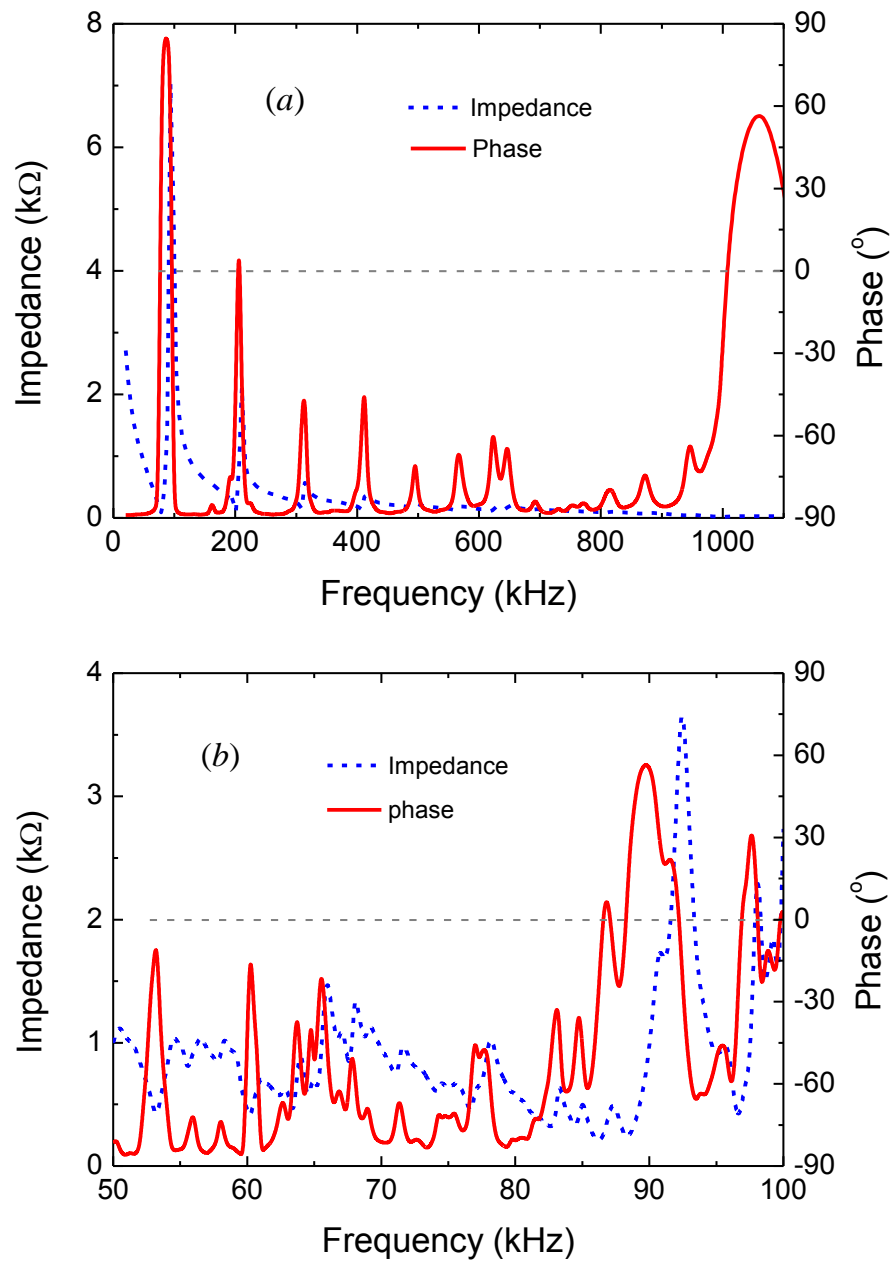
Figure 3.6 - Frequency characterization of the PZT ceramic used in the experiments in the range from (*a*) 0 to 1,2 MHz and (*b*) a zoom in the low frequency range, from 50 to 100 kHz.

A Fabry-Perot fiber interferometer for measuring vibration amplitude and resonances was also built in order to verify the amplitudes of the PZT displacement and check the measurement performed with the impedance analyzer. The first resonance peak was analyzed and compared with the value obtained via the impedance and phase measurement. Figure 3.7 shows the first resonance of the PZT, around $f \approx 90$ kHz (also shown in figure 3.6(*a*)). Figure 3.7(*a*) shows the characterization using the extrinsic Fabry-Perot interferometer (EFPI), while figure 3.7(*b*) shows the electronic characterization through the measure of the impedance and

78

phase of the electrical signal. One sees that the measurement performed with the EFPI is consistent with that of the impedance analyzer. The maximum longitudinal displacement measured using the EFPI (considering $V_{PZT} = 10$ V voltage) was $u_{PZT} = 8,4$ nm (SILVA *et al*, 2011), a parameter that cannot be measured with the impedance analyzer.

Along this work, different elements were used, which present different resonance characteristics. However, all of them present the same dimensions, which results in a similar behavior, differing only on the composite material.

3.2.1.2 The Silica horn

The silica horn is used to couple the acoustic energy into the optical fiber, which contains the grating. Liu *et al* (1997) reported the importance of such device to acousto-optic applications. In Liu's device, the silica horn is attached longitudinally to the PZT, allowing the generation of longitudinal waves in the grating. The horn diameter is reduced over its $l_{sh} = 70$ mm length from $d_{sh} = 3$ mm (base diameter) to $d_{sht} = 125$ μm (tip diameter), and then fused to the grating.

Oliveira *et al* (2008) reported the effect on the acoustic coupling when the dimensions of the horn vary. It was noticed that, as the diameter of the horn base increases, keeping the density of energy applied to the base constant, the strain effect increases, while variation in its length does not affect the final strain field experienced by the grating. The silica horn used in this work was made at the chemistry department of the University of Aveiro, Portugal. The initial horn design was built to follow the specification: larger base diameter and small length, according to the PZT dimensions. The necessity of having a hole to allow the fiber passes though the silica horn, made the choice of a proper capillary tube crucial. Figure 3.8 shows the original capillary tube and the obtained silica horn after the process of pulling. The final dimensions of the silica horn were: base diameter $d_{sh} = 8$ mm, tip diameter $d_{sht} = 0,8$ mm and length $l_{sh} = 46$ mm, as shown in figure 3.1. Figure 3.9 shows a photography of some of the horns and the optimized one (highlighted).
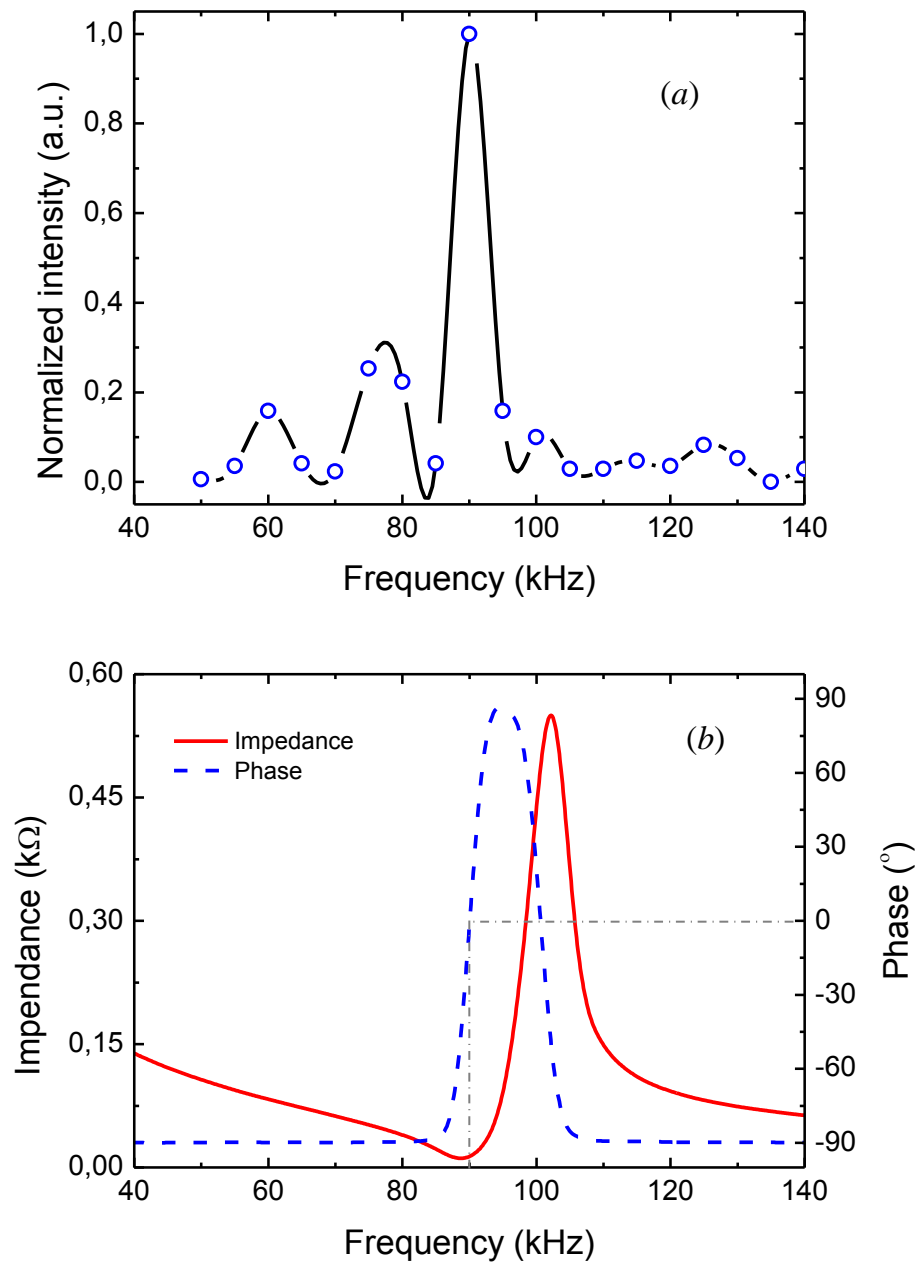
Figure 3.7 - First resonance of the PZT measured by (*a*) the EFPI and (*b*) the impedance analyzer.
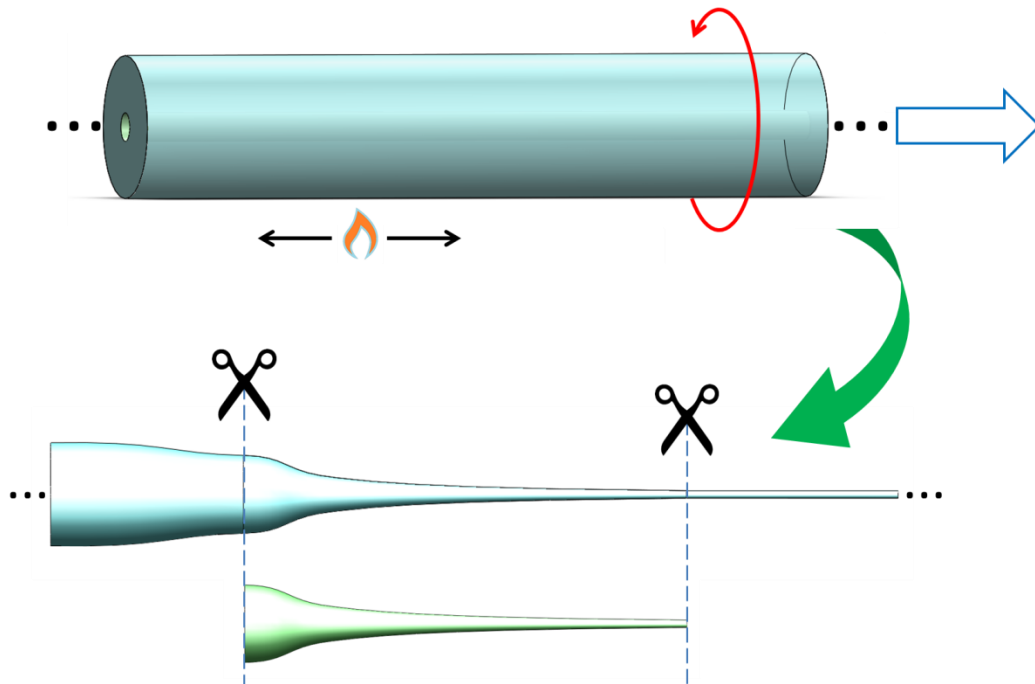
Figure 3.8 - Original capillary tube and the obtained silica horn after the process of pulling.
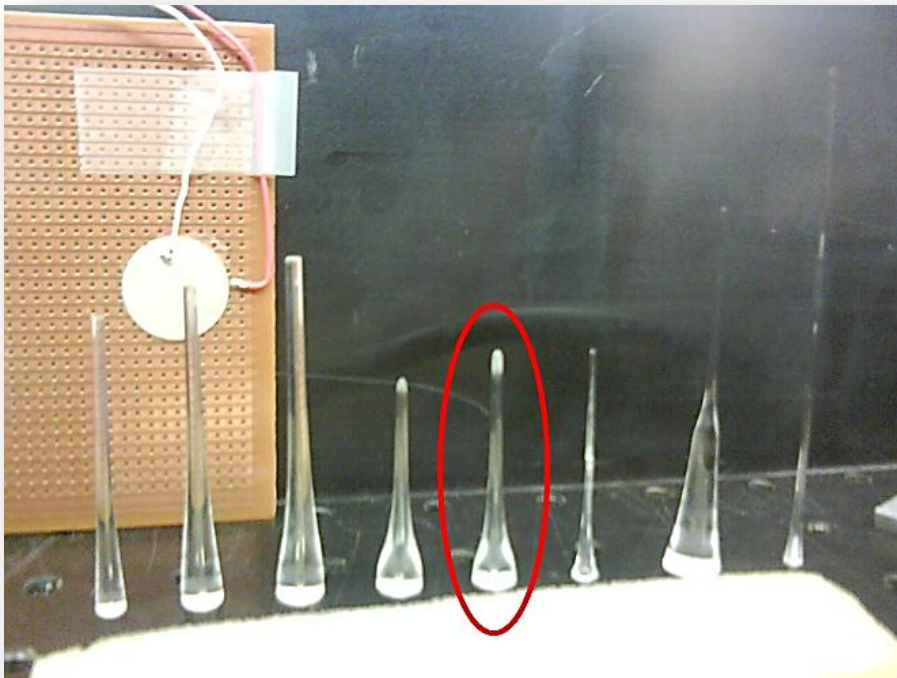
Figure 3.9 - Photography of the fabricated horns. Highlighted, the horn that presented the best performance.

The gratings used in the experiments were written using different lasers in different laboratories. Gratings were written in Brazil, at the LASER laboratory of UTFPR, in Portugal

at the *Instituto de Telecomunicações* of University of Aveiro, and in Australia at the Interdisciplinary Photonics Laboratories (iPL). Usually, the gratings length was chosen to be the longest possible, so to enhance the acousto-optic interaction. However, the available phase masks presented a physical limitation. For example, the longest grating fabricated was an FBG written at iPL by means of a phase mask with $l_{pm} = 50$ mm and an LPG using an amplitude mask with $l_{am} = 50$ mm.

3.2.1.3 The Fixing stages

The fixing stages here are considered as the set formed by the PZT, the silica horn, the fiber with the grating, the holders and the translational stages. The holders are in charge to embrace the set and allow the generation of a stationary wave, i.e. the resonance conditions are given by the holders. The holder set is composed by two aluminum parts, one for the PZT and the other for the optical fiber. Figure 3.10 shows the diagram of the main part of the set, together with its dimensions. The space between the holders, lying between the silica horn and the piece of fiber length is called interaction length, and during the experiments this distance was set to $l_b = 96$ mm.
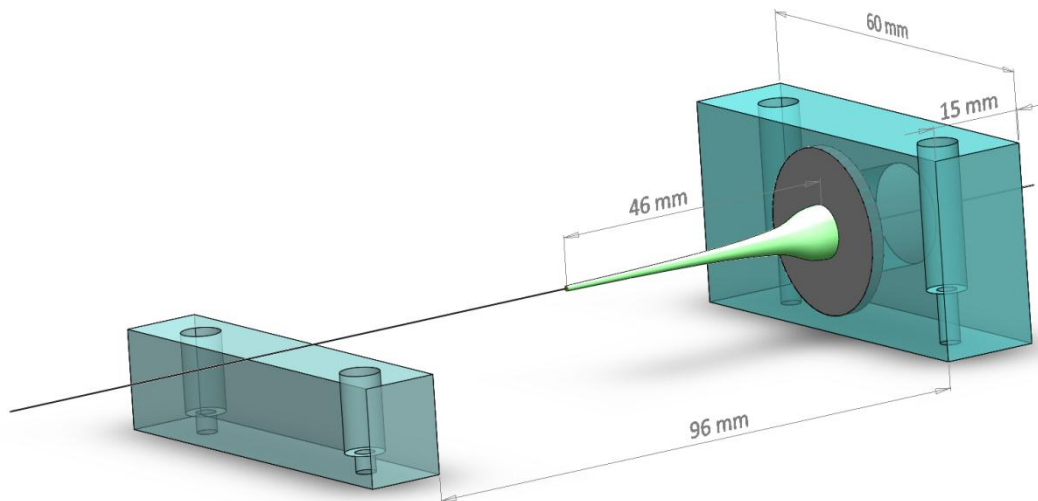
Figure 3.10 - Dimensions of the fixing stages of the acousto-optic modulator.

When assembled, the resonance conditions of the PZT slightly change. This can be noticed measuring again the impedance and phase of the PZT. Figure 3.11 shows the comparison before and after the modulator assembly was put in place. One observes that the resonance conditions changed and some resonances were weakened, however, the frequency of each resonance did not change. Figure 3.12 shows the modulator assembled on top of

translational stages. The translational stages, however, have springs that damp the acoustic wave. This way, the translation stages have to be avoided for dynamic characterization.
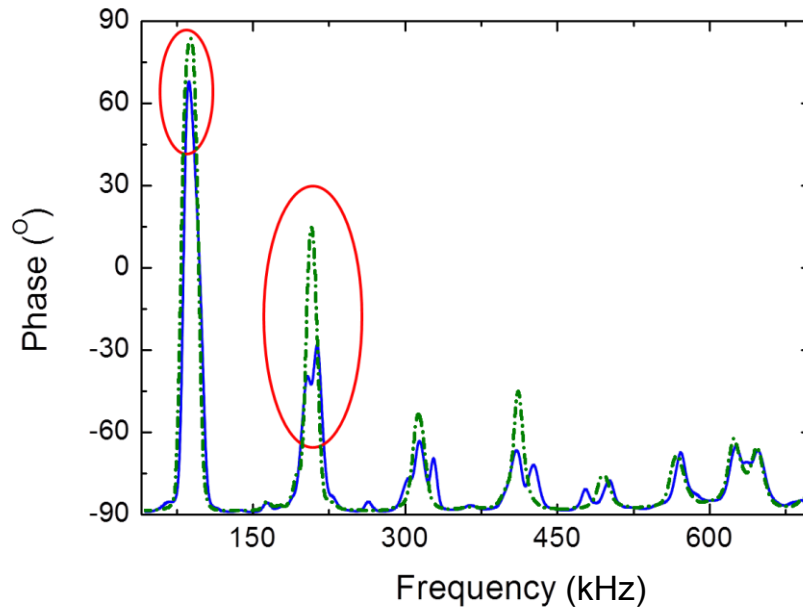
Figure 3.11 - Electrical phase measurement of the PZT before (dotted lines) and after (solid line) the assembling in the holders.
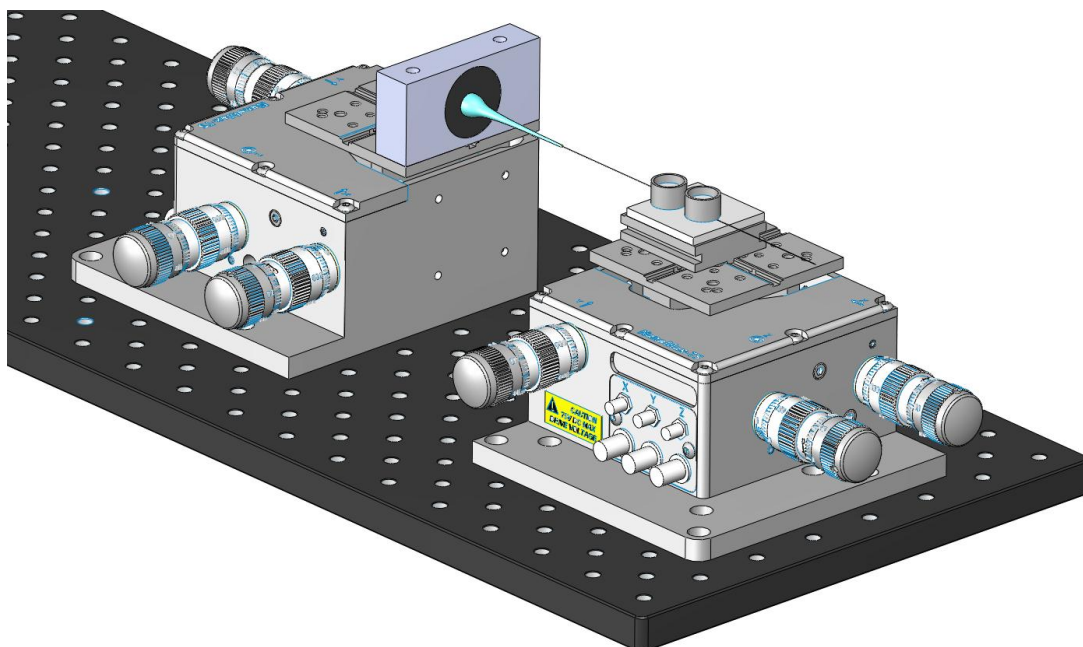
Figure 3.12 - The set PZT-silica horn-fiber assembled on top of translational stages.

3.2.1.4 The acousto-optic modulator

The acousto-optic modulator consists of the fixing stages connected to an arbitrary RF signal generator for excitation of the PZT disc, an optical source for the interrogation of the grating, a polarization controller, an optical spectrum analyzer (OSA) and/or a photodetector for measuring the grating parameters, as shown in figure 3.13. The applications proposed in this work are based on this setup.
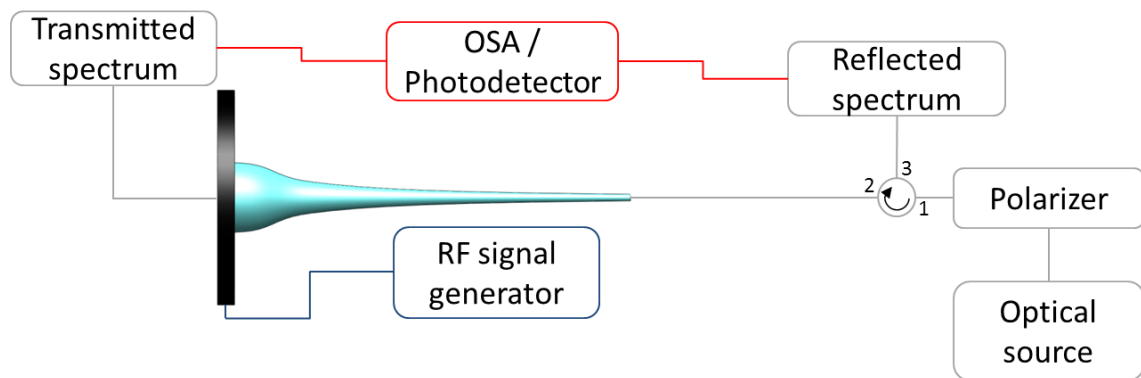
Figure 3.13 - Experimental assembly of the acousto-optic modulator.

4   CHARACTERIZATION OF THE MODULATOR

As different mechanical modes can be excited using the silica horn – fiber set, the modulator has to be characterized in order to give information about the way it affects the grating spectrum. A 3-D simulation based on finite elements method was performed in order to show the mechanical modes excited in the fiber.

4.1   RESONANCE MODES OF THE SILICA HORN – FIBER SET

Using the commercial software ANSYS$^{®}$, simulations demonstrated that different modes can be excited in the fiber, depending on the frequency applied to the PZT, considering the longitudinal excitation of the base of the silica horn. A modal analysis was first performed and showed that flexural modes are predominant in the low frequency regime, due to the buckling load that acts in the fiber, generating bends. The resultant flexural acoustic wavelength can be calculated using the equation

$$\lambda_s = \sqrt{\frac{\pi a c_{ext}}{f}} \tag{4.1}$$

where a is the fiber radius, c_{ext} is the extensional acoustic velocity in the material and f is the acoustic frequency applied on the base of the silica horn (see figure 4.2), whose value fits well with the mechanical simulation. For example, considering a longitudinal frequency $f = 38,508$ kHz on the basis of the silica horn which corresponds to the 49th resonance mode of the silica horn – fiber set, the calculated acoustic wavelength is $\lambda_s = 5,2$ mm, which is comparable to the result obtained in the simulation, as shown in figure 4.1.
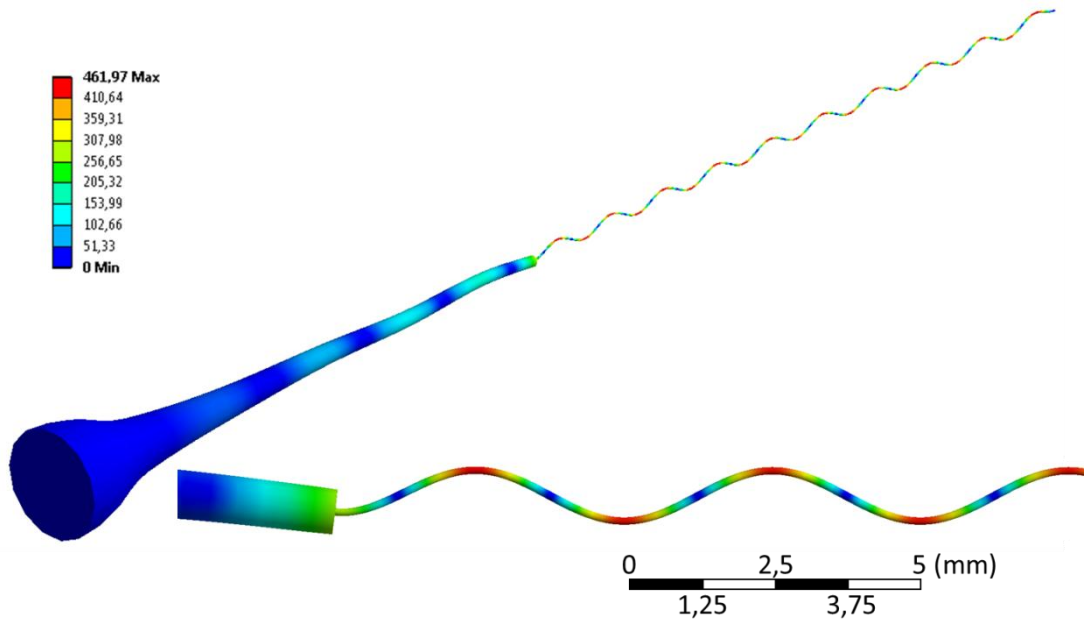
Figure 4.1 - Flexural vibration of the 49th vibration mode in the fiber at f = 38,508 kHz.

To perform the simulation, 24.323 finite elements containing 51.818 nodes were used as shown in figure 4.2. The boundary conditions were chosen as follows:

- Fixed supports were added to the base and the fiber end;
- The movement of the silica horn base was restricted only to the longitudinal axis.

The first 1.000 modes were calculated using the modal analysis without pre-tension on the fiber. However, as the PZT supports frequencies up to ~1,2 MHz (see figure 3.5), only the first 450 modes were considered. A variety of mode shapes were observed, considering the proposed dimensions of the modulator. Examples of mode shapes are shown in figure 4.3. Such modes are classified as flexural (presence of bends), longitudinal (absence of bends) or radial (radial expansion), whose frequencies are also listed in table 4.1. The classification is done simply by observation of the resulting excitation.

Table 4.1 - Mode and correspondent frequency and shape.

Mode	Frequency (kHz)	Mode shape
11	3,012	Flexural
43	31,133	Radial
51	41,692	Flexural
57	50,305	Longitudinal
86	99,290	Longitudinal
112	154,730	Longitudinal
113	155,690	Radial
117	161,350	Flexural
192	373,650	Radial
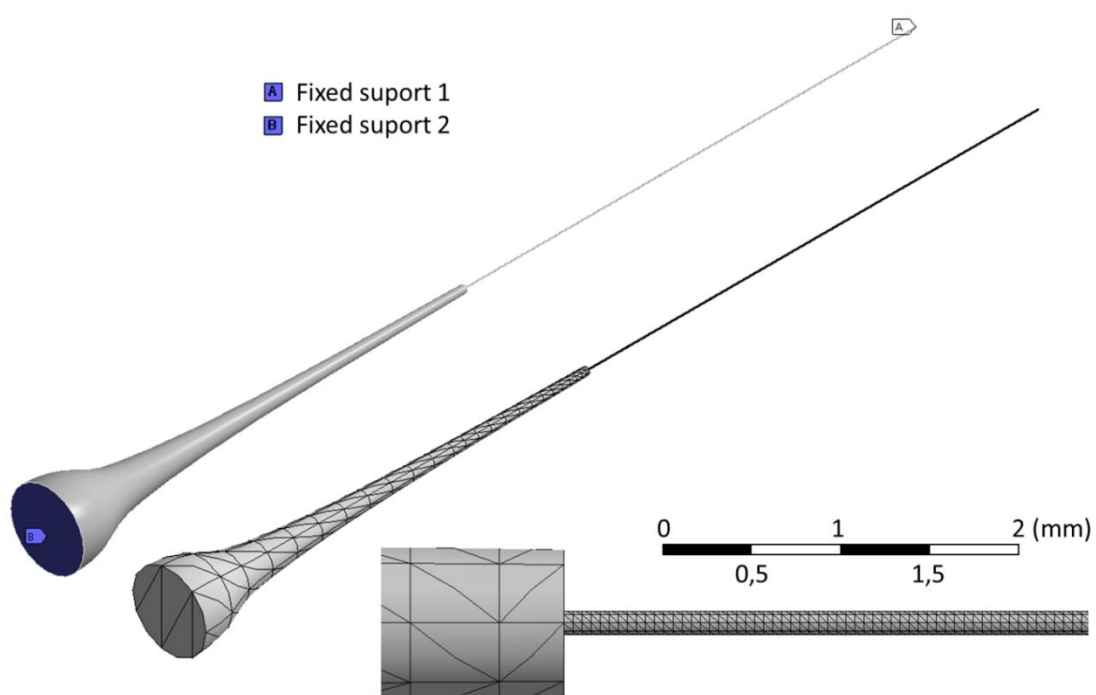
Figure 4.2 - Finite elements used on the mechanical simulations.
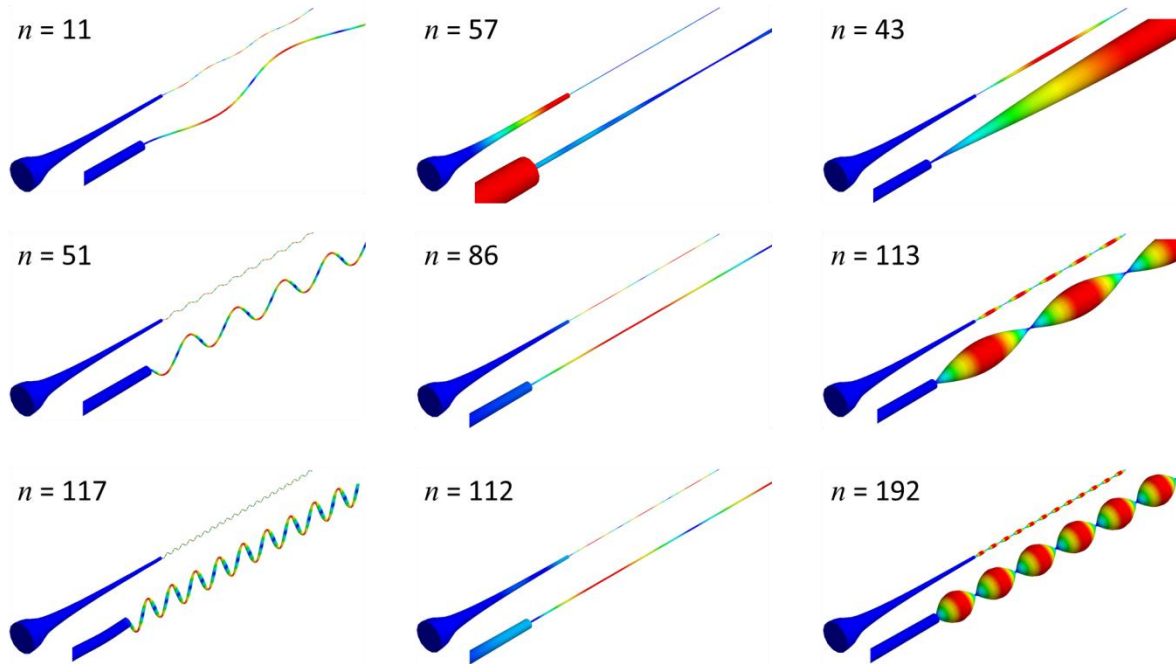
Figure 4.3 - Different mode shapes observed in the excited fiber: flexural, longitudinal and radial. The term *n* represents the mode number.

In order to characterize the modulator cell, the frequency applied to the PZT was swept from $f = 0$ to 1,2 MHz. Spectral changes on the gratings were observed using an optical spectrum analyzer. However, even though the characterization of the PZT and the silica horn - fiber set were presented alone, the frequencies where the effects on the gratings were observed are a combination of the resonance of the PZT and the set, thus, different values than the presented were achieved.

4.2   THE FLEXURAL VIBRATION OF THE FIBER

4.2.1   Fiber Bragg grating – The reflectivity modulation

When the fiber containing the grating is excited by flexural waves, the effects described in section 2.2.1.2 are achieved. Using FBGs, the main effect is the decrease of the grating reflectivity due to changes in the optical path and coupling of light to higher order modes. This decrease is observed both on reflection and transmission spectra.

Figure 4.4 shows the reflectivity and transmissivity behavior of a FBG, when excited with a flexural wave at $f = 54$ kHz. When the PZT load is varied from $V_{PZT} = 0$ to 10 V, the reflectivity decays 60%, following a non-linear behavior, and the transmissivity increases 18 dB. More evident results are achieved by enhancing the PZT load.
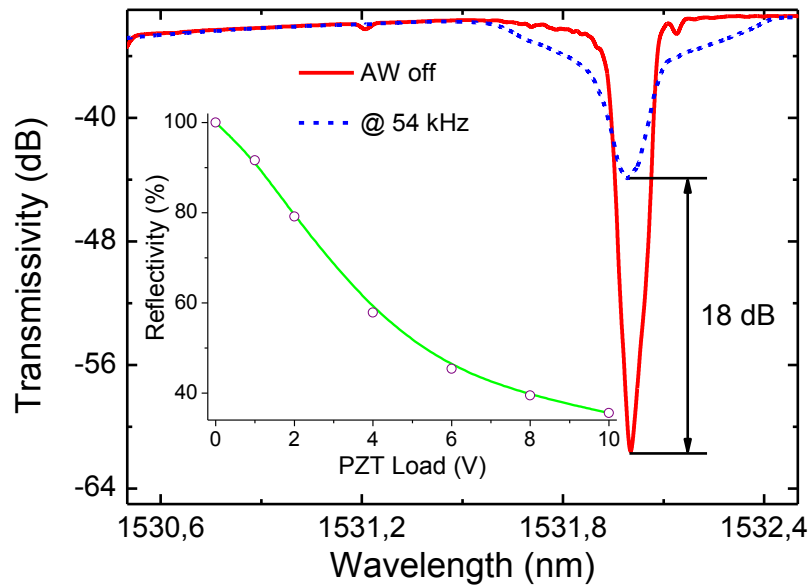
Figure 4.4 - Reflectivity and transmissivity behavior of a FBG. Inset: The reflectivity behavior depending on the PZT load.

Figure 4.5 shows the spectrum behavior of the FBG when a flexural wave excites the fiber at $f = 115$ kHz. In this case, the reflectivity decay (7 dB) of the grating does not present the same attenuation observed in the example of figure 4.4, where the transmission enhancement is 18 dB. It means that the flexural acousto-optic effect is changing the reflectivity by changing the optical path and effective refractive index and the transmissivity by coupling light into cladding and radiation modes.
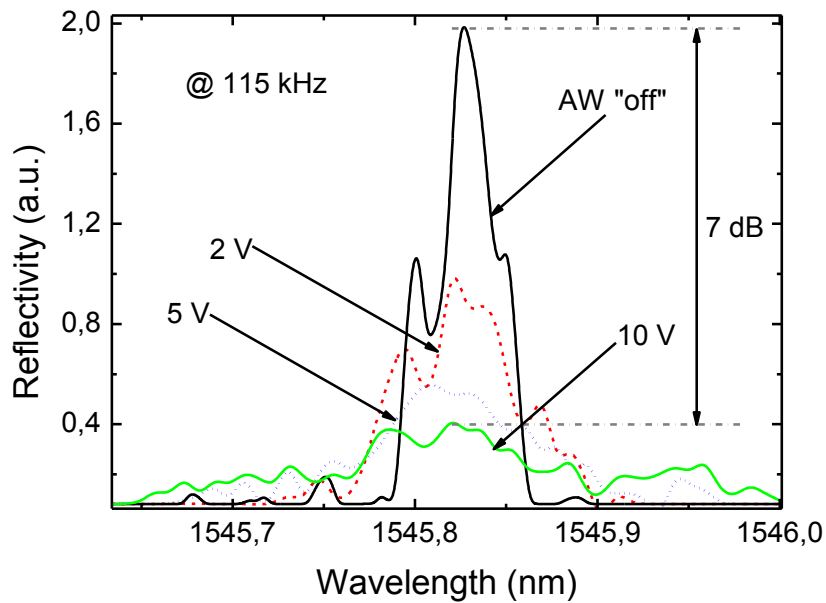
Figure 4.5 - Reflection spectrum of a FBG when excited by flexural acoustic waves at *f* = 115 kHz.

4.2.2 Long period grating

Using LPGs, the effect of bends on the spectrum is more evident when resonance frequencies are chosen. The periodic bend induced by the acoustic wave changes the optical path, modifies the difference between the effective refractive indices of the core and cladding modes and modulates the intermodal overlap integral, consequently reducing the coupling coefficient between them. Figure 4.6 shows the behavior of the LPG spectrum when the acoustic frequency is swept from *f* = 52 to 74 kHz. Particularly, the more evident effects in the LPG spectrum appears at *f* = 53,3 kHz and *f* = 60,6 kHz (two first peaks of figure 3.5(*b*)). Figure 4.7 shows the minimum transmissivity and dip wavelength behavior of the LPG spectrum (projection of figure 4.6) depending on the excited frequency. It can be used in order to identify the resonance frequencies of the set.
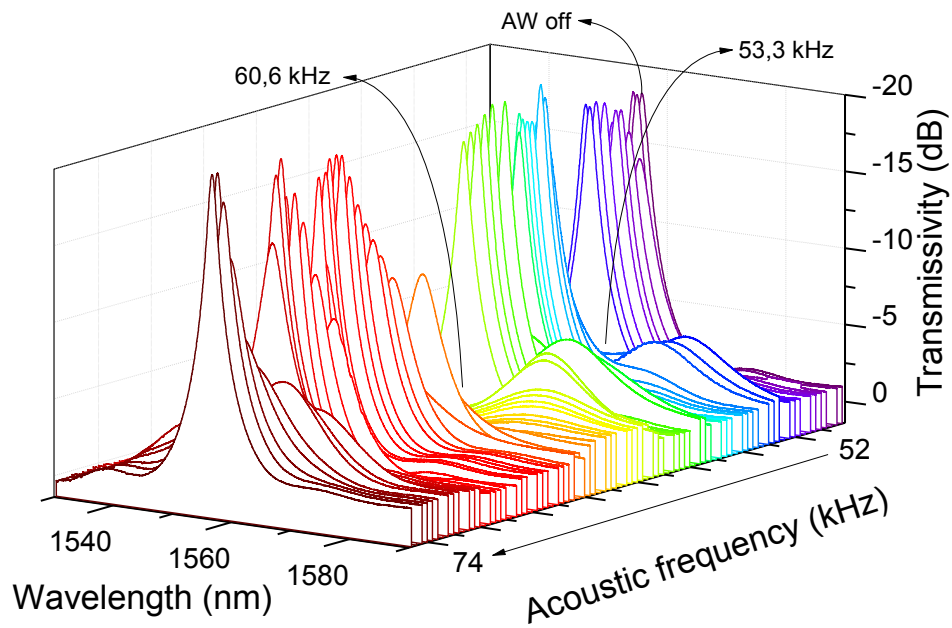
Figure 4.6 - LPG spectrum behavior when the excitation frequency is swept from *f* = 52 to 74 kHz, considering a PZT load at *V_PZT* = 10 V (note that the *y*-axis (transmissivity) is upside down).
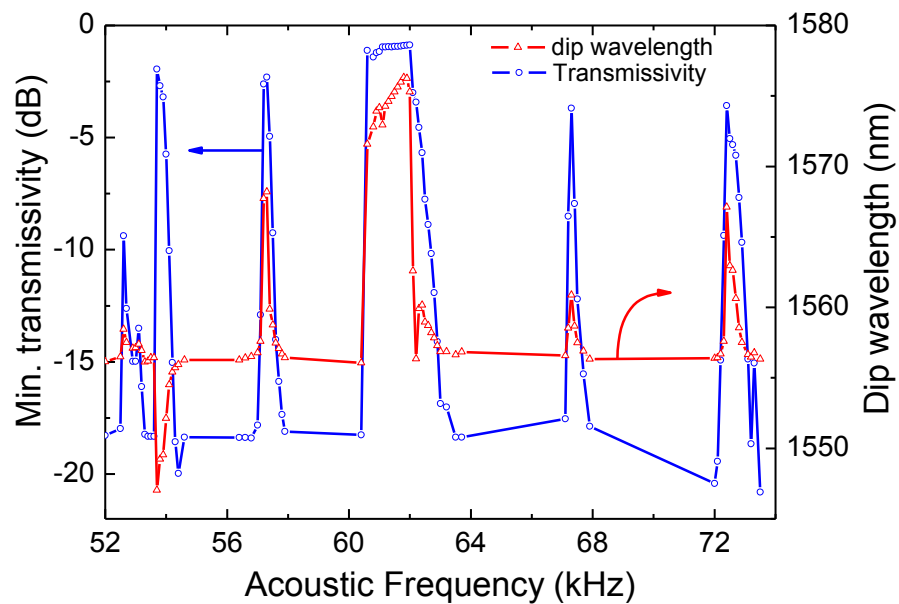
Figure 4.7 - Resonance spectrum of the modulator, measured by means of acousto-optic effect in LPG.

Figure 4.8 shows the result of the modulation for an acoustic excitation at $f = 60,6$ kHz. The PZT load was varied from $V_{PZT} = 0$ to 10 V. The increase in amplitude of the acoustic wave reduces the peak transmissivity of the LPG attenuation band and induces a shift to longer wavelengths (red shift). A similar behavior is observed for acoustic waves generated

at other resonances, however, the magnitude of the effect is lower than that achieved at $f =$ 60,6 and 53,3 kHz, which are the strongest observed with the silica horn − fiber set used in the experiments.
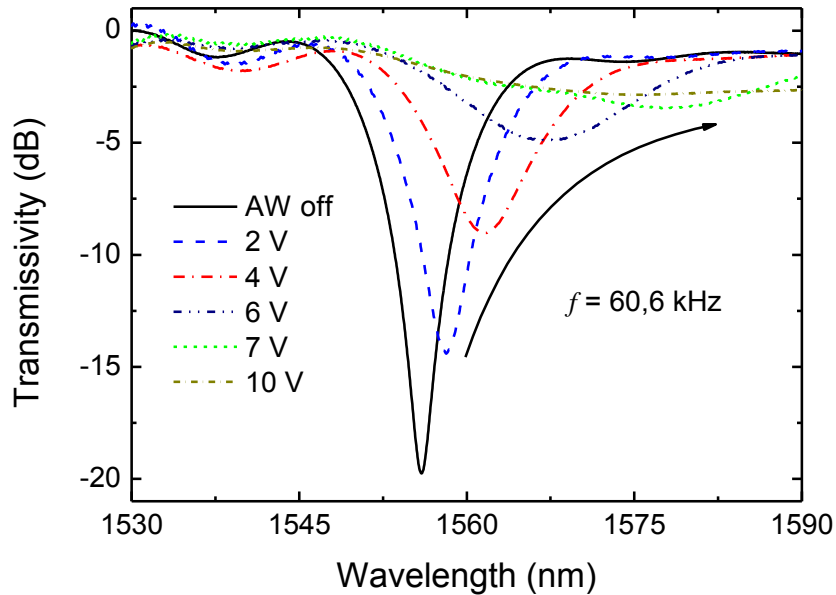
Figure 4.8 - LPG spectrum behavior when the PZT load varies from 0 to 10 V at f = 60,6 kHz.

Simulations were performed using the numerical approach presented in section 3.1, through the combination of the transfer matrix and assumed modes methods. Figure 4.9 shows the experimental and simulated (using TMM) transmission spectrum of the LPG when no acoustic wave is applied to the fiber (fiber at rest). The TM method provides an excellent match of the wavelength dip for the transmission band, but delivers a slightly different behavior concerning the device bandwidth.
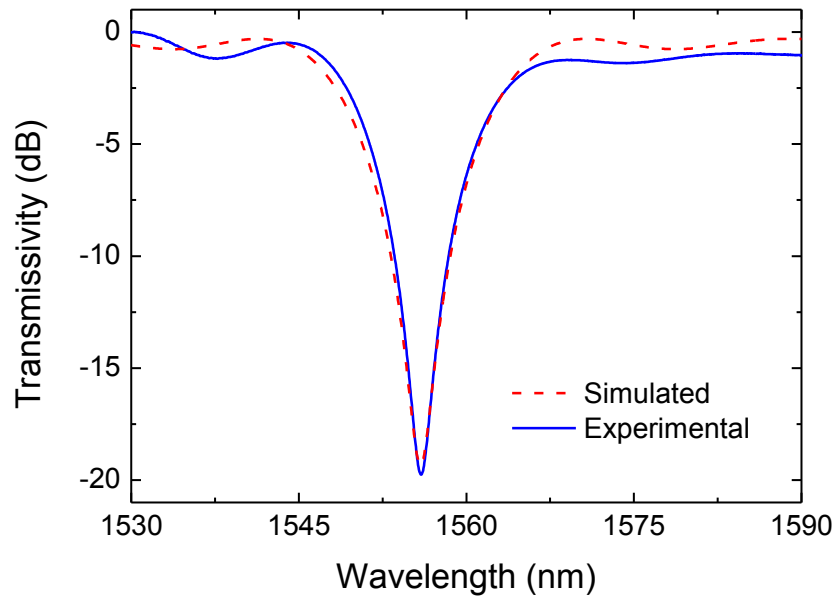
Figure 4.9 - Simulated and experimental spectrum of the LPG.

Figure 4.10 shows the minimum transmissivity of the LPG over the load range from $V_{PZT} = 0$ to 10 V, also related with the force applied to the horn base, at the excitation frequency of $f = 60,6$ kHz. At $V_{PZT} = 10$ V the force delivered by the PZT corresponds to $P_0 = 0,042$ N (verified by comparison with numerical results). Over the PZT load range, ~ 15 dB decrease of the attenuation peak is achieved, however, this relationship, between the amplitude of acoustic wave and the wavelength shift, is quasi-linear up to $V_{PZT} = 6$ V, and then it levels up and keeps stationary. Figure 4.11 shows the shift of the dip wavelength ($\Delta\lambda = 31,6$ nm) over the same voltage range. At $V_{PZT} = 6$ V there is a transition region, where the main peak is completely suppressed and secondary peaks appear in the spectrum. In this case, the initial conditions of the overlap integral is changed, presenting two distinct solution, so generating two attenuation bands in the transmission spectrum.
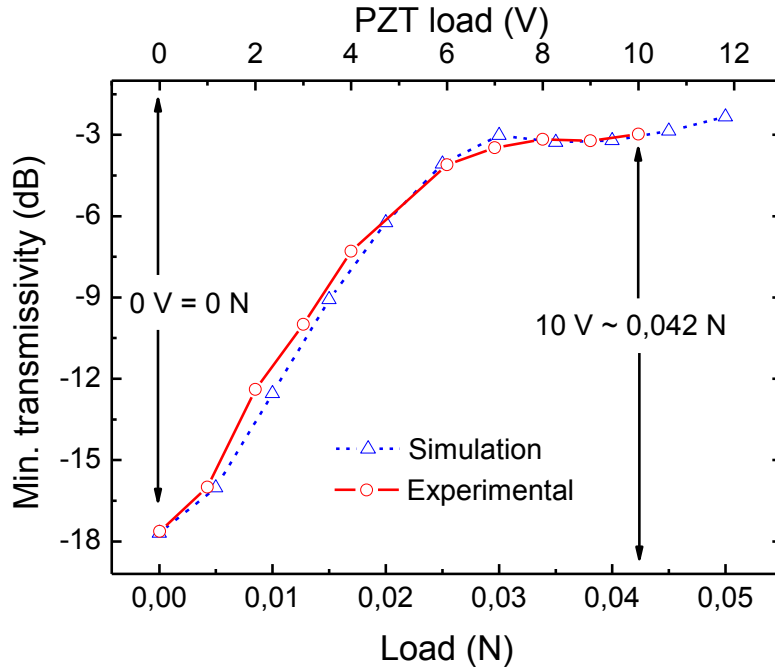
Figure 4.10 - Experimental and simulation results for the behavior of the minimum transmissivity at the peak wavelength versus the PZT load and the force.
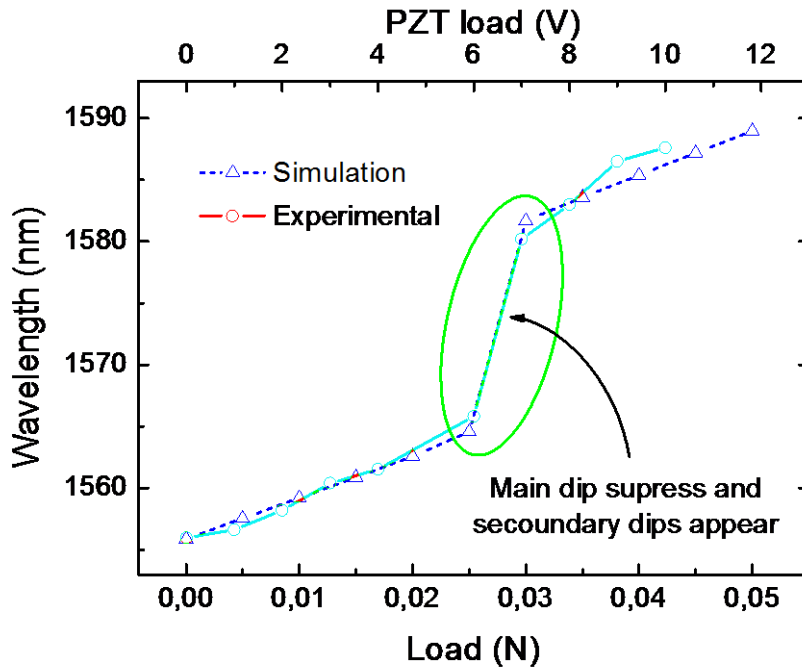
Figure 4.11 - Experimental and simulation results for the behavior of peak wavelength when the acoustic wave at f = 60,6 kHz excites the grating.

The secondary peaks are more evident at the acoustic excitation f = 53,3 kHz, as shown in figure 4.12. At this frequency for V_{PZT} = 10 V, the formation of two attenuation peaks (blue and red peaks) can be clearly seen, which are separated $\Delta\lambda$ = 34,2 nm apart.

Besides the change in the optical path, changes in the difference between the effective refractive indices of core and cladding modes, as well as the break of degeneracy of the circular cladding modes, lead to the modification of the LPG spectrum (BLOCK *et al*, 2006; ALLSOP *et al*, 2004). Furthermore, experiments showed that no significant polarization dependence exists (BLOCK *et al*, 2006; CHEN *et al*, 1999). The experimental behavior is verified by the simulation (considering $F = 0,06$ N due now to a different mechanical resonance), whose result fits well the experimental curve, particularly at the long wavelengths (red peak). A total shift of $\Delta\lambda = 20,6$ nm is achieved by driving the PZT from $V_{PZT} = 0$ to 10 V in relation to the peak at rest (no acoustic wave).
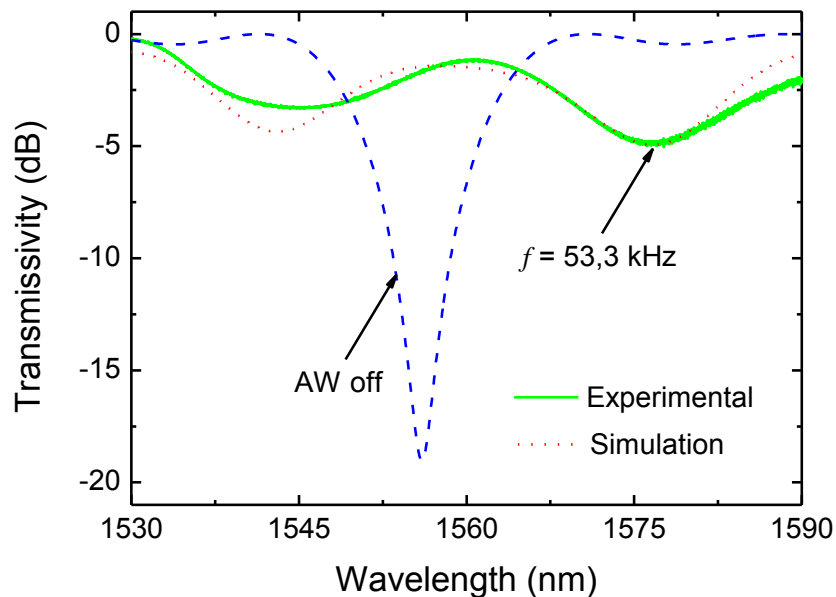
Figure 4.12 - LPG spectrum behavior for PZT load at $V_{PZT} = 10$ V ($P_0 = 0,06$ N) at $f = 53,3$ kHz.

During the experiments, it was noticed that for higher frequencies (in the $f \sim 1$ MHz range), where the predominant vibration mode is longitudinal (OLIVEIRA *et al*, 2010a) no such effect takes place in the LPG spectrum. The explanation for this absence of grating modulation is that the induced changes in the refractive indices are negligible and the longitudinal displacement of the grating planes does not affect the LPG spectrum. However, at this point, it is interesting to compare with the FBG case, for which the period is much smaller. In FBGs small changes in the grating modulation planes do change the spectrum, resulting is the modulation of the grating at higher frequencies (OLIVEIRA *et al*, 2008a; OLIVEIRA *et al*, 2010a).

4.3   THE LONGITUDINAL VIBRATION OF THE FIBER

In the high frequency regime (frequencies higher than $f \sim 500$ kHz) the predominant vibration modes in the fiber are longitudinal. However, even though the predominant resonant modes when low frequencies are applied are flexural, particular frequencies can generate longitudinal vibration modes in the fiber as well. In fact, different resonant modes have been excited in the fiber depending on the applied frequencies. From simulation results obtained with ANSYS and from the behavior of grating spectra, one can see which mode (flexural or longitudinal) is predominant at a particular frequency.

For frequencies around 200 kHz, a flexural effect was expected in the grating spectrum, however, for some particular frequencies a side lobe generation was obtained. For example, figure 4.13 shows the reflection spectrum of the FBG when $f = 223,3$ kHz excites longitudinally the grating with PZT load at $V_{PZT} = 5$ and 10 V.
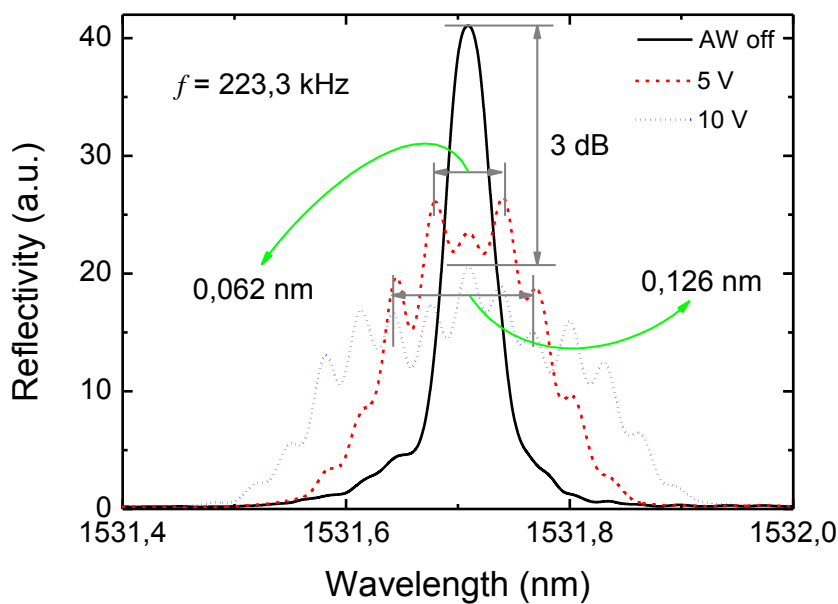
Figure 4.13 - FBG reflection spectrum of the FBG when excited by $f = 223,3$ kHz longitudinal acoustic wave.

Sweeping the frequency from 0 to $f = 1$ MHz, other longitudinal modes can be found, and the behavior of the side lobes can be tracked (considering the first and second symmetrical lobes from the center peak – called primary and secondary lobules) as shown in figure 4.14. The behavior follows the theoretical curve calculated using the numerical approach presented in section 3.1 (OLIVEIRA *et al*, 2008a). Figure 4.15 shows a comparison

of the experimental and theoretical FBG spectrum considering an acoustic excitation at $f = 1,021$ MHz with $V_{PZT} = 10$ V, which correspond to $P_0 = 1$ N applied to the base of the silica horn, considering the silica horn –fiber set presented in section 4.1. The theoretical curve fits well the experimental one in wavelength and reflectivity. As for the characterization, different experimental assemblies (silica horn, fiber tension, FBG length, holders, etc.) were used to perform the experiments and, moreover, under different physical conditions (temperature, humidity, etc.), slightly divergent results are presented along the thesis.
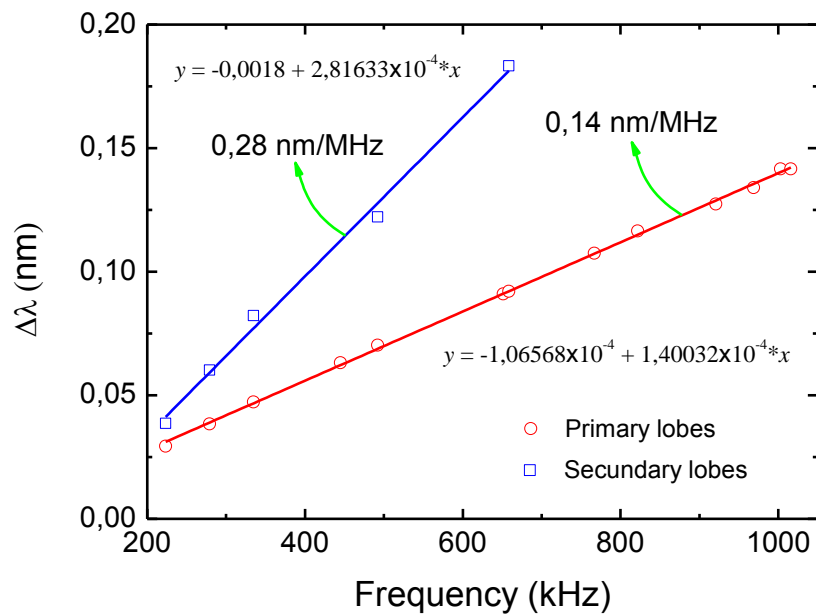
Figure 4.14 - Linear behavior of the primary and secondary lobes of the FBG spectrum, depending on the applied frequency.
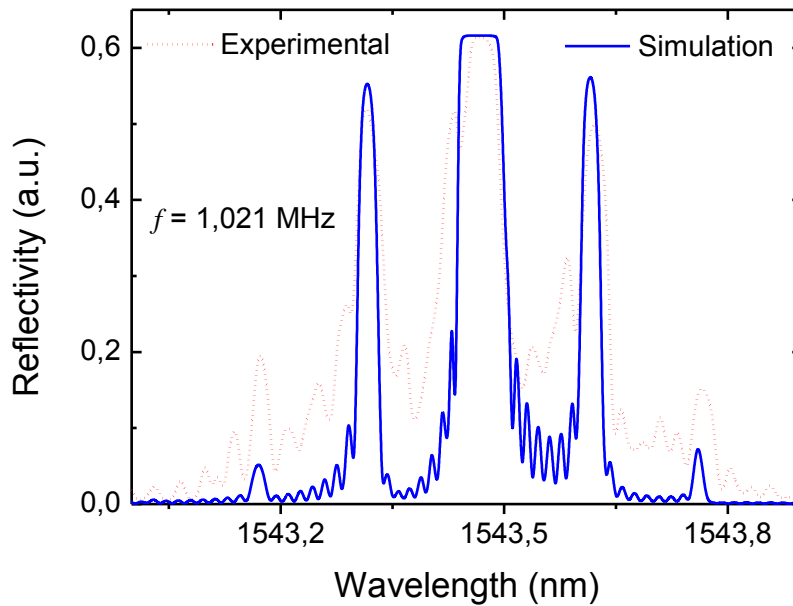
Figure 4.15 - Experimental and simulated results for f = 1,021 MHz acoustic wave excitation.

The capability of generating side lobes in the FBG spectrum opens up the possibility of having a tunable sampled grating, where the period of the side lobes is dependent on the applied acoustical frequency and the intensity of the PZT load. Figure 4.16 shows a 3-D graph that shows the behavior of the side lobes reflectivity, when the applied load varies from V_{PZT} = 1 to 10 V. This behavior is founded to be nonlinear and is characterized by an increase of the side lobes reflectivity while central wavelength peak decreases, as shown in figure 4.17.
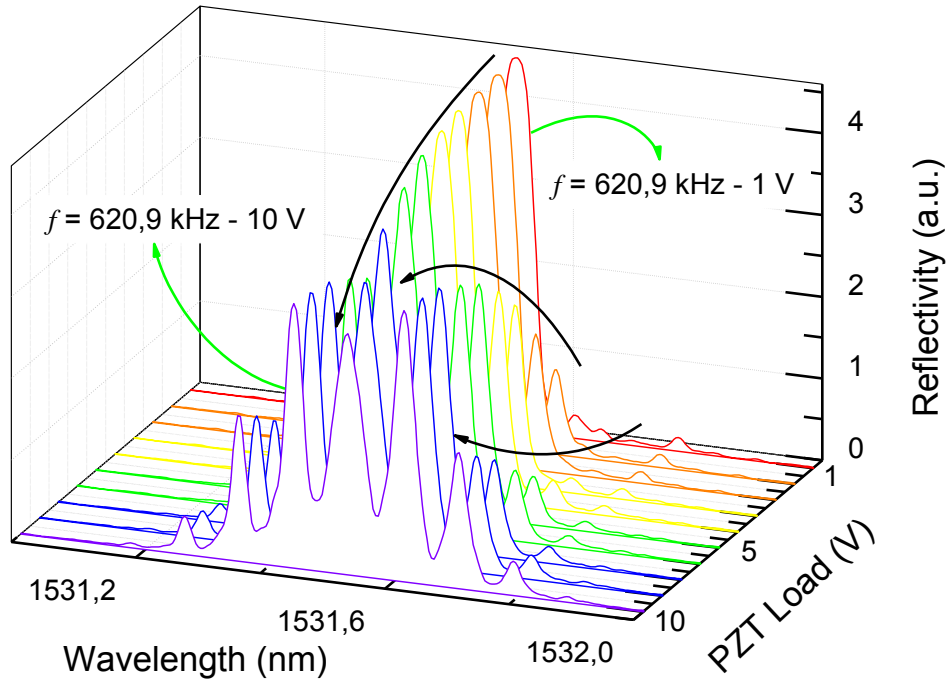
Figure 4.16 - Growing of side lobes as the PZT load increases.
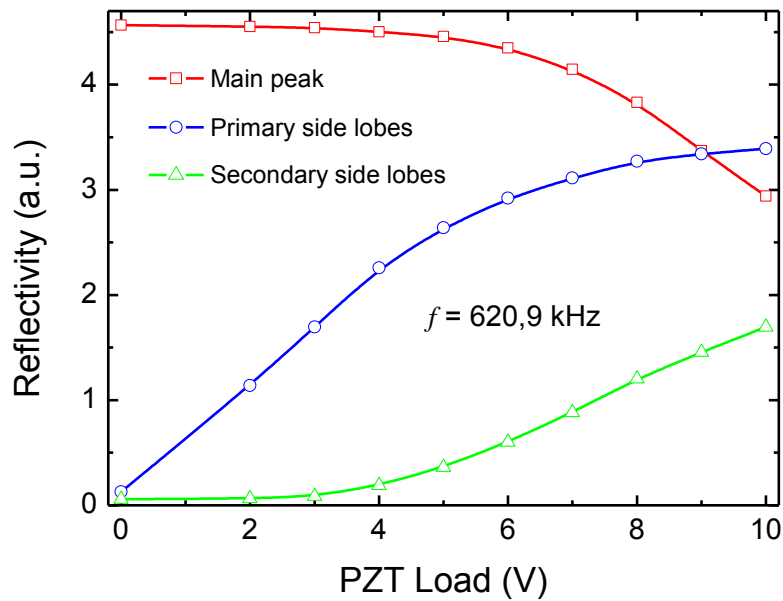
Figure 4.17 - Side lobes growing and peak wavelength decreasing behavior.

4.4   TEMPORAL CHARACTERIZATION

The time taken by the acoustic wave to change the spectrum characteristics is called switching time. This time depends on a variety of factors, such as the mechanical setup,

temperature and fiber tension. However, every assembled modulator presents a particular behavior depending on the excited frequency. For example, pure longitudinal modes usually take the time correspondent to the acoustic wave to travel at $c_{ext} = 5740$ m/s, which corresponds to the speed of sound in the silica optical fiber, calculated using the equation:

$$c_{ext} = \sqrt{\frac{E}{\rho}} = \sqrt{\frac{72,9 \text{ GPa}}{2200 \text{ kg/m}^3}} \ . \tag{4.2}$$

However, when the excited mode is flexural, the propagating time is higher, which correspond to a lower speed of sound. For a given frequency, the speed of flexural wave can be measured using the follow relation:

$$v_f = \sqrt{\pi a c_{ext} f} \ , \tag{4.3}$$

where f is the frequency applied to the PZT. Even though in these equations the external and mechanical conditions are not included, the speed of sound is strongly dependent on them. Another factor is the damping of the acoustic wave, which makes the measured time differ from the theoretical value. However, this damping characteristic can be used further to construct a sensor.

The modulator showed in figure 3.13, when operating in reflection for side lobes generation (high frequency regime), can be used to be a measure of the switching time. A photodetector is used to interrogate the reflection of an optical channel positioned on the same wavelength of a primary side lobe of a FBG, considering a longitudinal excitation at $f = 617$ kHz. When the acoustic wave is turned on, the acoustic excitation takes approximately $t_{st} = 44$ μs to change the FBG reflectivity. This time represents the period taken to allow the optical channel to be reflected by the primary side lobe and to be detected by the photodetector. Figure 4.18 shows this time, measured when the acoustic wave is "on" and taken at the point where the reflectivity response grows and remains constant. Indeed, the time that can be considered for practical applications, in this case, is $t_s = 22$ μs, which corresponds to the time the standing acoustic wave takes to be generated in the region between the tip of the horn and the fiber holder (which corresponds to the grating length). The delay observed between the RF and optical signal is related to the time the acoustic wave takes to propagate along the interaction length (silica horn + fiber) and the inertia of the system. Optimizing the experiment through the suppression of the mechanical damping that acts on the modulator, for instance, removing the device from any positioning stage (which always have a damping spring), faster switching time can be achieved. For example, by fixing the modulator in a rigid table, the time measured was $t_s = 17$ μs (MARQUES *et al*, 2011).

Using this time and taking the interaction length as $l_t = 95$ mm, the measured acoustic speed in the fiber is $c_{ext} = 5588$ m/s, which is comparable with values found in the literature (ELMORE and HEALD, 1985). This fast behavior is achieved basically due to a good coupling of the acoustic wave between the horn and the fiber, which reduces the mechanical damping. This configuration can be applied in a series of devices where fast dynamic control is required.
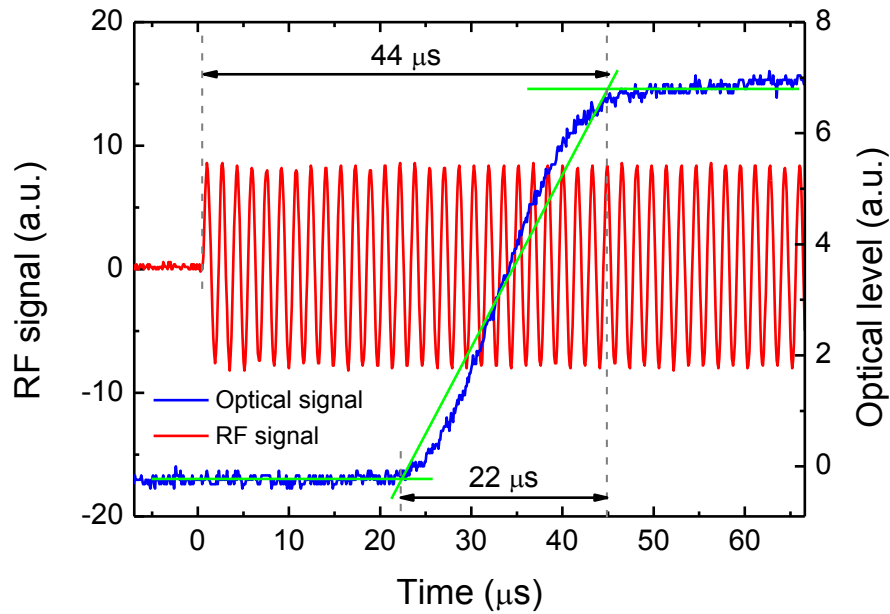
Figure 4.18 - The time response of the modulator when driven by f = 617 kHz longitudinal acoustic wave.

In the case of excitation of flexural waves, the time taken to change the spectrum characteristics is larger, as seen in figure 4.19. A tunable laser has its center wavelength tuned to the dip wavelength of a LPG and, when excited by $f = 58,8$ kHz acoustic wave, the transmission at that wavelength is enhanced, and an increase on the photodetector signal is experienced. The acoustic wave takes approximately $t_{st} = 596$ μs to change the spectrum. Furthermore, the switching time for practical applications is around $t_s = 211$ μs. The time t_{st} can be understood as the time taking to the standing acoustic wave takes place.
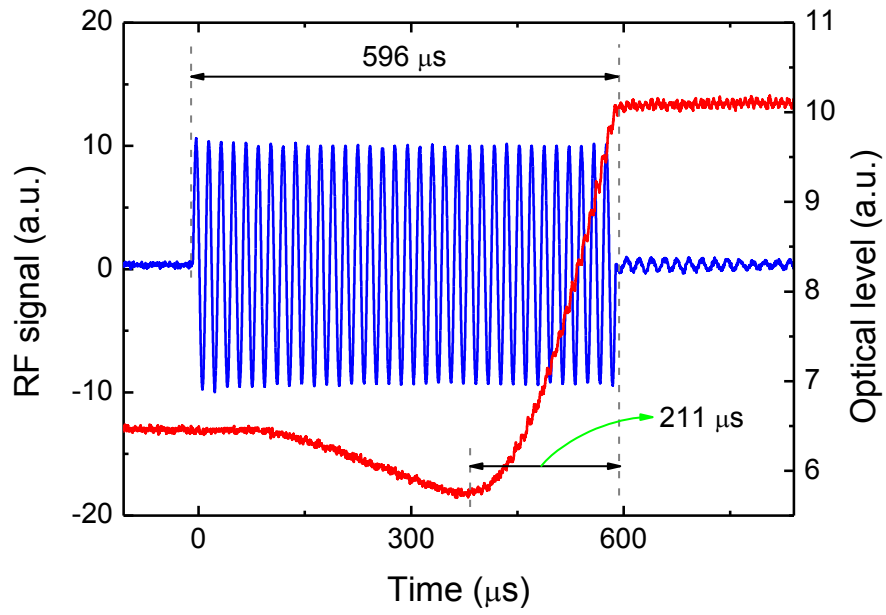
Figure 4.19 - Switching time of the modulator when driven by *f* = 58,8 kHz flexural acoustic wave.

5   APPLICATIONS

In this section, applications of the modulator are proposed and their performance verified through experiments. Such applications are based on the assembled silica-horn structure and consist of a fast add-drop (OLIVEIRA *et al*, 2009a), a tunable dispersion compensator for WDM channels (POHL *et al*, 2010; OLIVEIRA *et al*, 2010b), a new method for writing complex FBG profiles (OLIVEIRA *et al*, 2010c; 2010d; 2010e) and a compact dip-style viscosity sensor (OLIVEIRA *et al*, 2010f; 2010g). The design of these devices is presented and the main results summarized.

5.1   FAST ACOUSTO-OPTIC ADD-DROP MULTIPLEXER

5.1.1   Experimental assembly

The modulator itself works as an acousto-optic add-drop multiplexer (AO-ADM), as one can see from the schematic diagram shown in figure 5.1. The AO-ADM is based on the use of acoustical waves to decrease the FBG reflectivity (using both flexural and longitudinal modes - see figures 4.5 and 4.13), by changing the optical path and coupling coefficients. A uniform FBG ($l_g = 25$ mm) was written using the direct writing technique through the use of a phase mask and a 248 nm UV laser.
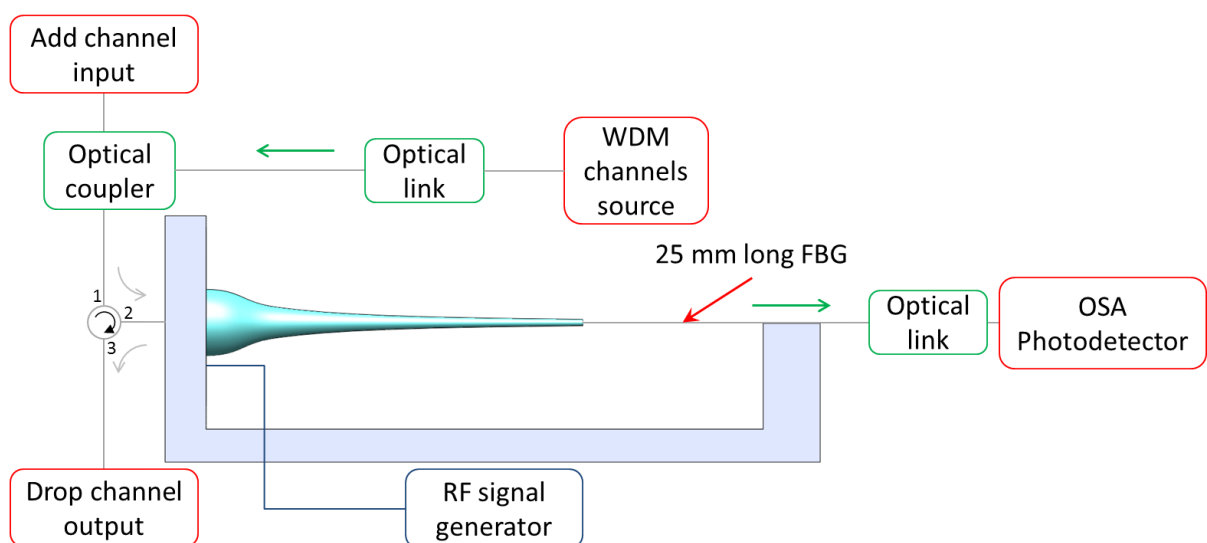
Figure 5.1 - AO-ADM schematic diagram.

For testing the device, a WDM channel source (tunable laser) to generate the optical channel, an arbitrary function generator to control the excitation of the acoustical wave and an OSA were used. A 3-port optical circulator was employed as the input and output of the AO-ADM (left hand side of the modulator in figure 5.1). The modulator is attached to port number 2. When the acoustic wave is off, the channel λ_B, inserted through port 1 and whose bandwidth is much narrower than the grating bandwidth, is reflected by the grating and exits port 3. In this configuration the grating acts as a passive element that reflects the optical channel to the output of the ADM, dropping the channel λ_B. When the acoustic wave is turned on, the resonance condition of the grating weakened and no coupling between the counter-and co-propagating modes takes place. This makes the grating reflectivity decreases allowing the addition of a channel (λ_B) in the optical link.

5.1.2   Results

The performance of the fast acousto-optic add-drop multiplexer was tested using the property of suppressing the reflectivity of the FBG through longitudinal waves (for a slower device, flexural waves can be used as well). In the "off" state the ADM works dropping the channel in port 3. In this case, figure 5.2 shows the FBG reflection spectrum and the $P_c = 0$ dBm reflected optical channel λ_B exiting port 3. On the other hand, figure 5.3 shows the transmission spectrum of the FBG and the $P_c = -20$ dBm transmitted signal. Indeed, the grating acts as a passive element that reflects the optical channel to the output of the ADM (port 3).
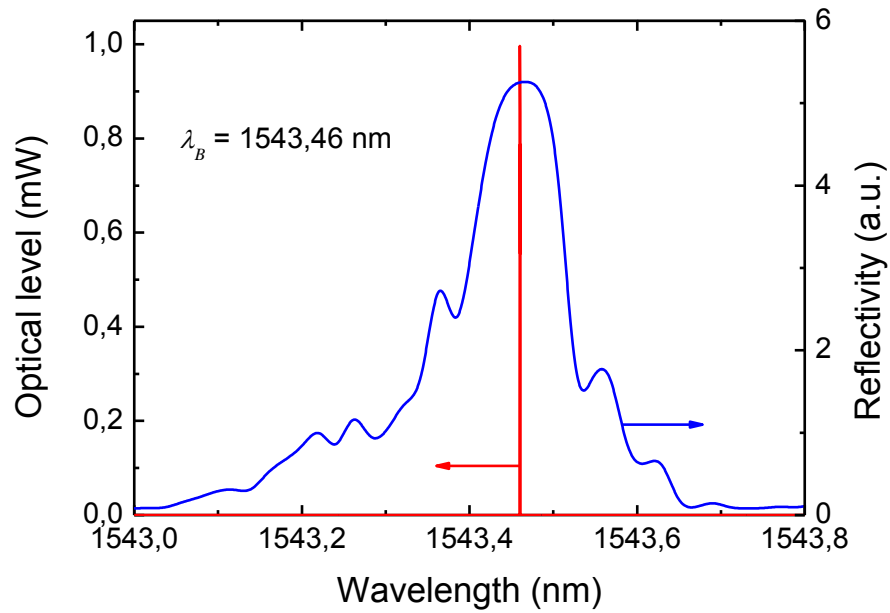
Figure 5.2 - Reflected spectrum and 0 dBm reflected optical channel (AW off).
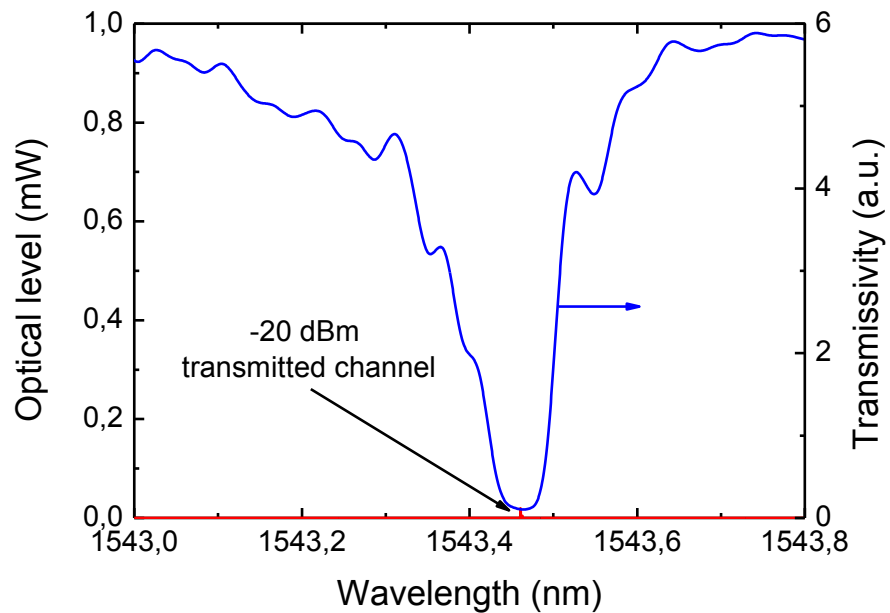
Figure 5.3 - Transmission spectrum of the FBG and the -20 dBm transmitted optical channel (AW off).

When the acoustic wave is "on" the grating spectrum is modulated and its reflectivity suppressed. When longitudinal modes are excited, the effect is the superlattice modulation of the grating, as discussed in topic 2.2.1.1. When excited by flexural waves, the optical path changes due to the flexural vibration of the fiber, and the guided fundamental mode is first

coupled to an asymmetric cladding mode, whose field overlaps weakly with the core. As most of the field is in the cladding, there is a low overlap with the grating written in the core. The condition for coupling the energy back to the fundamental mode is given by the product of the coupling coefficient between the modes and the interaction length. For this to occur, this product must be equal to π (DIEZ *et al*, 2003), a condition that can be easily controlled with the voltage applied to the PZT. Figure 5.4 shows the corresponding decrease of the FBG reflectivity together with the undesired P_c = -4 dBm channel, as the suppression of the reflectivity is not 100 %. Figure 5.5 shows the modulated transmission spectrum and the P_c = -6 dBm optical channel that passes through the grating and exits the ADM on the optical link (ADD function). The frequency used to control the reflectivity was set at f = 227,3 kHz, which allows the excitation of a longitudinal vibration mode in the fiber.
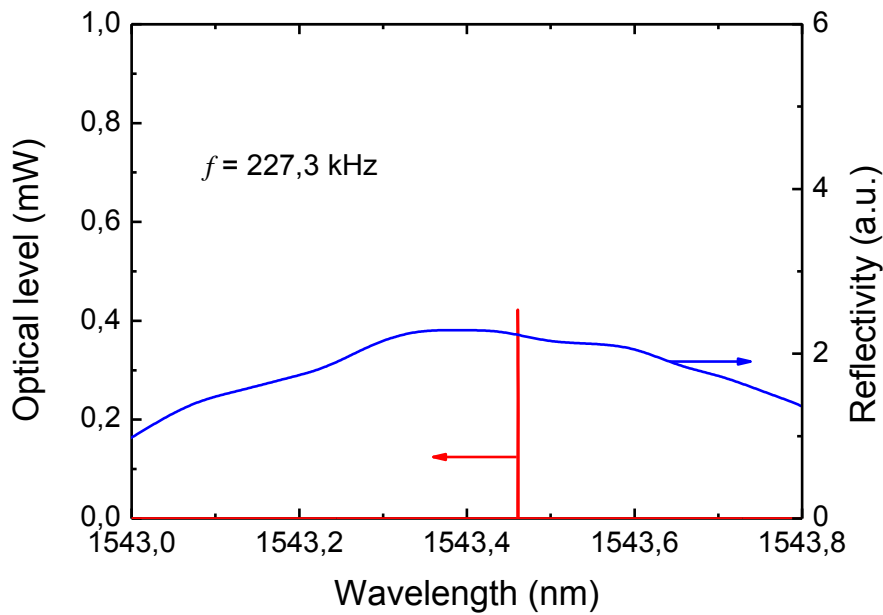
Figure 5.4 - The acousto-optic modulated reflected spectrum of the FBG and the undesired -4 dBm channel reflected by the grating and exited through the DROP port.
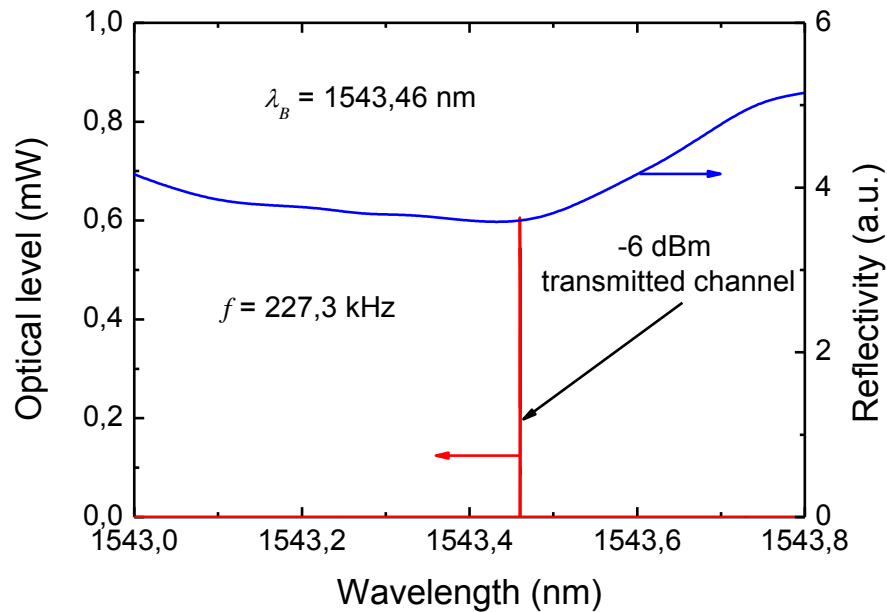
Figure 5.5 - Resultant transmission spectrum and the optical channel added to the optical link.

5.1.3 Response time

The response time was measured using a fast photodetector with the help of an EDFA to enhance the power of the optical channel. The photodetector is positioned at the transmission end of the grating. The acousto-optic effect took approximately $t_s = 61$ μs to change the FBG reflectivity, having the on-set of the RF frequency as the initial time reference, as shown in figure 5.6. This result is comparable to the fastest result achieved using this modulator (see figure 4.18 in section 4.4). The fast switching time is due to an optimal coupling of the acoustical wave between the horn and the fiber by placing both parallel to each other. The FBG reflectivity decay is strongly dependent on the PZT applied load, i.e. increasing the voltage the reflectivity is decreased from 0 to -26 dBm over 50 V, as shown in figure 5.7. The curves represent an extrapolation of experimental data, as measured points were taken for voltages up to 10 V.
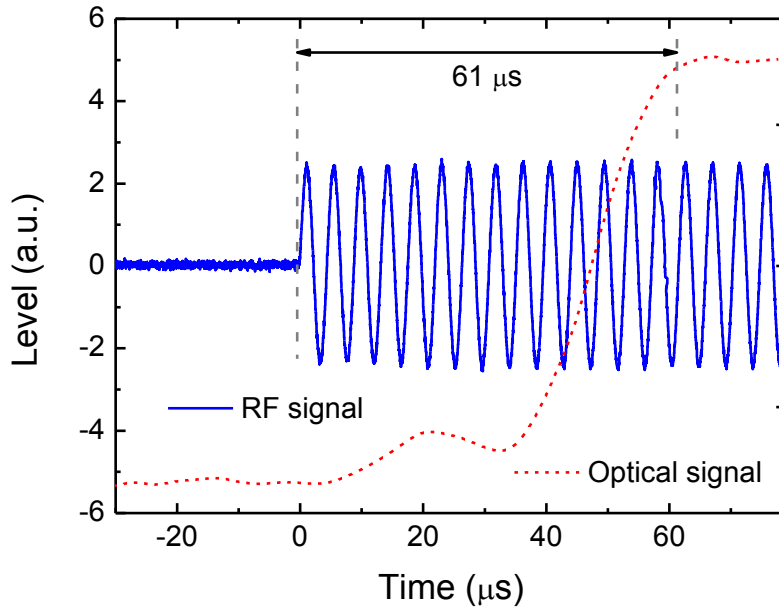
Figure 5.6 - Switching time of the ADD-DROP multiplexing.
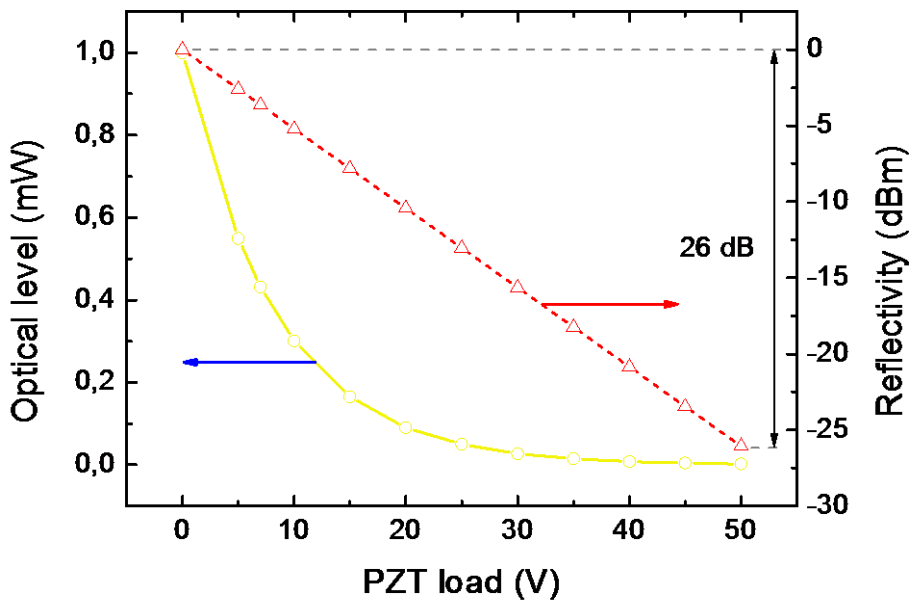
Figure 5.7 - FBG reflectivity behavior as a function of the PZT applied load.

5.2   CHROMATIC DISPERSION COMPENSATOR

Nowadays, due to the dynamics of telecommunication links, different channels travels through different optical paths, making the dispersion characteristics differ for each

case. Because of this, a dispersion compensator with reconfigurable parameters is necessary. It was noticed that, by using the acousto-optic effect, this goal can be achieved.

5.2.1 Experimental Assembly

The experimental assembly is based on the same configuration used for AO-ADM, however, instead of the OSA, an optical network analyzer (ONA) was employed. The dispersion compensation coefficient and the group delay ripple (GDR) were measured and the performance verified.

5.2.2 Results

The adjustment of frequency changes the group delay profile as well as the bandwidth, as one can see from the previous results. Figure 5.8 shows the reflection and group delay behavior when different acoustic frequencies excite the FBG (l_g = 25 cm) at f = 58, 117 and 220 kHz, respectively. The resultant group delay is measured and the dispersion coefficient is estimated. When the acoustic frequency is set at f = 58 kHz, the dispersion is measured as D = -1353,87 ps/nm, while for an acoustic excitation at f = 117 and 220 kHz, the measured dispersion is D = -287,38 and -856,50 ps/nm respectively, considering V_{PZT} = 10 V.

On the other hand, by adjusting the amplitude of the acoustic wave, changes in the group delay profile as well as the bandwidth are achieved. Figure 5.9 shows a comparison of simulated (using the FEM and TMM combination) and experimental results when no acoustic wave excites the FBG and when f = 117 kHz acoustic frequency is applied to the PZT, considering different voltages, (V_{PZT} = 5, 8 and 10 V). Results show a good agreement between simulation and experimental data. It is clear that the dispersion can be tuned by adjusting the applied PZT voltage. Moreover, the useful bandwidth, over which the slope presents a linear behavior (from V_{PZT} = 6 to 10 V) is $\Delta\lambda \sim 0,21$ nm.

Since the group delay at f = 117 kHz presents the most linear behavior (see figure 5.8) for the range between λ = 1544,25 and 1544,46 nm, this frequency was selected for more detailed analysis, as the linearity can be controlled by varying the PZT load. The dispersion can be controlled from -546,32 ps/nm (at V_{PZT} = 6V) to -132,06 ps/nm (V_{PZT} = 10V), as shown in figure 5.9. For PZT loads below V_{PZT} = 6 V, the behavior is polynomial and it is not considered for dispersion measurements (when the acoustic wave is off, the dispersion is D = -2391,49 ps/nm). In summary, figure 5.10 shows the isolated result for the dispersion

behavior when the grating is at rest and when f = 117 kHz acoustic frequency excites the fiber, considering the mentioned wavelength range.
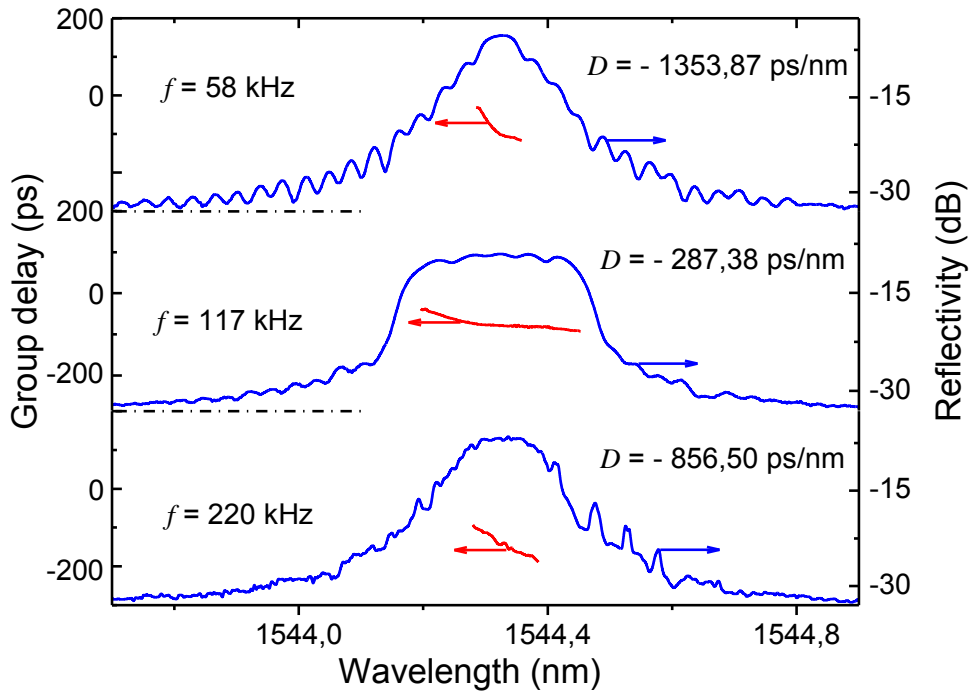
Figure 5.8 - FBG spectrum and group delay behavior when the acoustic wave is set at
f = 58, 117 and 220 kHz respectively (from the top).
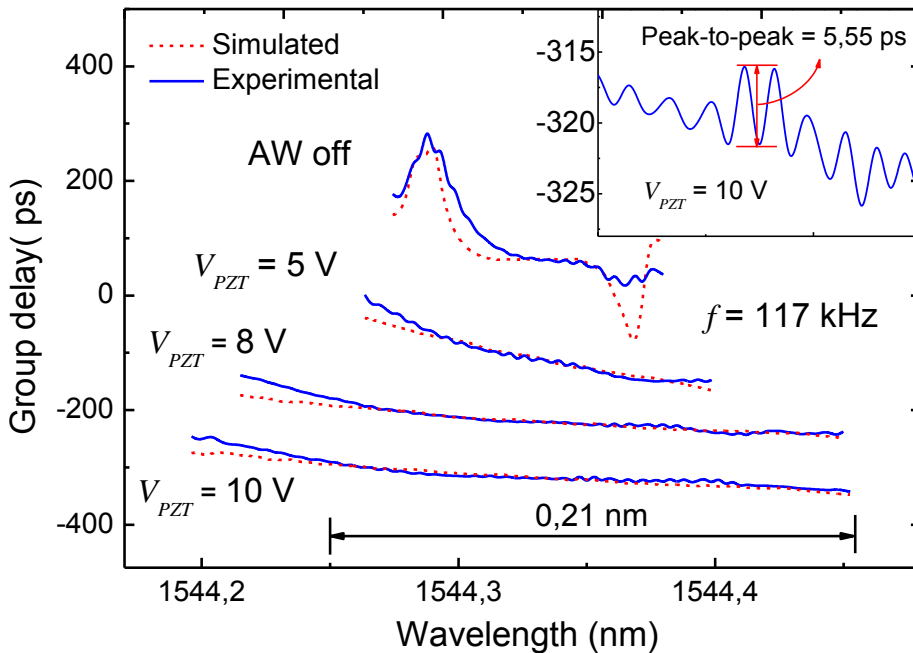
Figure 5.9 - Group delay simulation and experimental behavior when no acoustic wave excites the FBG
and when the acoustic wave is set at f = 117 kHz, driven by V_{PZT} = 5, 8 and 10 V PZT loads, respectively.
Inset: GDR spectrum when the PZT load is set at V_{PZT} = 10V.
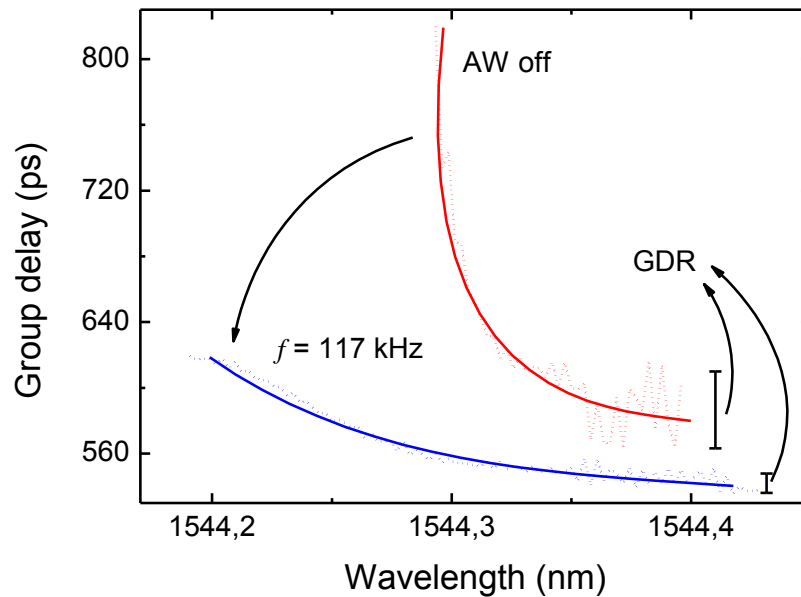
Figure 5.10 - Group delay behavior when the grating is at rest and when the acoustic wave is set on at f = 117 KHz.

The length of standard single mode fiber (SSMF) the device can compensate was estimated and shown in table 5.1. This length varies from 7 km (10 V) to 32 km (6 V), opening up the possibility to use this device in dynamic optical links, with variable length. The group delay ripple (GDR) coefficient (t_{GDR}) is caused by weak reflections occurring at the edges and along the grating and it is a critical parameter in a communication link. The GDR coefficient is measured as the peak-to-peak time variation of the group delay dispersion (in this case, the values were obtained at f = 117 kHz, for loads varying from V_{PZT} = 6 to 10 V. Results show values from t_{GDR} = ±10,06 to ±5,55 ps (table 5.1). The inset graph of figure 5.9 shows in details how the GDR is estimated (for V_{PZT} = 10 V). The acoustically induced strain wave reduces the GDR, which can be explained as a "dc" apodisation of the grating, similar to that reported for "dc" apodisation with a tailored UV writing profile (ASHTON and CANNING, 2002; ASHTON *et al*, 2004). Acceptable values for commercial applications vary from t_{GDR} = ±2 to ±10 ps, however, the average of GDR founded in datasheet of commercial equipment is t_{GDR} = ±5 ps.

Table 5.1 - Dispersion and GDR values and length of SSMF that can be compensated (length of SSMF) when the grating is acoustically excited at f = 117 kHz.

V_{PZT} (V)	D (ps/nm)	t_{GDR} (ps)	Length of SSMF (km)
AW off - 5 V	-2391,49 (nonlinear)	±37,15	--
6V	-546,32	±10,06	32,14
7V	-437,92	±7,94	25,76
8V	-320,54	±5,99	18,86
9V	-236,30	±5,71	13,90
9,5V	-180,26	±7,60	10,60
10 V	-132,06	±5,55	7,77

Figure 5.11 shows a comparison of simulated results, obtained through the combination of FEM and TMM, and experimental results for the dispersion compensation as a function of the PZT load, at f = 117 kHz. It is noticed that by adjusting the load, it is possible to dynamically control the dispersion using a low power consumption acousto-optic device.
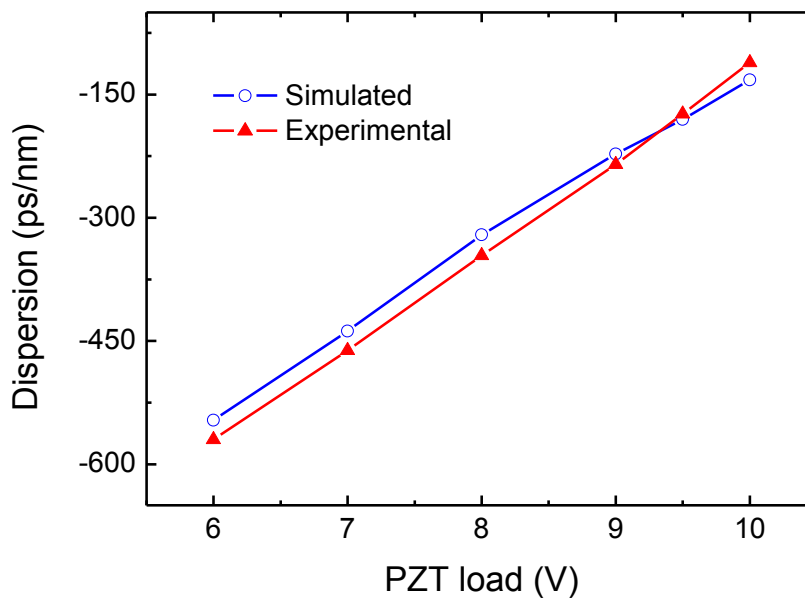
Figure 5.11 - Simulation and experimental dispersion behavior as a function of PZT load.

## 5.3	PHASE-SHIFT FBG CONTROLLER

### 5.3.1	Experimental assembly

The l_g = 50 mm long $\varphi = \pi$ phase-shifted FBG (PS-FBG) used was inscribed in standard single mode photosensitive fiber with the phase mask technique, using a 248 nm KrF laser.

The same experimental setup shown in figure 5.1 is used to characterize the phase-shifted grating. However, an ONA was used. The acoustic frequency was swept over the range from 1 kHz to 1.3 MHz in order to investigate the effects on the phase-shift.

### 5.3.2	Results

Figure 5.12 shows a comparison of simulated (using the combined FEM and TMM methods) and experimental results when an acoustic excitation at f = 621 kHz is applied to the grating creating side lobes on the phase-shifted FBG (PS-FBG) spectrum. The inset figure in figure 5.12 shows the spectrum of the PS-FBG at rest. This is an example of the excitation with a longitudinal mode. However, when a flexural acoustic mode acts on the fiber, the effect is a reduction of the reflectivity of the grating, and, consequently, the reduction of the phase-shift strength.
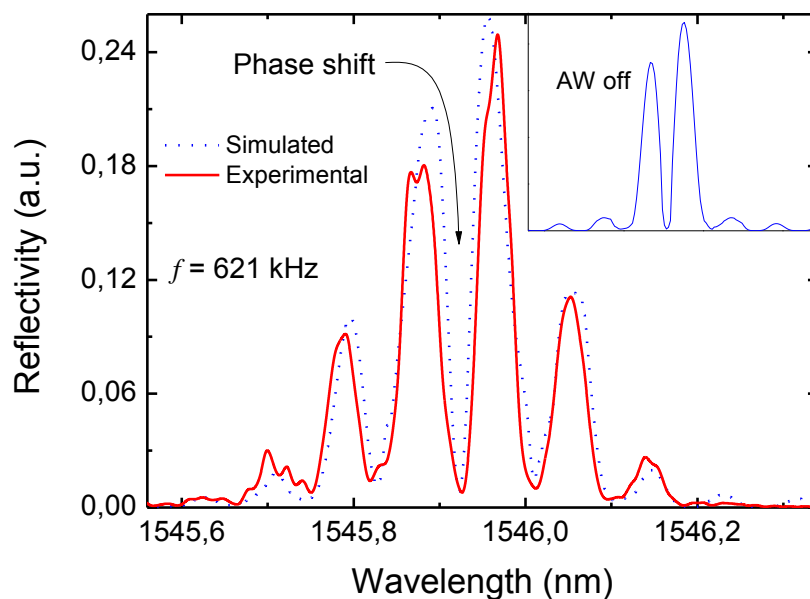
Figure 5.12 - f = 621 kHz acoustic excitation of the PS-FBG. Inset: PS-FBG spectrum when the fiber is at rest (AW off).

Figures 5.13 and 5.14 show, respectively, the reflection and transmission spectra of the PS-FBG when the PZT load varies for an acoustic excitation at $f = 113$ kHz. Figure 5.13 shows that the acoustic excitation leads to a broadening of the phase-shift, which can be controlled by changing the load. At $V_{PZT} = 5$V the notch is totally suppressed, thus values above that are not considered. Therefore, as the load is increased the notch depth decreases as shown in figure 5.13. In the same way, figure 5.14 shows transmission spectra considering the same excitation frequency. The left and right rejection bands depth decrease when the PZT load increases. The flexural acoustic wave leads to the destruction of the grating phase matching condition, turning the grating weaker. In summary, this device acts as a tunable rejection band as well as a narrow notch filter, when used in transmission and reflection, respectively.
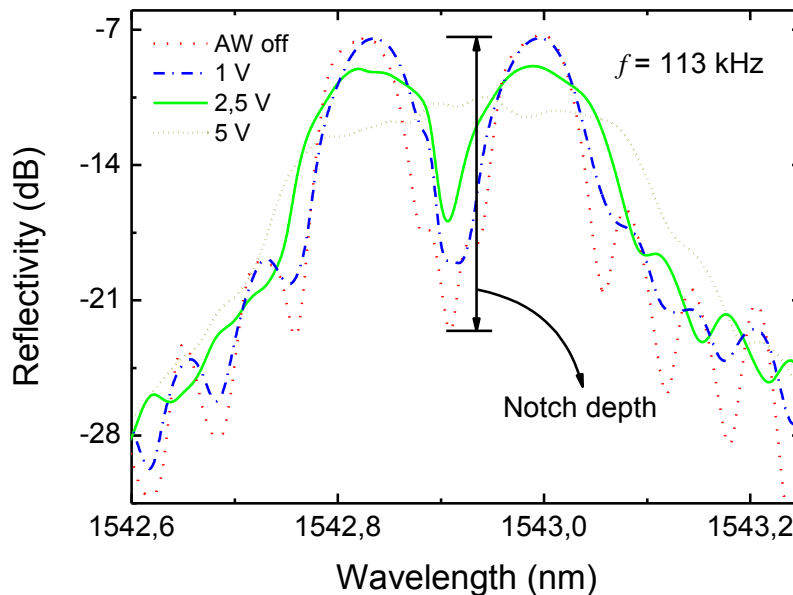
Figure 5.13 - Behavior of the PS-FBG reflection spectrum for several PZT loads at an acoustic excitation $f = 113$ kHz.

By adjusting the applied load, it is also possible to control the 3-dB bandwidth of the left and right peaks. As the load is increased the side band bandwidth increases. This particular behavior is depicted in figure 5.15. The results show that the effect is symmetrically observed on both bands.
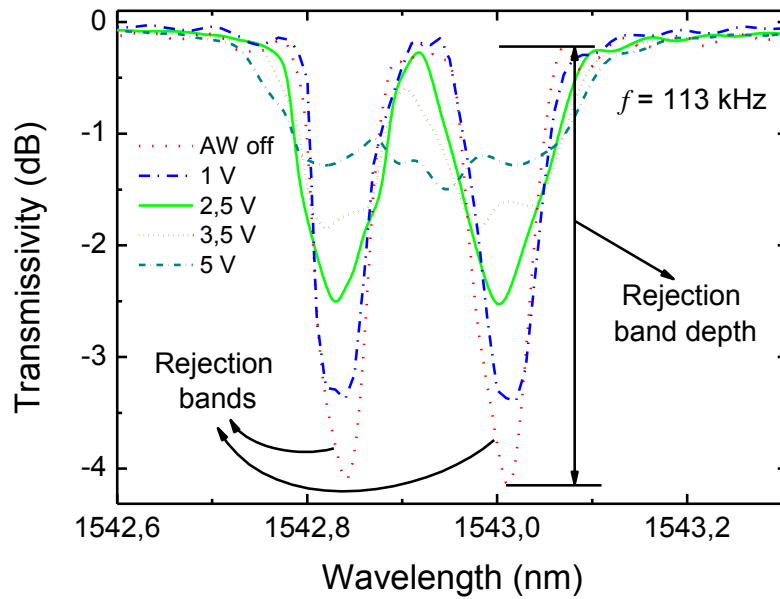
Figure 5.14 - Transmission behavior of the PS-FBG under influence of different PZT loads at f = 113 kHz acoustic (flexural) excitation.
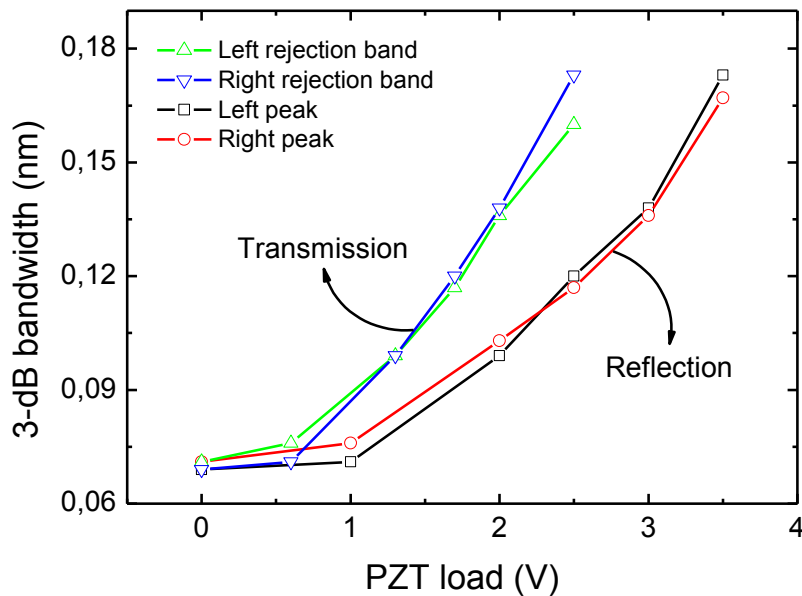
Figure 5.15 - 3-dB PS-FBG bandwidth behavior over the PZT load for the left and right transmission and reflection peaks at f = 113 kHz.

The notch depth and the rejection band depth can also be changed, as illustrated in figure 5.16. A comparison of the simulated and experimental data shows a good agreement between both. One observes that the notch depth and rejection band behavior are linearly dependent on the acoustic intensity for a particular frequency (in this case, at f = 113 kHz). By

increasing the PZT load the notch depth can be adjusted from 14 to 0 dB, while the rejection band depth varies from 3,4 to 0,3 dB. For higher loads (above V_{PZT} = 5 V), the notch is completely suppressed, leading to devices that can be implemented using very low voltage sources.
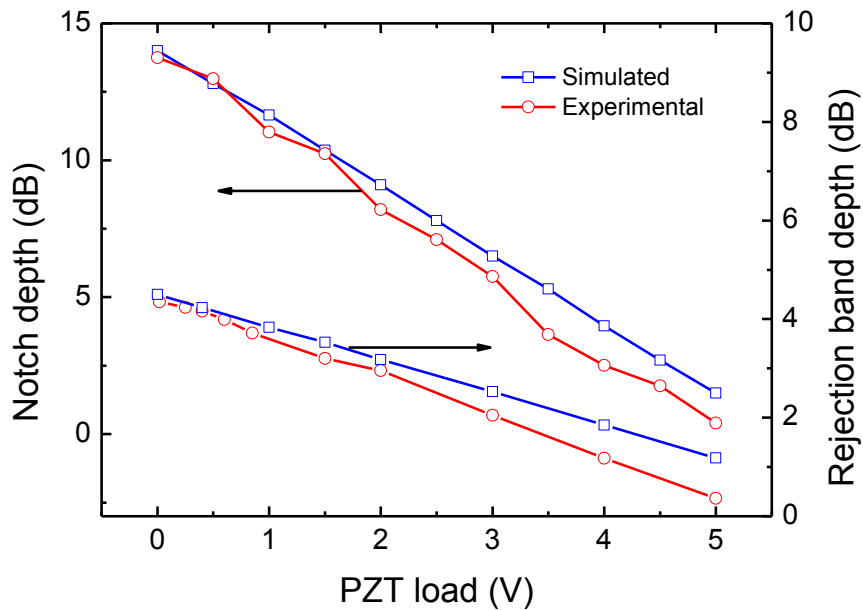
Figure 5.16 - Notch depth (reflection) and rejection band depth (transmission) simulation and experimental behavior as a function of the PZT load up to 5V (point at which the rejection band is totally suppressed).

5.4 ACOUSTO-OPTIC METHOD TO SHAPE THE GRATING SPECTRUM DURING INSCRIPTION

5.4.1 Experimental assembly

For inscription of acoustic induced gratings, the writing technique through the phase mask was modified by placing the acousto-optic modulator in positioning rigs and aligning it within the interferometer setup. Figure 5.17 shows a diagram of the setup containing the acousto-optic modulator.
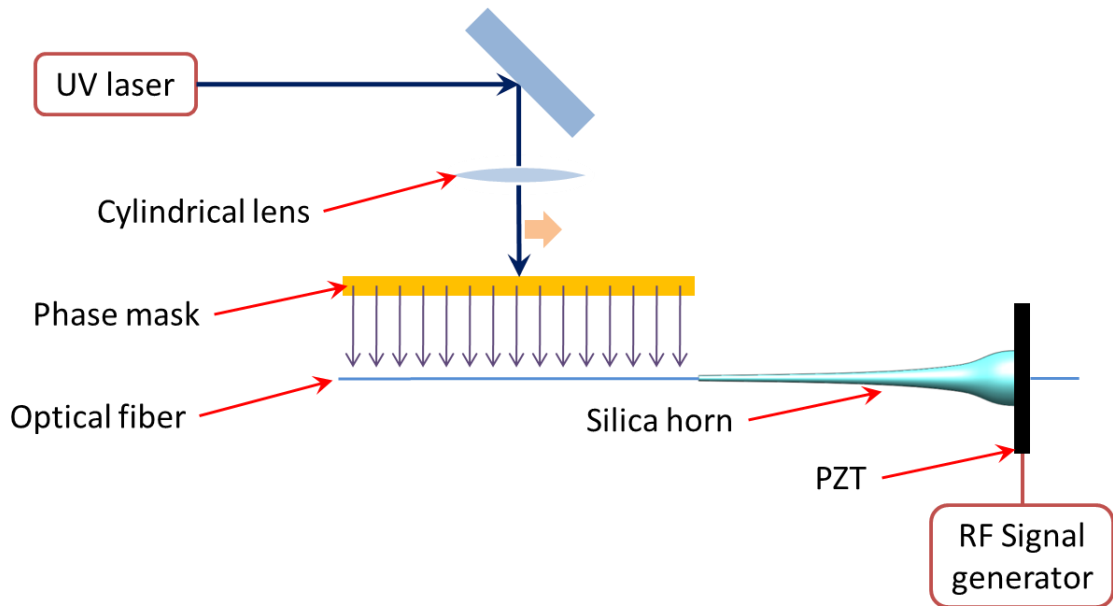
Figure 5.17 - FBG writing setup showing the modulator positioned in the assembly.

Depending on the nature of the acoustic wave (longitudinal or flexural) different properties can be adjusted. Longitudinal waves generate a periodic strain in the fiber, which gives rise to the creation of side bands in the grating spectrum (called sampled gratings (HILL *et al*, 1994; EGGLETON *et al*, 1994)), due to its non-periodic grating planes profile. The period of the generated side bands is strongly dependent on the acoustic frequency applied to the PZT, and its amplitude, on the load (PZT voltage) of the RF signal. On the other hand, flexural waves can be used to create resonant cavities, for instance, in distributed feedback lasers (DFB), due to the insertion of a phase-shift in the FBG spectrum (KRINGLEBOTN *et al*, 1994; JIANG *et al*, 2004), and in Fabry-Perot interferometers based on Bragg mirrors (WAN and TAYLOR, 2002). Flexural waves can be used to switch the grating imprinting course while the laser beam is swept over the fiber. In this case, the light from the UV source is scattered and no light reaches the core of the fiber, avoiding the necessity of using an optical switch or a beam modulator.

In summary, this new technique leads to fabrication of special gratings, known as sampled gratings, leading to profiles that form spectral combs, phase-shifted gratings and resonant cavities.

5.4.2   Results

5.4.2.1 Sampled FBG

A permanent change of the refractive index as the period of the grating is modulated under a periodic acoustic excitation during UV writing leads to sampling of the structure and the production of spectral combs. A permanently imprinted sampled grating structure, similar to those first produced by lithography in semiconductors (JAYARAMAN *et al*, 1993) and in an optical fiber as first proposed by Sceats (1994) is useful for creating complex filter devices suitable for signal multiplexing and demultiplexing or for serving as multiple narrowband transmission filters in photonic applications (HUBNER *et al*, 1998). The first sampled fiber gratings were written by sampling the period using a hair comb (HILL *et al*, 1994) and shortly after by introducing the sampling period through modulation of the UV beam over the length of the phase mask during the exposure (HILL *et al*, 1994; EGGLETON *et al*, 1994).Another method that leads to the same result uses the superposition of many gratings spectra until the summation superstructure has a similar sampling period (OTHONOS *et al*, 1994).

Figure 5.18 shows a schematic diagram that helps to explain the resultant modulated periodic index modulation of the grating planes. As one can see, the period of the sampled gratings is strongly dependent on the longitudinal acoustic wavelength (Λ_s). After the inscription, the resultant FBG modulation planes profile is not uniform, indeed, is modulated by the acoustic wave, as shown in figure 5.18.
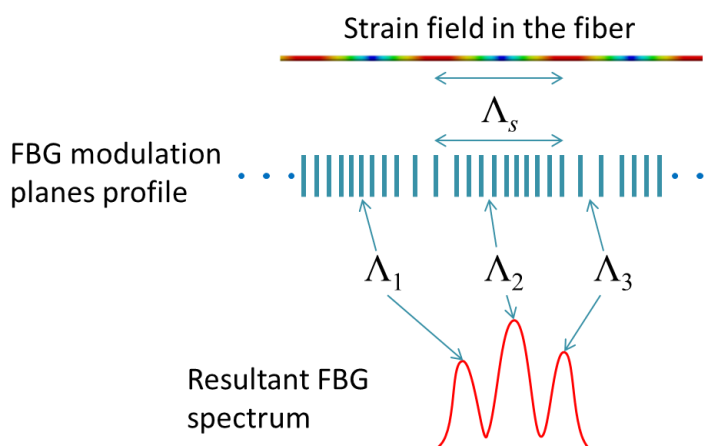
Figure 5.18 - Schematic distribution of the grating planes, which gives rise to the side bands that appear in the FBG spectrum.

Based on previous knowledge and experience, acoustic waves with frequencies at $f = 1,021$ MHz and $f = 919$ kHz were used (which correspond to two of the resonance

frequencies of the PZT). Figure 5.19 shows the resultant FBG spectrum when the acoustic wave is switched-off after the writing process at $f = 1,021$ kHz. The graph shows the formation of two side bands due to the modulation of the grating period, creating a sampled grating with 3 distinct peaks. The transmitted spectrum is also shown in figure 5.19. The separation between the generated side bands is $\Delta\lambda = 0,56$ nm, while the separation between the sampled peaks is $P = 0,28$ nm. Moreover, when the grating is excited after writing is concluded by an acoustic wave at the same frequency used during the writing process ($f = 1,021$ MHz @ $V_{PZT} = 10$ V), a sampling of the sampled grating is achieved − each sideband is now sampled to generate other symmetric side bands, one between the central wavelength and the primary bands and one after that, as shown in figure 5.20. The separation of the bands are approximately the same when the acoustic wave is applied, i.e. $P = 0,145$ nm. This behavior follows the prediction for longitudinal acousto-optic effect, showing the ratio of $P \sim 0,14$ nm/MHz.
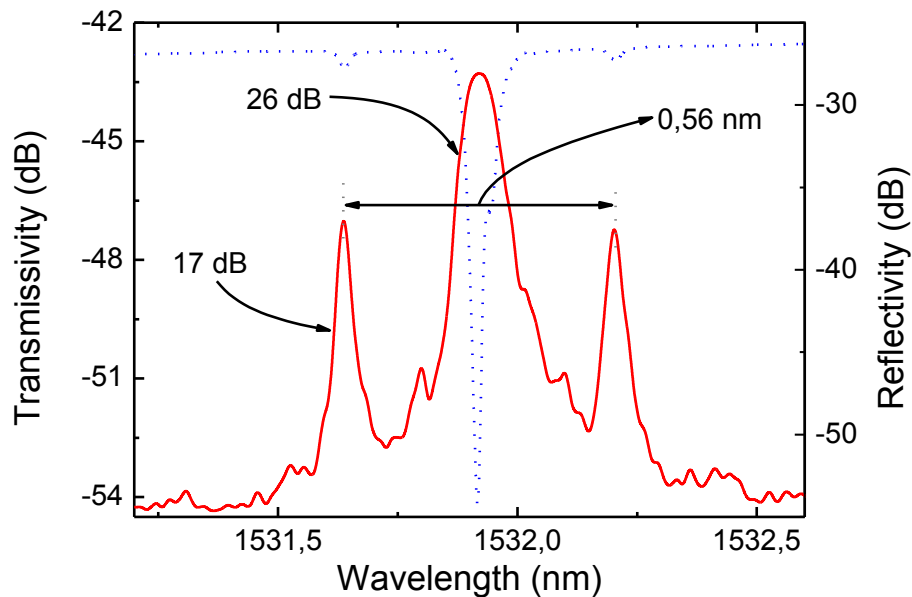
Figure 5.19 - FBG reflection and transmitted spectra after the writing process under acousto-optic modulation of the fiber at $f = 1,021$ MHz.
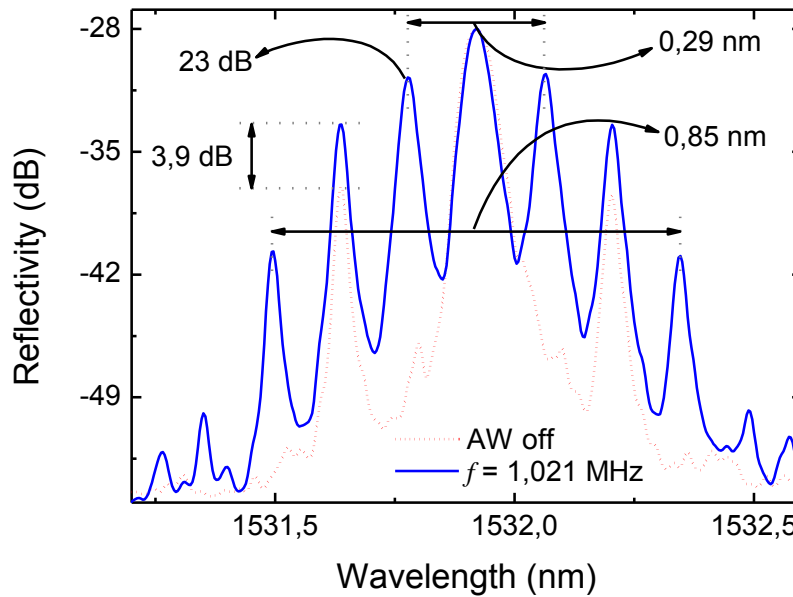
Figure 5.20 - Post-writing excitation of the sampled grating at *f* = 1,021 MHz. This effect allows the possibility of sampling sampled gratings.

Figure 5.21 shows another recording of a sampled grating. In this case, four side bands were formed due to the modulation of the grating period creating a sampled grating with 5 distinct peaks, considering the acoustic excitation at f = 919 kHz. The separation between the generated side bands is $\Delta\lambda$ = 0,48 nm for the primary lobes and $\Delta\lambda$ = 0,88 nm for the secondary ones (while for f = 1,021 MHz, the separation between the primary lobes is $\Delta\lambda$ = 0,56 nm with no formation of the secondary ones, due, perhaps, to misalignment of the fiber during writing). Figure 5.22 shows the comparison between the FBG spectrum at rest after the writing process and the simulation result, achieved through the numerical approach that employs the FEM associated with the TMM. The case when no acoustic wave excites the fiber during the writing process is also shown in figure 5.21.
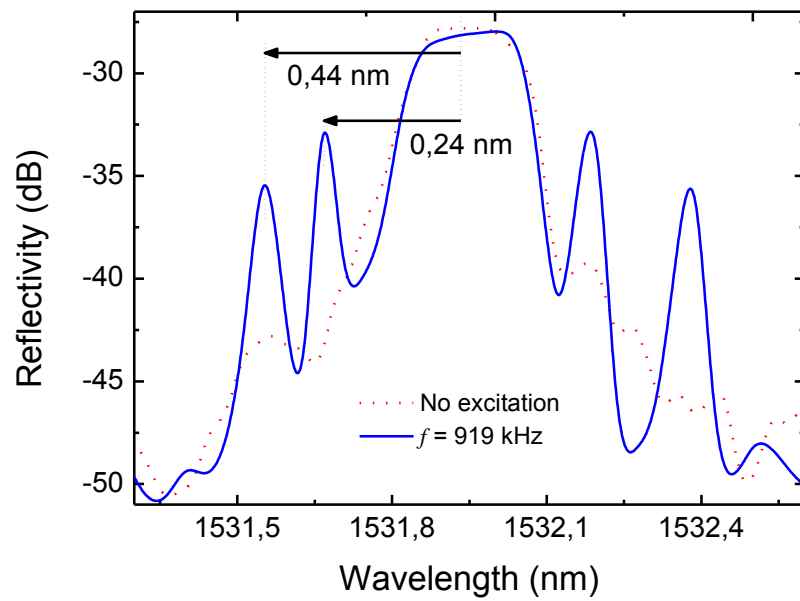
Figure 5.21 - Comparison between the achieved FBG spectrum when no acoustic wave excites the fiber during the writing process and when an f = 919 kHz acoustic wave excites the fiber.
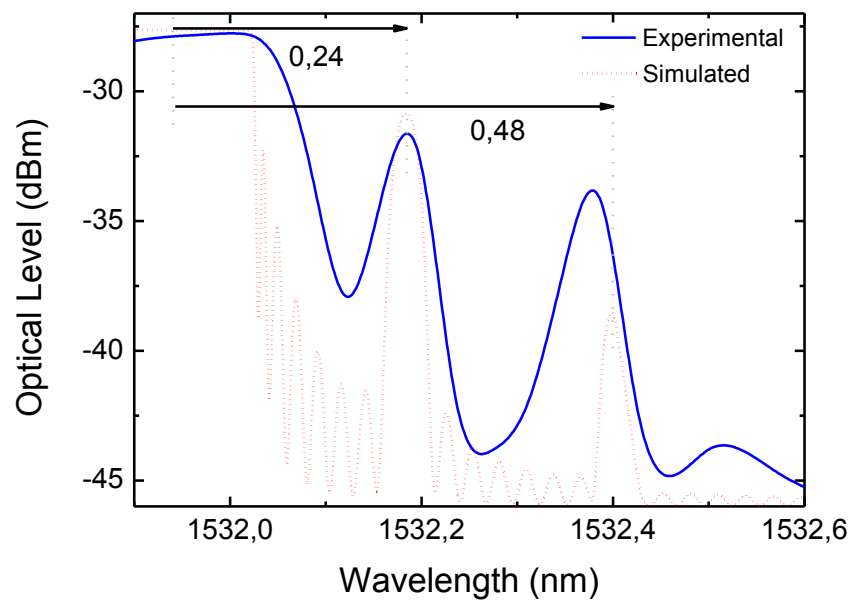
Figure 5.22 - Experimental and theoretical comparison of the FBG inscription in acoustically excited optical fiber.

5.4.2.2 Phase-shifted fiber Bragg grating and Fabry-Perot cavities

The possibility of modulating the fiber during the writing process leads to other special gratings, depending on the nature of the acoustic excitation. In section 5.4.2.1, the discussion about the excitation of longitudinal waves, giving rise to the generation of permanent sampled gratings, showed the feasibility of the technique. In the same way, by means of controlling the flexural excitation, it is possible to write special types of gratings. Basically, the idea is to use the acoustic wave to switch the writing process, whose mechanism is based on the scattering of the light and misalignment of the fiber core. The diagram shown in figure 5.23 exemplifies the expected effect. When the fiber is at rest, the UV light induces a refractive index change in the core (figure 5.23(a)), whereas when the fiber is flexurally excited (figure 5.23(b)), there is no photoinduced changes because the dither of the core in relation to the interferometric pattern makes the light scatter, avoiding the UV light to reach the fiber core. This effect can be used to create interferometric cavities, formed by a comb of gratings (Bragg grating mirrors), intrinsic fiber Fabry-Perot (F-P) interferometers and phase-shifted FBGs.
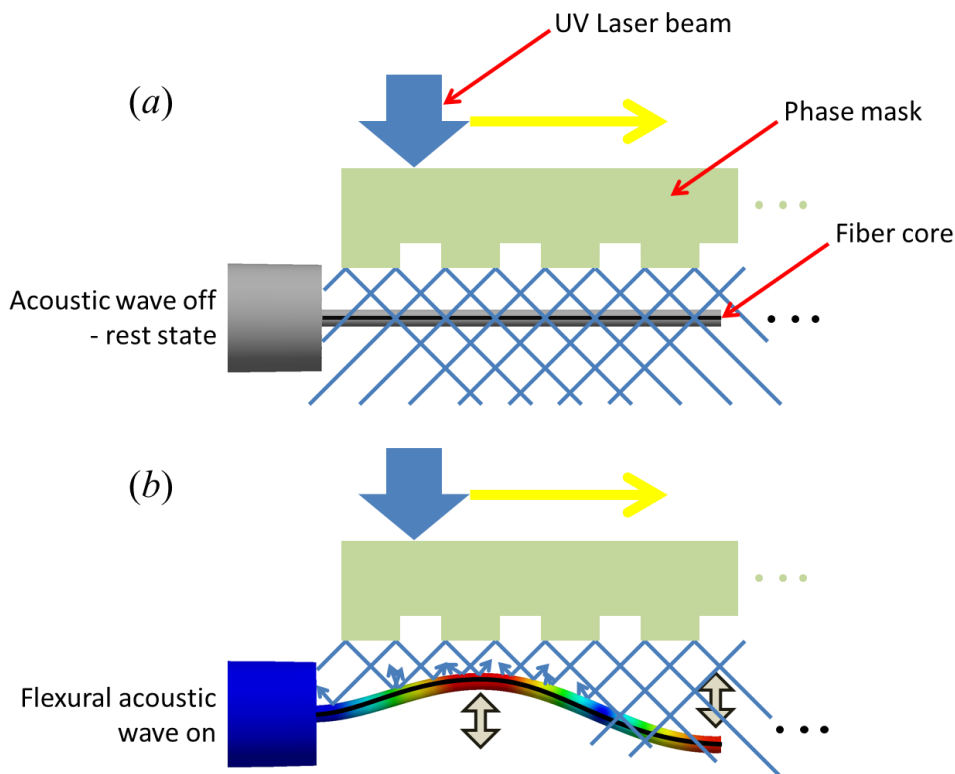
Figure 5.23 - Diagram of the photoinduced refractive index change through the phase mask technique (a) when the fiber is at rest and (b) when a flexural acoustic wave excites the fiber.

Figure 5.26 shows the FBG spectrum written using the same setup of figure 5.17, considering the excitation of a flexural wave during the sweep of the UV beam over the fiber. In this case, the acoustic wave is not constantly on, but periodically turned on and off for an certain period of time, t_b (using the burst function of the RF signal generator). Considering a RF signal with 100 cycles, for different frequencies, the burst mode of the RF generator creates a signal that switches the acoustic excitation, for a certain period of time, on and off. The graph that represents the RF excitation time is shown in figure 5.24, where the t_b corresponds to the interval between bursts of 100 cycles, since the RF frequency at $f = 40{,}9$ kHz is considered.
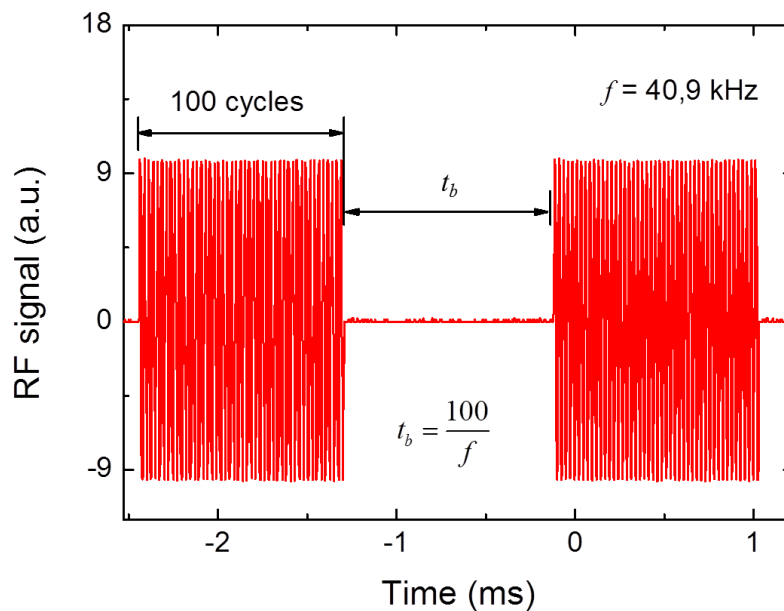
Figure 5.24 - Burst mode excitation of the PZT. The burst time, t_b, corresponds to the time between bursts of 100 cycles.

In summary, when the acoustic wave is on, no grating is written in the fiber. By using the frequency generator in the burst mode, it is possible to set the distance between the gratings, which can be controlled over the acoustic frequency and the burst time. 100 cycles was first chosen randomly, but it represents the correspondent length of the grating. The sweep time of the UV beam over the phase mask is also critical. Therefore, a good control of these parameters allows the generation of special fiber gratings. Figure 5.25 shows a schematic of the technique adopted for writing Fabry Perot interferometers using Bragg gratings mirrors.
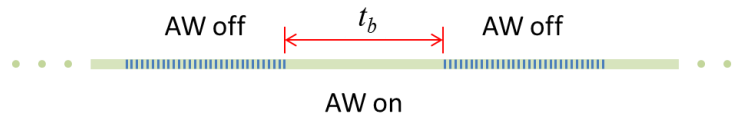
Figure 5.25 - Schematic diagram of the Fabry Perot interferometers writing process under excitation of flexural acoustic waves.

Figure 5.26 shows the fabricated F-P interferometer considering different frequencies applied on the modulator. The solid curve represents a standard F-P interferometer formed by six gratings of approximately $l_g \approx 4{,}5$ mm uniformly separated, obtained by sweeping the modulated UV beam over the phase mask length ($l_{pm} = 50$ mm). The sweep time (t_{sw}) was set at $t_{sw} = 10$ mm/min. Depending on the acoustic frequency, the length of each segment of FBG can be set. When $f = 306$ kHz, the achieved grating corresponds to the approximately four gratings written in the 5 cm long piece of fiber, which means that a four planes F-P interferometer is generated, whereas for $f = 75$ kHz, the structure corresponds to the generation of two planes, i.e. two series of cascade Bragg gratings. This proves that the technique can be used to write customized F-P interferometers directly.
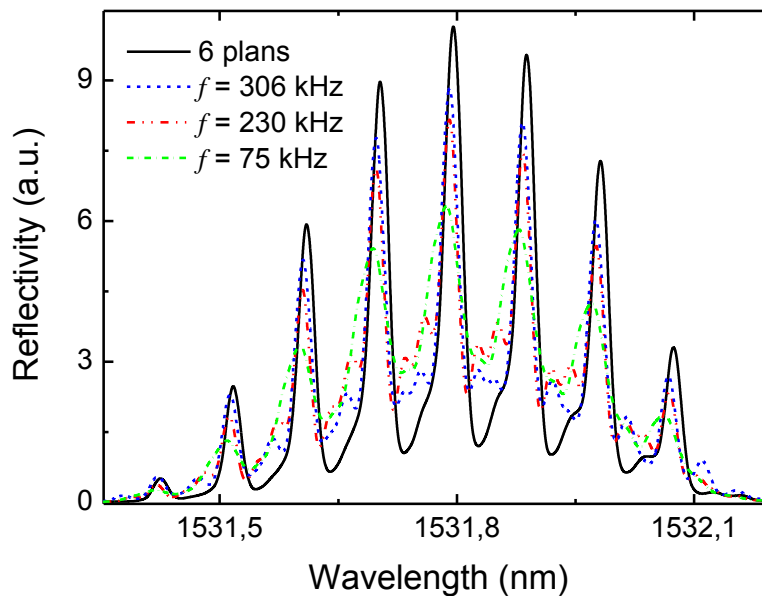
Figure 5.26 - F-P interferometers written using a direct UV beam modulation methodology (solid curve) and by means of acoustic waves.

On the other hand, if the burst time is tuned, keeping the frequency constant, the modulation conditions are changed and different configuration of resonant cavities can be

obtained. For example, the number of planes and length of the Bragg mirrors is related to the period of the modulation. Figure 5.27 shows the resultant FBG spectrum when f = 113 kHz acoustic frequency excites the PZT using the burst function, setting the modulation period at t_b = 0,5 s, 1 s, 2 s and 4 s. Increasing the period, the side lobes period decreases. Moreover, for the case when the modulation is continuous, the period tends to zero, and a sync-sampled fiber grating (IBSEN *et al*, 1998) with a phase-shifted spectrum (similar to a phase-shifted Moiré grating (REID *et al*, 1990)) is generated, as shown in figure 5.28. The inset scheme of figure 5.28 shows the resultant effective index modulation of the fibre core shaped by the flexural acoustic wave.
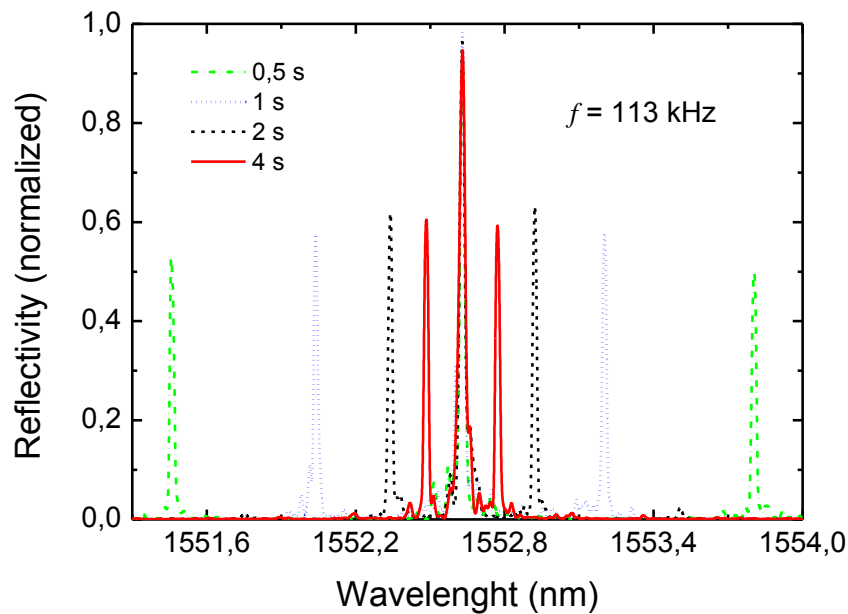
Figure 5.27 - Permanent resonant cavities achieved through the acousto-optic modulated FBG writing process methodology.

126
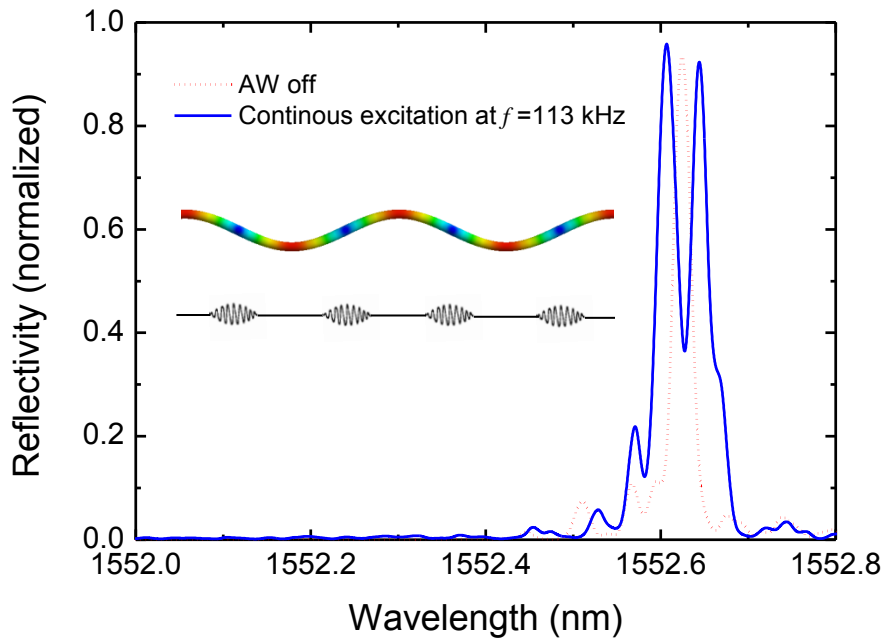
Figure 5.28 - Phase-shifted FBG spectrum. Inset: Resultant index modulation shaped by the acoustic wave.

5.5 VISCOSITY SENSOR

5.5.1 Viscosity sensing

The viscosity is characterized by the resistance of a material to flow. It is one of the main physical properties used to predict a number of other physical, chemical and biological parameters of a fluid (SRIVASTAVA *et al*, 2005). Density, stability, chemical content, molecular weight and color are examples of such properties that can be determined through the accurate measurement of viscosity (SRIVASTAVA *et al*, 2005; HENSON *et al*, 1953). The precise and real-time measurement of this parameter potentially allows monitoring of chemical reactions. For example, in manufacturing industries, viscosity can help control new material quality and homogeneity (DAVIS, 2007; FERRARIS, 1999). Another example is the production of paints and varnishes where such a measurement could help control thicknesses and texture (HENSON *et al*, 1953; BIDLACK and FASIG, 1951). In the field of food engineering, the application of viscosity measurements allows the control of the quantity, behavior and functionality of proteins in a given food system (DAVIS, 2007; CULLEN *et al*, 2000; CHERRY, 1981; BOURNE, 2002). Usually, the measurement of viscosity involves dynamic interrogation of the material under test and it can be based on vibrational and

rotational elements (sometimes called cone and plate viscometers, respectively) (BARBER *et al*, 1955; SUSUKI *et al*, 1990).

A viscometer, also called viscosimeter, consists of an instrument used to measure the viscosity of a fluid. Examples of commercial viscometers are the capillary (IRANY, 1944; UBBELOHDE, 1936; PAYNE, 1937; STARK *et al*, 1975), falling sphere (SUTTERBY, 1973; WRIGHT, 1986; BRYAN and BRYAN, 1993), vibrational (PORTMAN JR. and MARGRAF, 1989; FARONE *et al*, 2002), rotational (DAVID and CAMPBELL, 1960; PALMER, 1977; DAO *et al*, 2009), among others.

The capillary viscometer, also known as Ostwald viscometer is formed by a capillary glass tube (U-shaped) and bulbs containing default liquids, as shown in figure 5.29. When in use, a liquid is drawn into the upper bulb (right hand arm), then allowed to flow down through the capillary into the lowest bulb. Two marks (one above and one below the upper bulb) indicate a known volume. The time taken for the level of the liquid to pass between these marks is proportional to the viscosity. This device presents an ideal solution for small volume of measurand, however, the measurement time can be long, preventing a faster assessment of the parameter (real-time monitoring).
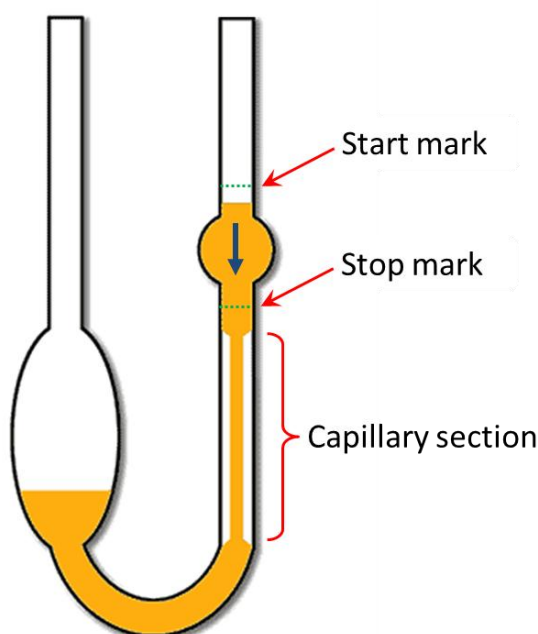
Figure 5.29 - Capillary viscometer scheme.

The falling sphere viscometer gives the viscosity through the measurement of the falling velocity of a sphere inside the fluid. This viscometer is based on the Stokes' law, where such configuration consists of a sphere of known size and density, which is allowed to

descend through the liquid. Its terminal velocity, which can be measured by the time it takes to pass two marks on the tube, is used to calculate the viscosity of the fluid according to the Stokes law. A series of steel ball bearings of different diameters are normally used in the classic experiment to improve the accuracy of the calculation. However, this viscometer presents the disadvantage of been massive, time consuming and does not present an efficient measurement.

Commercially, the most common viscometers founded are based on the rotational and vibrational technique. Rotational viscometers use the idea that the torque required to turn an object in a fluid is a function of the viscosity of that fluid. They measure the torque required to rotate an object in a fluid at a known speed. Vibrational viscometers operate by measuring the damping of an oscillating resonator immersed in a fluid. The resonator generally oscillates in torsion or transversely. The higher the viscosity, the larger the damping imposed on the resonator. Figure 5.30 shows an example of a commercial rotational viscometer. This viscometer is suitable for investigating the mixing, stirring, and pumping behavior of coatings, emulsions, and dispersions, as well as for performing conventional flow and viscosity profile experiments. However, as most of the viscometer founded in the market, it is robust, not portable and do not allow in situ measurements. In addition its main parts are made of external interference susceptible materials.

This work introduces an alternative compact dip-style viscometer based on the acoustic excitation of a fiber long period grating and an all-optical interrogation technique. This is the first optical fiber sensor able to measure the viscosity by adding a dynamic component to the fiber.

**Figure 5.30 - Vibrational viscometer distributed by MERLIN
(http://www.atsrheosystems.com/products/merlin.html).**

5.5.2   Sensor design

As discussed in section 2.1.2, about long period gratings, changes in the external refractive index manifest itself as a change in the grating dip wavelength and minimum transmissivity. However, to obtain the measurement of more challenging external parameters, such as viscosity, a temporal element has to be added to the LPG response. This is achieved by using the acousto-optic modulator to excite a flexural acoustic wave, forming bends in the fiber along its length. This effect modifies the coupling coefficients of the LPG, shifting the peak wavelength and changing the maximum attenuation coefficient, depending on the acoustic frequency and intensity (OLIVEIRA *et al*, 2011). The viscosity measurement is obtained by recording the optical response that depends critically on the damping of the acoustic wave by the surrounding medium. Figure 5.31 shows the schematic diagram showing how the viscosity damps the acoustic wave. Figure 5.31(a) shows the silica-horn fiber at rest, and figure 5.31(b) shows the formation of a flexural wave, and how the acoustic wave damps, considering an increasing of the surrounding viscosity (η) where the fiber is immersed. The higher the viscosity, the lower the amplitude of the acoustic wave.
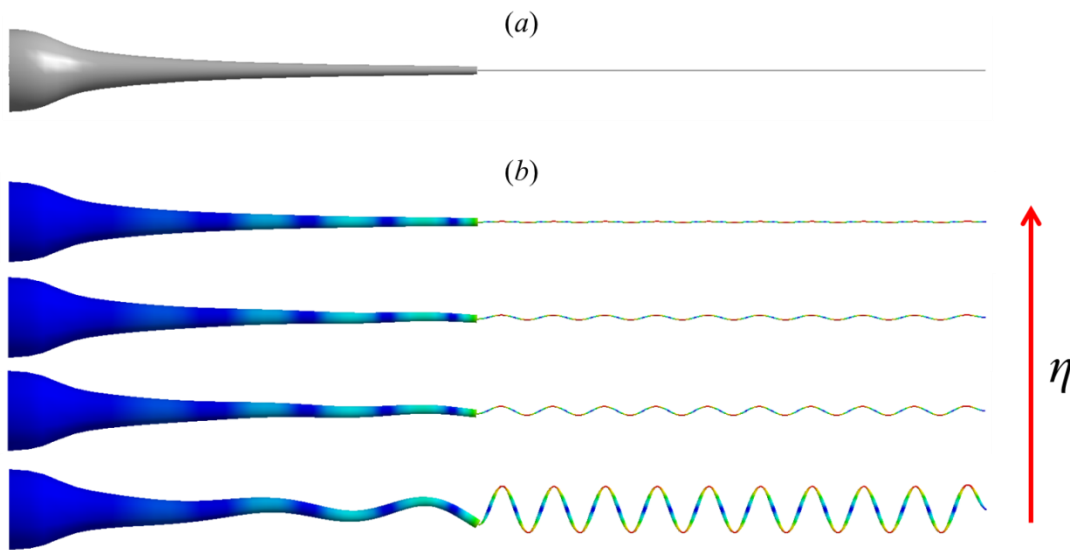
Figure 5.31 - Acoustic behavior of the silica-horn - fiber set when (*a*) at rest and (*b*) acoustically excited, considering an increase in the external viscosity.

This application demonstrates how a LPG can be used to sense, among all the well-known parameters that are sensitive to, such as temperature, pressure, strain and so on, the viscosity. Moreover, this sensor allows viscosity to be measured *in situ* with a compact dip-style sensor head by examining the frequency response to the applied modulation. Combined with dynamic analysis offered by an acoustic wave, the LPG sensor can provide real-time measurements. The damped frequency response is a direct measure of the relaxation time associated with viscous flow – the more viscous the flow the slower the relaxation after the impulse signal is applied. Considering practical implementation issues, a novel design for a viscosity sensor is presented, including the possibility of a disposable sensor head.

The sensor head is composed of a fiber connector, a holder, a PZT, a silica horn and a fiber containing the LPG. At the end of the fiber a silver mirror is deposited in order to allow the transmission spectrum to be recorded in reflection – for potential multiplexing of a distributed set of viscometers, which may be of interest in larger industrial processes, the device can equally operate in transmission. However, operation in reflection avoids the necessity of tight bending of the fiber and reduces the device length, making the device more robust. A glass capsule can be used to protect the fiber and isolate the silica horn, as shown in figure 5.32. The final length of the device (considering practical dimensions) is $l_{vs} = 98,4$ mm, which is compact and portable relative to most commercial instruments.
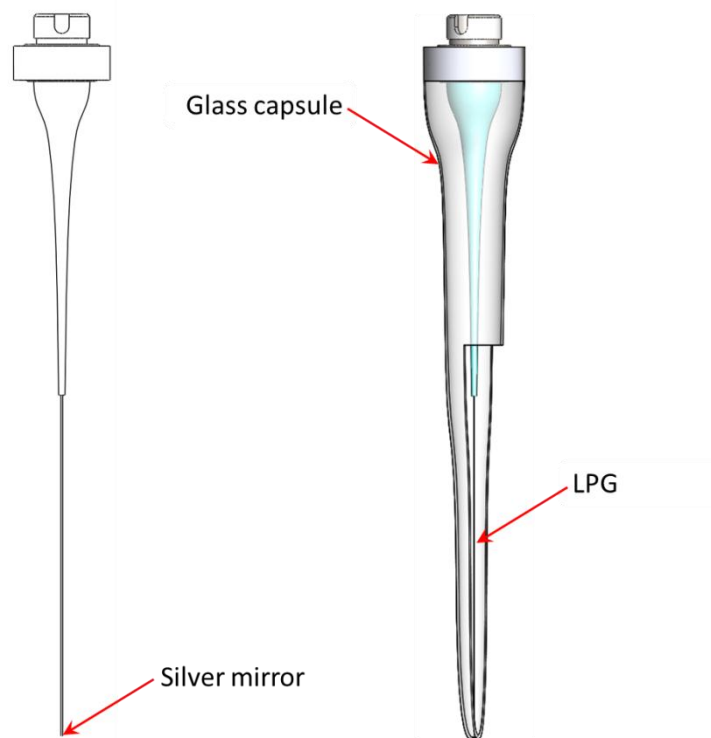
Figure 5.32 - The sensor head. The glass capsule is used to protect the silica horn and the grating.

Interrogation techniques, such as that based on derivative spectroscopy (ALLSOP *et al*, 2004), fiber-loop ring-down spectroscopy - FLRDS (BROWN *et al*, 2000) and arrayed waveguide gratings - AWG (SANO and YOSHINO, 2003) can be coupled to the sensor head to perform the required measurements. These techniques may be combined with other systems such as those using FBG references, for example. Figure 5.33 shows the block diagram of the sensor with the setup consisting of the LPG acousto-optic modulator, an acoustic excitation driver, interrogation stage and results display. Besides viscosity, the sensor measures all the well-known parameters which are often assessed by an LPG (e.g. temperature, refractive index, density and hydrostatic pressure).
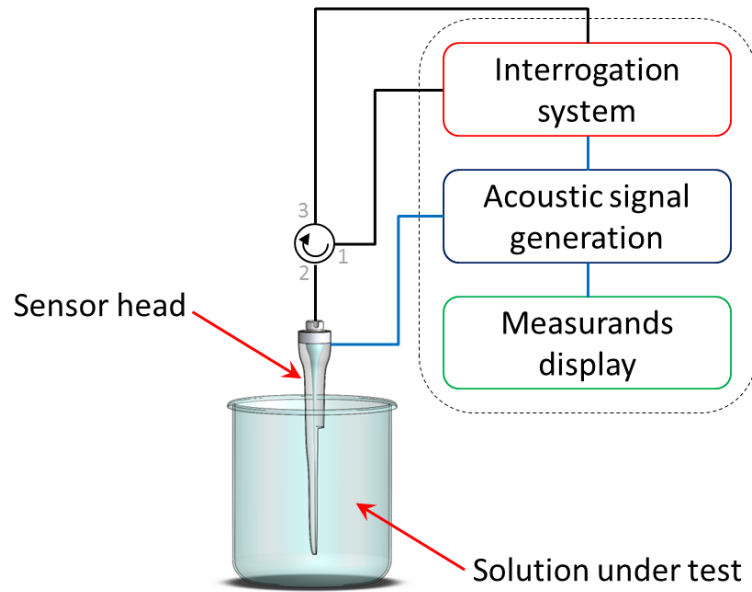
Figure 5.33 - Block diagram of the designed multiparameter sensor.

5.5.3   Laboratory version of the viscosity sensor

For demonstration purposes, a bench-top laboratory version of the proposed design was assembled, as shown in figure 5.34. The LPG (l_g = 40 mm) was inscribed in a standard boron co-doped germanosilicate fiber (cutoff ~ 1300 nm) using a 193 nm ArF laser with a central wavelength of λ_m = 1556 nm. The setup is composed by an arbitrary function generator, responsible for the excitation of the PZT, an optical source (amplified spontaneous emission (ASE) light source) to verify the grating spectrum using the optical spectrum analyzer (OSA), a tunable laser for the dynamic measurement using the photodetector and an oscilloscope synchronized with the arbitrary function generator to display the transient and damping values. The optical switch is used to set whether a tunable laser or an ASE is employed. Figure 5.35 shows a photography of the experimental assembly.
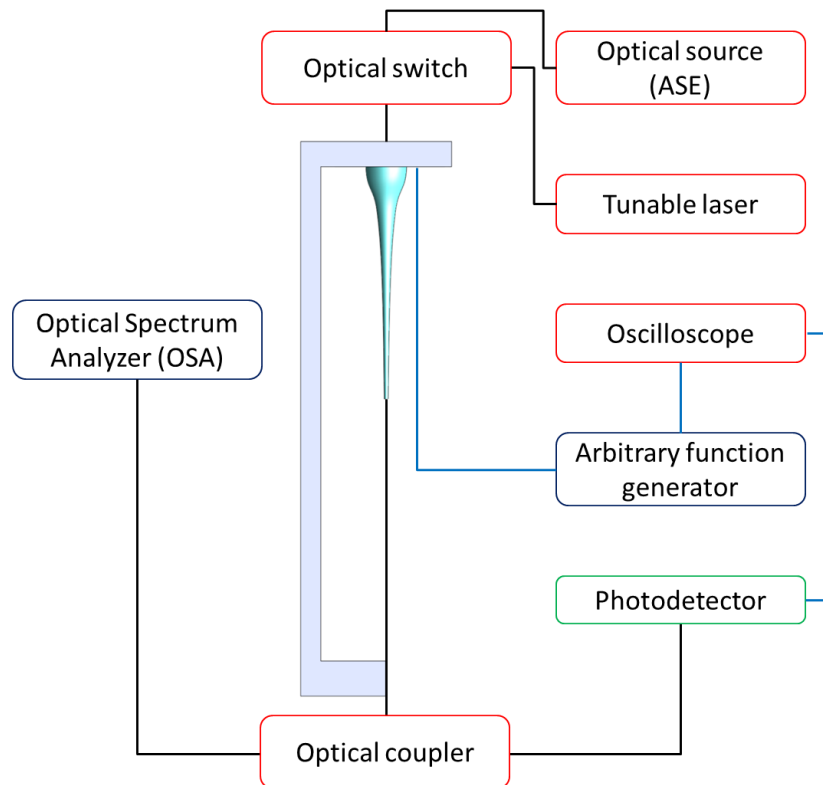
Figure 5.34 - Block diagram of the experimental setup.
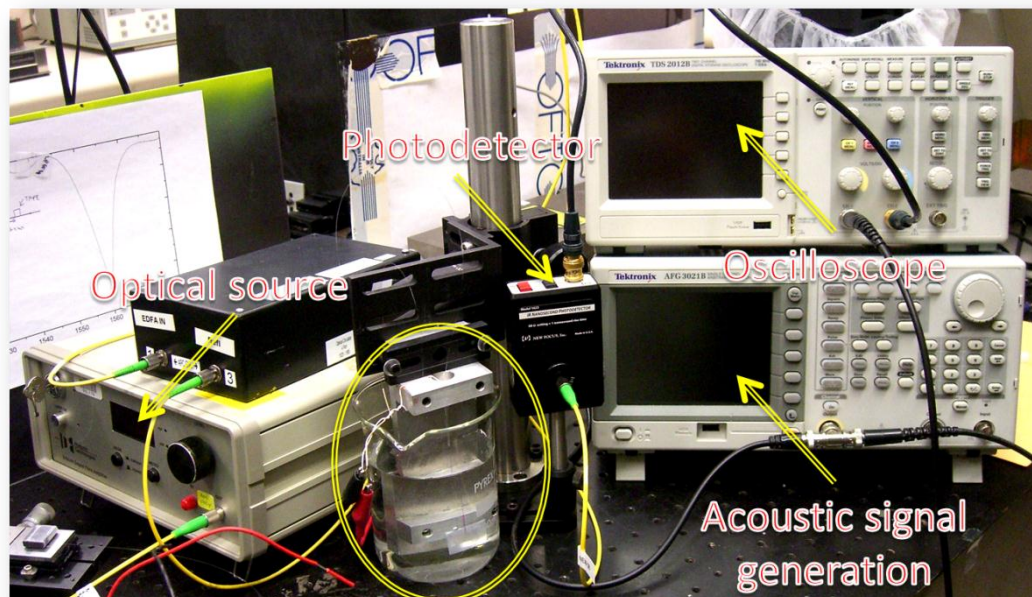
Figure 5.35 - Photography of the experimental assembly of the laboratory prototype of the sensor.

The solution used to calibrate the system was an anhydrous D(+)-glucose ($C_6H_{12}O_6$) in de-ionized and distilled water. This is a solution with a well-known refractive index and viscosity as a function of concentration and is often used to characterize and calibrate

134

commercial devices (LIDE, 2008). The density, ρ, and the refractive index, n, of the solution varies linearly from $\rho = 1$ (pure water) to 1,2793 g/cm^3 and from $n = 1,334$ to 1,4394 at a concentration $[C_6H_{12}O_6] = 8,326$ mol/L respectively. These literature values for refractive index were corroborated using an LED refractometer at 1550 nm. The viscosity, η, on the other hand, varies from $\eta = 1,021$ to 37,445 mPa.s (LIDE, 2008).

When the solute is added to the stock solution into which the sensor head is dipped, the density and the refractive index change, modifying the peak wavelength and the minimum transmissivity of the LPG. Figure 5.36 shows the dependence of the refractive index and the LPG peak wavelength shift ($\Delta\lambda$) in agreement with that measured using an optical refractometer. In the same way, the density (ρ) has a linear dependence with the refractive index (n), whilst the peak wavelength shift, from which the change in refractive index can be extracted, has a quadratic dependence, since the configuration involves a cylindrical waveguide. This quadratic dependence can be used to predict the value of the density in a multi-parameter sensor, in a passive way (with no acoustic wave).
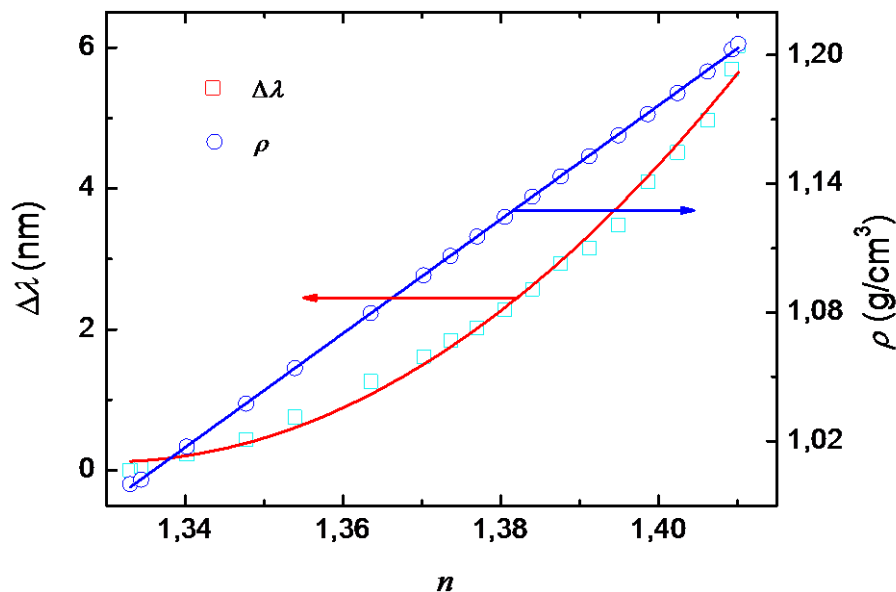
Figure 5.36 - Refractive index, n, versus peak wavelength shift, $\Delta\lambda$. The refractive index is also related to the density, ρ, of a solution (as calculated).

5.5.4 The acousto-optic characterization of the sensor

Figure 5.37 shows the transmission spectrum of the LPG when the fiber is at rest and when an acoustic wave excites the fiber at $f = 39,9$ kHz, which is immersed in solutions with

$[C_6H_{12}O_6]$ = 0,056 and 4,724 mol/L respectively. The acoustic wave induces a blue-shift and an increase in peak attenuation as well as narrowing of the rejection band with increasing concentration. Whilst the acoustic modulation shifts the LPG spectrum to longer wavelengths, the impact of the acousto-optic modulation is reduced when the $C_6H_{12}O_6$ concentration increases, in part due to a change in refractive index and phase detuning but also as a result of damping of the acoustic wave with increasing viscosity. For example, the peak wavelength shift, for $[C_6H_{12}O_6]$ = 0,056 and 4,724 mol/L is $\Delta\lambda$ = 6,89 and 1,25 nm, respectively, while the increase in transmittance, ΔT, is $\Delta T \sim$ 15,67 and $\sim$ 1,70 dB, respectively. Figure 5.38 shows the 3-D variation of the LPG attenuation peak when the $C_6H_{12}O_6$ concentration increases and the fiber is excited at f = 39,9 kHz. The response is complex and both wavelength and transmittance are non-linear with increasing concentration under the same applied acoustic frequency (f = 39,9 kHz).
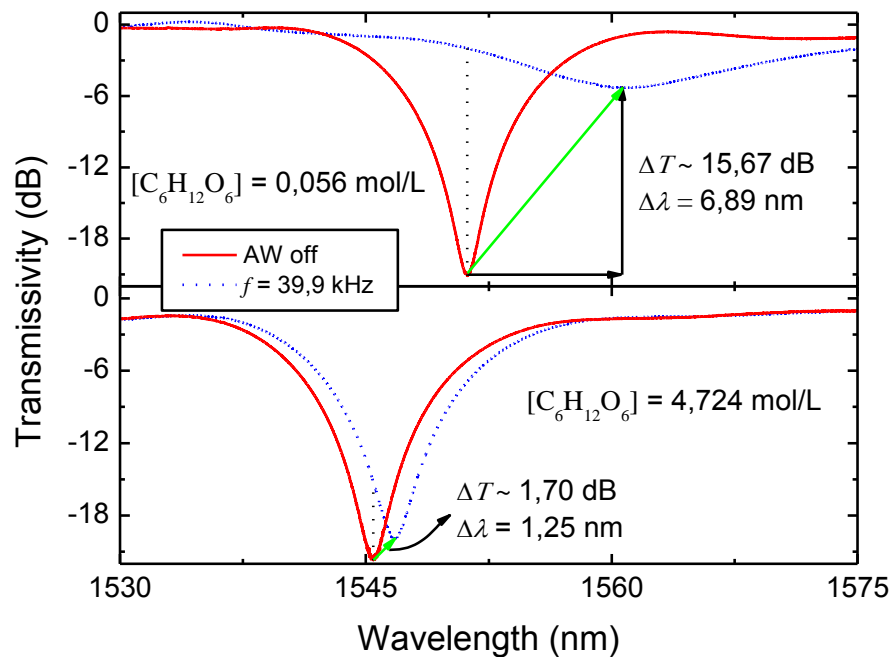
Figure 5.37 - LPG transmission spectra when immersed in $[C_6H_{12}O_6]$ = 0,056 and 4,724 mol/L D(+)-Glucose solution at rest and when f = 39,9 kHz acoustic wave excites the fiber. The red curves represents the LPG spectrum when the fiber is at rest.
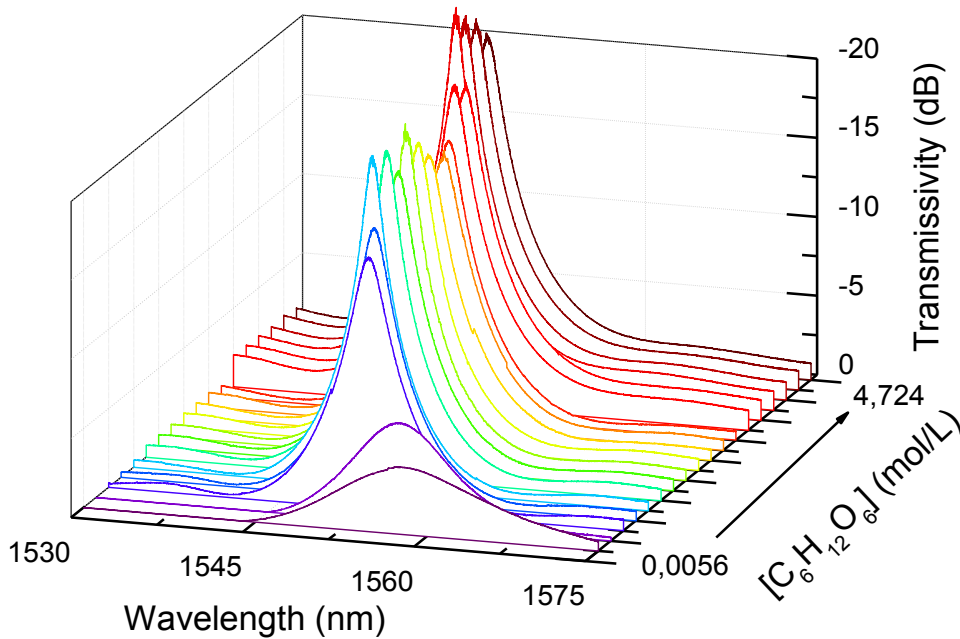
Figure 5.38 - Transmittance spectra versus increasing of $C_6H_{12}O_6$ concentration.

Figure 5.39 shows the induced wavelength change ($\Delta\lambda$) as a function of $C_6H_{12}O_6$ concentration. At low concentrations, there appears to be a quadratic dependence of $\Delta\lambda$ for solute concentrations up to $[C_6H_{12}O_6] \sim 1,75$ mol/L. Between $[C_6H_{12}O_6] \sim 1,5$ and 3 mol/L there is a reverse change leading to an increase in the wavelength shift. Figure 5.40 shows a similar response for the peak transmittance, ΔT, plotted against concentration. For concentrations up to $\sim 1,75$ mol/L, which correspond to a viscosity of $\eta \sim 2,42$ mPa.s a quadratic relationship of ΔT and concentration is observed. At higher concentrations, the behavior is similar to the previous analysis ($\Delta\lambda \times [C_6H_{12}O_6]$), which makes the use of these average parameters impracticable for sensing when there is an applied acoustic frequency. However, if measurements are taken rapidly in time an initial red-shift of the spectrum will be accompanied by a small blue-shift as a result of the initial excitation followed by the establishment of the damped standing wave – the non-linear profile likely reflects a complex contribution from a finite spectrum collection time using an OSA relative to the mechanical relaxation time (after a "threshold" viscosity around $\eta = 2,42$ mPa.s).
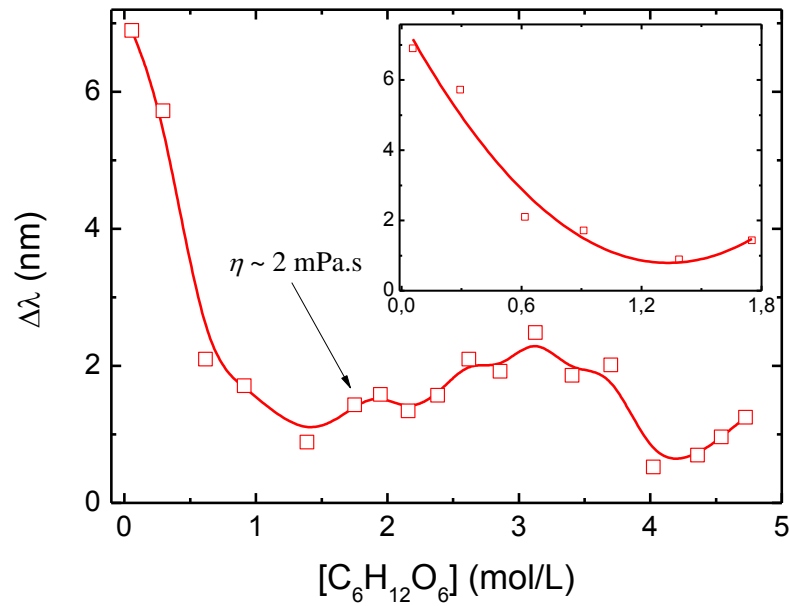
Figure 5.39 - Peak wavelength shift at the acoustic resonance (f = 39,9 kHz). A quadratic fit is shown for glucose concentrations up to [C$_6$H$_{12}$O$_6$] ~ 1,75 mol/L (inset graph).
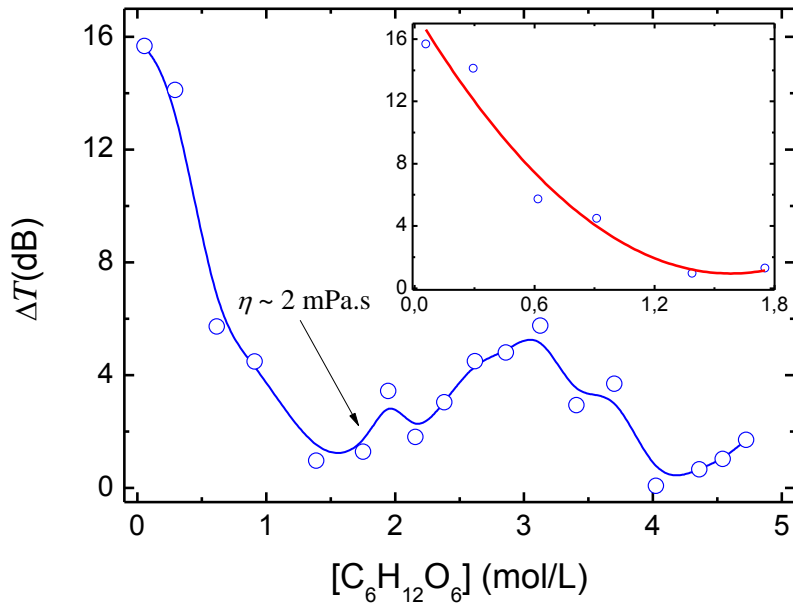
Figure 5.40 - Transmittance shift at the transmission peak when the acoustic wave excites the fibre at f = 39,9 kHz.

138

5.5.5   Dynamic analysis

Figure 5.41 shows the time characterization of the sensor. When the acoustic wave is switched on, the LPG spectrum is shifted, and a maximum signal level in the photodetector is reached quickly. This time is the transition time (τ_r), which corresponds to the first excitation of the fiber. However, a relaxation following this one, corresponding to the damping of the fiber bends by the viscous solution, is expected. This effect corresponds to a small signal reduction in the photodetector. As this measurement is time dependent, there is a finite time (τ_s') before the fiber relaxes for a full relaxation at τ_s, point when a standing wave is established. For comparison purposes, if the wavelength is fixed at the wavelength corresponding to the peak wavelength when the acoustic wave is off in figure 5.37, when interrogating with a narrow linewidth laser, a small shift in the transmittance and peak wavelength will not represent a measurable change in the photodetector for lower concentration ($[C_6H_{12}O_6] = 0{,}0056$ mol/L), while for higher concentration ($[C_6H_{12}O_6] = 4{,}724$ mol/L), it will be detected (see figure 5.42).
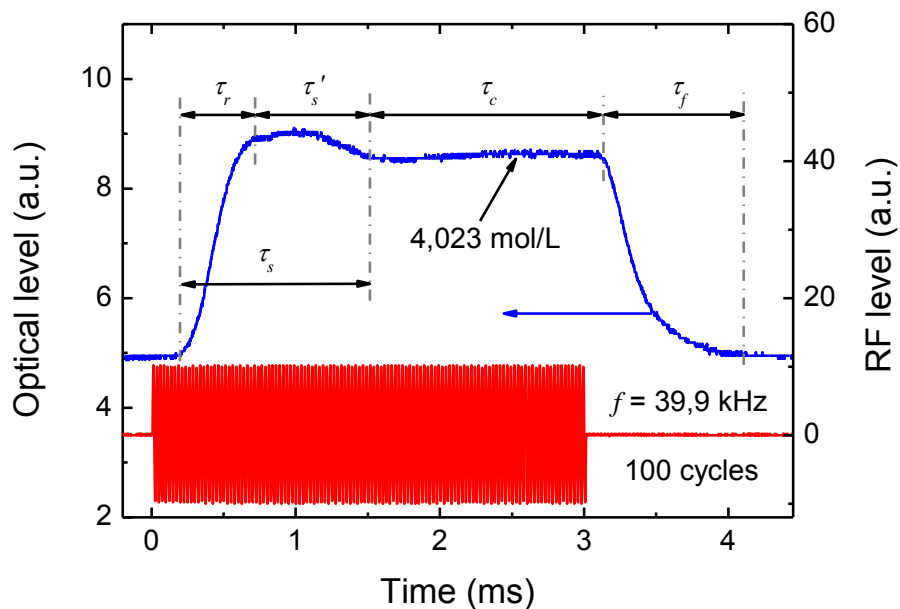
Figure 5.41 - Time parameters considering a solution with $[C_6H_{12}O_6] = 4{,}023$ mol/L.

A means of separating out the excitation and relaxation time by measuring τ_r or $\tau_s' = (\tau_s - \tau_r)$ to obtain a linear relationship between $[C_6H_{12}O_6]$ and time (and therefore η) was developed. This behavior occurs only for viscosity values higher than 2,24 mPa.s, due to the weaker acoustic efficiency, which emphasizes the changes in optical power. This viscosity

value is consistent with the threshold value in figures 5.39 and 5.40. For the sake of consistency with rise time measurements, time is measured as the 5-95 % confidence level of the rise. The measurement time is controlled by controlling the number of cycles used to excite the grating. In this case, 100 cycles were used, representing a total measured time $t = \sim 4$ ms, or a sample frequency of $f_m \sim 250$ Hz, which can be increased up to $f_m \sim 700$ Hz. The time at which the photodetector signal reaches a constant value is labeled the constant level time, τ_c, and is related to the inertia of the fiber after the solution causes the relaxation around it (corresponds to the generation of a standing wave). When the acoustic wave is switched off, the LPG relaxes and experiences a fall time (τ_f) back to the rest state. Figure 5.41 shows the defined time constants and the dynamic behavior of the LPG when immersed in a solution with $[C_6H_{12}O_6] = 4{,}023$ mol/L for 100 cycles acoustic excitation at $f = 39{,}9$ kHz, while figure 5.42 shows the time characterization for various glucose concentration.
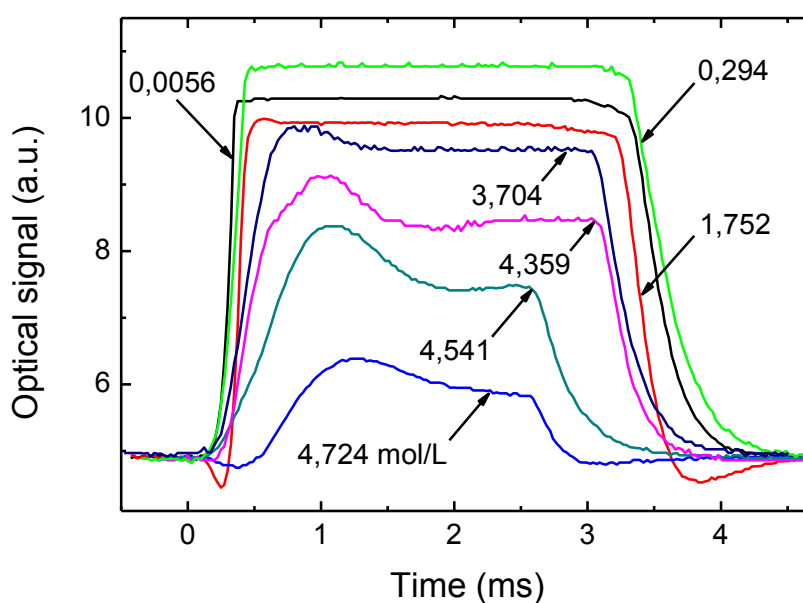
Figure 5.42 - Time behavior of the sensor for various solution concentrations.

5.5.6   The viscosity measurement

Figure 5.43 shows the behavior of the viscosity and rise time depending on the glucose concentration. The viscosity is directly related to $[C_6H_{12}O_6]$ through a quadratic dependence (LIDE, 2008), and given that the rise time and concentration both have a quadratic dependency as well, this means that the viscosity has a linear dependence with rise time (figure 5.44).
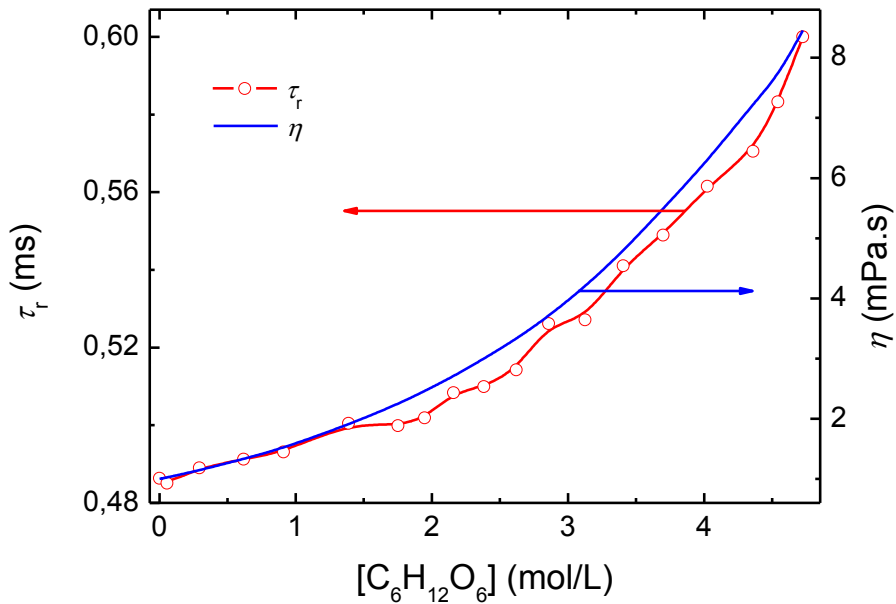
Figure 5.43 - Quadratic relationship between glucose concentration and rise time and viscosity.

Figure 5.44 shows the linear dependence for both the rise time and the total relaxation time, τ_s, with the viscosity. Both increase when η increases, consistent with the damping of the acoustic wave by the solution. These linear relations therefore make viscosity measurements straightforward:

$$\eta = \left(-31,80 + 67,76 * \tau_r\right) \pm 0,76 \text{ mPa.s} \tag{5.1}$$

and

$$\eta = \left(0,10 + 4,61 * \tau_s\right) \pm 0,15 \text{ mPa.s.} \tag{5.2}$$

By confining the measurements to τ_r, a substantially larger viscosity range becomes possible although with lower resolution. Further, the need to consider a threshold is removed and the process is entirely linear. If the sensitivity parameter, S_η, is redefined as the slope of the curves, $S_\eta = 67,76$ mPa.s/ms for the initial excitation and $S_\eta = 4,61$ mPa.s/ms for the total relaxation time are achieved. Given that both cases are linear, the observed complex response of the average spectral parameters seems most likely to arise from time mismatch between OSA spectrum collection and the two contributions to relaxation. The total relaxation time presents a higher resolution and, therefore, greater sensitivity for viscosity measurements higher than $\eta = 2,24$ mPa.s.
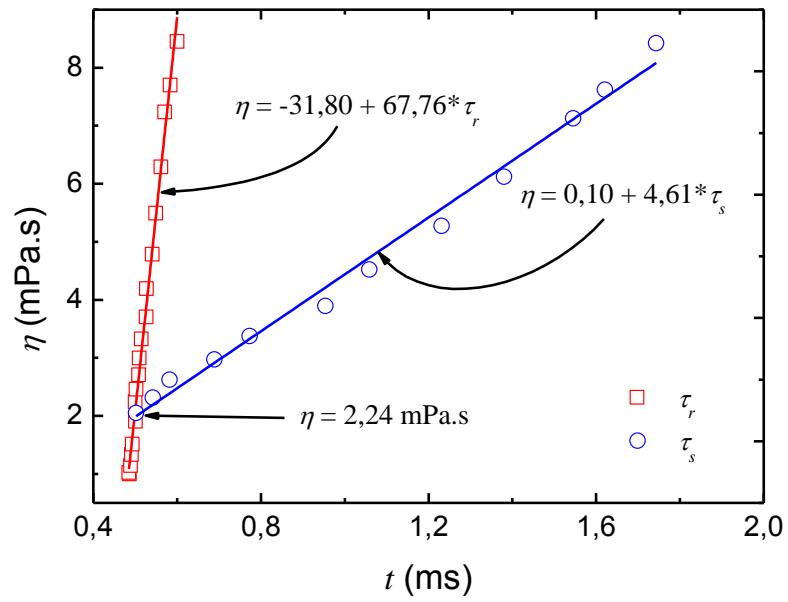
Figure 5.44 - The viscosity *versus* time behavior.

6 CONCLUSIONS

6.1 GENERAL CONCLUSIONS

The Acousto optic effect has been explored regarding the excitation of different resonant modes in the silica horn – fiber set. Numerical approaches based on the combination of the finite elements, assumed modes and transfer matrix methods were used in order to model the devices, simulate the effect and calculate some grating properties. It was achieved that flexural and longitudinal excitation modes can be excited using a single acousto-optic modulator device, which opens up a large range of applications.

By using fiber Bragg gratings (FBG) and long period gratings (LPG), the acousto-optic effect was employed in several situations. In the low frequency regime, when flexural modes predominate, the effect experienced by FBGs is a reflectivity decay, due to a mismatch between the co-propagating and counter propagating modes as a consequence of bends generated in the fiber. In the LPG case, the increase of the flexural acoustic wave intensity reduces the dip transmissivity of the LPG attenuation band and induces a shift of the spectrum to longer wavelengths. By changing the optical path and the difference between the effective refractive indices of the core and cladding modes and the overlap between them, the acoustic wave causes a reduction of the coupling coefficient and, consequently, a reduction of the dip transmissivity.

In the high frequency regime, where the excitation of compression and rarefaction strain fields in the fiber predominates, the acousto-optic effect is noticeable only when applied to FBGs, because its refractive index modulation period has the same order of magnitude of the induced longitudinal displacement of the planes. It leads to the superlattice modulation of the grating. In LPG, due to its larger modulation period, the longitudinal modulation does not change significantly the grating spectrum. However, the effect of induced bends in the fiber (flexural waves) is more evident in LPGs.

The complete characterization in the low and at high frequency regime made it possible to apply the modulator in different devices, by controlling the effect that is most suitable for the particular application. In this work, several devices were proposed, demonstrated and characterized, such as: a fast acousto-optic add-drop multiplexer, a tunable chromatic dispersion compensator, a phase-shifted FBG controller, a method to control the grating spectrum during the writing process and a viscosity sensor.

6.2   SPECIFIC CONCLUSIONS

6.2.1   Fast add-drop multiplexer

An add-drop multiplexer (ADM) with fast switching times has been presented. The response time of such device is limited by the speed of the acoustical wave through the entire modulator. Considering an interaction length of $L_i = 10$ cm and the speed of $c_{ext} = 5740$ m/s in silica, a switching time of $t_s = 17$ μs was measured. This can still be improved, if the interaction length and the acoustical frequency are optimized. Yet, this switching time is one of the smallest found in literature, which makes the device very promising for practical applications.

6.2.2   Chromatic dispersion compensator

It has been demonstrated that both the amplitude and frequency of an acoustic wave can be used to tune the dispersion slope and group delay ripple of a uniform FBG. By ensuring the induced strain profile is positioned properly over the grating length, an effective "dc apodisation" is achieved. If the broadening of the bandwidth over which the device works is equal or less than the channels bandwidth itself then this technique opens up an opportunity for the dispersion compensation of individual channels. In very complex systems where different channels travel different lengths and experience differing group delay and dispersion, this unique form of active channel control turns up to be an important solution. The achieved results can be improved by tailoring the uniform grating profile (including partial apodisation) to help reduce the GDR and to flatten the dispersion slope further. Additionally, this technique can be applied to tune much broader band devices, including existing chirped FBG compensators to enhance their tunability and performance.

6.2.3   New method to control the grating properties during the writing process

It has been demonstrated the capability of the acousto-optic device to modulate the FBG by acoustically exciting the fiber during the sweep of the UV beam in the writing process. Sampling of uniform Bragg grating in the presence of a longitudinal acoustic excitation gives rise to a permanent sampled grating. This arises from the modulation of the refractive index period through the normal UV interaction with photosensitive centers and through the stress-optic contribution to the glass relaxation after UV exposition. Various FBG spectra are achieved by adjusting the excitation frequency of the piezo-electric transducer

used to generate the acoustic wave in the optical fiber. Fabry-Perot interferometers and resonant cavities, including distributed feedback (DFB) lasers can also be accomplished, through the generation of phase-shifted gratings. The method of controlling the FBG writing process using acoustic waves has great potential in various applications where precise and fast control of the grating parameters is desired.

6.2.4   Viscosity measurement

By adding a dynamic temporal component to an LPG response, its sensitivity to external medium is enhanced, turning the LPG sensitive to more challenging parameters such as the viscosity. Nevertheless, a threshold seems to limit the accuracy for viscosity measurements. However, using frequency based measurements the onset of the threshold can be avoided to provide a strong linear response over a very wide viscosity range. On the other hand, greater resolution and sensitivity is possible for viscosities above this threshold if the full relaxation time is measured. The proposed sensor is compact and based on a simple source/detector optical interrogation with a highly linear response; a full system can be readily integrated into a small unit. This technique is much cheaper and simpler than the technique based on the analysis of spectral measurements where temporal synchronization issues need to be considered. The compact dip-style sensor reported in this thesis has the potential for real-time monitoring of chemical reactions and more complex processes, such as measurements of blood properties and food engineering applications. The time analysis shows that the sensor has two linear regimes of possible operation – the regime of the initial excitation rise time and the regime that follows the mechanical relaxation when the standing wave is established. Both can be calibrated to provide a direct measure of the viscosity. Further, a simple optical power interrogation technique as a function of time permits a cheap and ready implementation of the sensor in contrast to many current applications using LPGs. Finally, the viscometer design also allows a number of sensors to be potentially multiplexed to provide distributed viscosity measurements that may be of use in a number of industrial processes where rapid and simultaneous assessment of the viscosity distribution profile is important.

6.3   FINAL CONSIDERATIONS AND FUTURE WORK

This thesis has shown the design, development and performance of a variety of all fiber devices, where the main principle of functionality is based upon the acousto-optic effect

applied to diffraction gratings. Even though the basic principle was proved to be efficient for practical applications, more detailed characterization, using new multiphysics modeling computer software and alternative techniques have to be performed, and prototypes for commercial applications have to be technologically advanced.

Regarding the add-drop multiplexer and the chromatic dispersion compensator, where FBGs were used, different gratings should be tested in order to achieve the most suitable for WDM applications. Likewise, the viscosity sensor can be further developed, though prototype optimization and miniaturization using micro and nano fibers for biological sensing.

The novel method designed for controlling the grating properties during the writing process can be further developed to systems where no masks are used, i.e. the acoustic wave can be used to change the photo induced index modulation of the grating.

7 PUBLICATIONS RELATED WITH THE THESIS

7.1 ARTICLES IN SCIENTIFIC JOURNALS

OLIVEIRA, R. A., CANNING, J., COOK, K., NASHQBANDI, M., POHL, A. A. P. "Compact dip-style viscometer based on the acousto-optic effect in a long period fiber grating," **Sensors and Actuators B: Chemical**, doi:10.1016/j.snb.2011.05.035, 2011.

NEVES JR, P. T., BAVASTRI, C. A., PEREIRA, J. T., OLIVEIRA, R. A., POHL, A. A. P., BONI, D. A., LUERSEN, M. A. "Fiber Bragg grating tuning with notch type spring device," Accept to **Measurement Science and Technology**, 2011.

OLIVEIRA, R. A., POSSETTI, G. R. C., MARQUES, C. A. F., NEVES JR, P. T., COOK, K., KAMIKAWACHI, R. C., BAVASTRI, C. A., FABRIS, J. L., MULLER, M., NOGUEIRA, R. N., CANNING, J., POHL, A. A. P. "Control of the long period grating spectrum through low frequency flexural acoustic waves," **Measurement Science & Technology**, 22, 045205, p. 1-6, 2011.

MARQUES, C. A. F., OLIVEIRA, R. A., POHL, A. A. P., CANNING, J., NOGUEIRA, R. N. "Dynamic control of a phase-shifted FBG through acousto-optic modulation," **Optics Communications**, 284, p. 1228-1231, 2011.

OLIVEIRA, R. A., COOK, K., CANNING, J., POHL, A. A. P. "Bragg grating writing in acoustically excited optical fiber," **Applied Physics Letters**, 97, p. 041101, 2010.

OLIVEIRA, R. A., NEVES JR, P. T., PEREIRA, J. T., CANNING, J., POHL, A. A. P. "Vibration mode analysis of a silica horn fiber Bragg grating device," **Optics Communications**, 283, p. 1296-1302, 2010.

OLIVEIRA, R. A., NEVES JR, P. T., PEREIRA, J. T., POHL, A. A. P. "Numerical approach for designing a Bragg grating acousto-optic modulator using the finite element and the transfer matrix methods," **Optics Communications**, 281, p. 4899-4905, 2008.

7.2 COMPLETE WORKS PUBLISHED IN PROCEEDINGS OF CONFERENCES

OLIVEIRA, R. A., MARQUES, C. A. F., COOK, K., CANNING, J., NOGUEIRA, R. N., POHL, A. A. P. "Inscription of Bragg gratings using flexural acoustic waves," **Proceedings of ECOC 2011**, Geneva, Swiss, 2011.

SILVA, R. E., OLIVEIRA, R. A., FRANCO, M. A. R., POHL, A. A. P. "Influência da microestrutura em propriedades acusto-ópticas de fibra de cristal fotônico," **Anais do SBrT 2011**, Curitiba, Pr, Brasil, 2011.

148

OLIVEIRA, R. A., POSSETTI, G. R. C., MARQUES, C. A. F., NEVES JR, P. T., COOK, K., KAMIKAWACHI, R. C., BAVASTRI, C. A., FABRIS, J. L., MULLER, M., NOGUEIRA, R. N., CANNING, J., POHL, A. A. P. "Acousto-optic control of the LPG spectrum for sensing applications," **Proceedings of SPIE (OFS 21) 7753**, 77538Y, Ottawa, Canada, 2011.

SILVA, R. E., OLIVEIRA, R. A., POHL, A. A. P. "Fiber Fabry-Perot interferometer sensor for measuring resonances of piezoelectric elements," **Proceedings of SPIE (OFS 21) 7753**, 775319, Ottawa, Canada, 2011.

MARQUES, C. A. F., OLIVEIRA, R. A., CANNING, J., NOGUEIRA, R. N, POHL, A. A. P. "Controlling the properties of fibre Bragg gratings based on the Acousto-optic modulation. **Proceedings of EUROCON and CONFTELE 2011**, Lisbon, Portugal, 2011.

MARQUES, C. A. F., OLIVEIRA, R. A., POHL, A. A. P., ANDRÉ, P. S., NOGUEIRA, R. N. "Adaptive gain equalization on optical amplifiers based on the acousto-optic effect using a single long period grating," **Proceedings of EUROCON and CONFTELE 2011**, Lisbon, Portugal, p. 1-3, 2011.

MARQUES, C. A. F., MELO, L., OLIVEIRA, R.A., POHL, A. A. P. ANDRÉ, P. S., NOGUEIRA, R. N. "Adaptive gain equalization on optical amplifiers based on the acousto-optic modulation using a long period grating," **Proceedings of International Conference on Applications of Optics and Photonics (AOP2011)**, Braga , Portugal, 2011.

OLIVEIRA, R. A., CANNING, J., NASHQBANDI, M., COOK, K., POHL, A. A. P. "Design of a viscosity sensor using a long period grating acousto-optic modulator," **Proceedings of Asia-Pacific Optical Fiber Sensors (APOS 2010)**, Guangzhou, China (*Best student paper*), 2010.

OLIVEIRA, R. A., COOK, K., CANNING, J., POHL, A. A. P. "Bragg grating writing in acoustically excited optical fiber," **Proceedings of Bragg Gratings, Photosensitivity, and Poling in Glass Waveguides (BGPP 2010)**, OSA Technical Digest, Karlsruhe, Germany, BMA4, 2010.

OLIVEIRA, R. A., COOK, K., CANNING, J., POHL, A. A. P. "Controlling the properties of fiber Bragg gratings by using acoustic waves," **Proceedings of Bragg Gratings, Photosensitivity, and Poling in Glass Waveguides (BGPP 2010)**, OSA Technical Digest, Karlsruhe, Germany, JThA48, 2010.

MARQUES, C. A. F., OLIVEIRA, R. A., POHL, A. A. P., CANNING, J., NOGUEIRA, R. N. "Tunable optical notch filter based on the acousto-optic effect in a FBG," **Proceedings of Bragg Gratings, Photosensitivity, and Poling in Glass Waveguides (BGPP 2010)**, OSA Technical Digest, Karlsruhe, Germany, BTuC5, 2010.

MARQUES, C. A. F., OLIVEIRA, R. A., CANNING, J., POHL, A. A. P., NOGUEIRA, R. N. "Control of the properties of fiber Bragg gratings based on the acousto-optic effect,"

Proceedings of 36th European Conference and Exhibition on Optical Communication (ECOC 2010), Torino, Italy, p. 1-3, 2010.

OLIVEIRA, R. A., NASHQBANDI, M., COOK, K., CANNING, J., POHL, A. A. P. "Acoustically modulated long period grating sensor for simultaneous viscosity and density measurement," **Proceedings of 4th European Workshop on Optical Fiber Sensors (EWOFS 2010)**, Porto, Portugal, 7653, p. 76530Y, 2010.

POHL, A. A. P., OLIVEIRA, R. A., MARQUES, C. A. F., COOK, K., NOGUEIRA, R. N., CANNING, J. "Novel applications of the acousto-optic effect in the control of fiber Bragg grating parameters," **Proceedings of 12th International Conference on Transparent Optical Networks (ICTON 2010)**, Munich, Germany, Mo.C1.4, p. 1-4, 2010.

OLIVEIRA, R. A., CANNING, J., POHL, A. A. P. "Acousto-optic effect in fibre Bragg gratings" **Joint Japan-Australia Workshop on Frontier Photonics and Electronics Technologies**, University of NSW, Sydney, Australia, 2010.

COOK, K., OLIVEIRA, R. A., CANNING, J., POHL, A. A. P. "Complex Bragg grating writing in acoustically excited optical fiber," **Australian Conference on Optical Fibre Technology (ACOFT/AIP 2010)**, Melbourne, Australia, 2010.

OLIVEIRA, R. A., CANNING, J., NASHQBANDI, M., COOK, K., POHL, A. A. P. "Dip-style viscometer based on acoustic wave excitation of long period fibre grating," **Australian Conference on Optical Fibre Technology (ACOFT/AIP 2010)**, Melbourne, Australia, 2010.

OLIVEIRA, R. A., MAYER, C. E. N., PEREIRA, J. T., POHL, A. A. P. "Fiber Bragg grating compression-based tuning device for reconfigurable OADM," **Proceedings of the International Telecommunications Symposium (ITS 2010)**, Manaus, Amazonas, Brazil, 2010.

NEVES JR, P. T., MORAES, G. O., OLIVEIRA, R. A., POSSETTI, G. R. C., POHL, A. A. P., BAVASTRI, C. A. "Combinação dos métodos modos assumidos e matriz de transferência em moduladores acusto-ópticos baseados em redes de período longo," **Anais do MOMAG 2010**, Vila Velha, Espírito Santo, Brazil, 2, p. 310-315, 2010.

OLIVEIRA, R. A., INACIO, P. L., POHL, A. A. P. "FBG filtering of SCM WDM channels with a notch type spring tuning device," **Proceedings of 16th International Conference on Telecommunications (ICT 2009)**, Marrakech, Marroco, King's College London, 1, p. 367-371, 2009.

OLIVEIRA, R. A., MARQUES, C. A. F., NOGUEIRA, R. N., CANNING, J., POHL, A. A. P. "Fast acousto-optic add-drop based on fiber Bragg grating," **Annual Meeting Conference Proceedings (LEOS 2009)**, Belek-Antalya, Turkey, IEEE, 1, p. 573-574, 2009.

OLIVEIRA, R. A., MARQUES, C. A. F., MAYER, C. E. N., PEREIRA, J. T., NOGUEIRA, R. N., POHL, A. A. P. "Single device for excitation of both flexural and longitudinal acousto-

optic effects in fiber Bragg gratings," **Proceedings of Microwave and Optoelectronics Conference (IMOC 2009)**, 2009 SBMO/IEEE MTT-S International, Belém, Pará, Brazil, 1, p. 546-549. 2009.

MAYER, C. E. N., OLIVEIRA, R. A., POHL, A. A. P. "Interrogação de redes de Bragg utilizando laser e medidor de potência óptica integrados via LabView," **Anais do Seminário de Iniciação Científica e Tecnológica da UTFPR (SICITE 2009)**, Curitiba, 1, 2009.

MAYER, C. E. N., OLIVEIRA, R. A., POHL, A. A. P. "Sistema de interrogação de redes de Bragg usando laser sintonizável," **Anais do 17° Simpósio Internacional de Iniciação Científica (SIICUSP 2009)**, São Paulo, USP, p. 1-1, 2009.

POHL, A. A. P., NEVES JR, P. T., OLIVEIRA, R. A., STEVESON, M., GROOTHOFF, N., CANNING, J. "Technique for estimating the tuning speed of fiber Bragg gratings," **Proceedings of SPIE 2008**, Perth, Australia, 70041I, p. 72-75, 2008.

OLIVEIRA, R. A., NEVES JR, P. T., POHL, A. A. P., MAIA, J. M., CANNING, J. "Modulação da refletividade de redes de Bragg usando interação acusto-óptica de baixa frequência," **Anais do MOMAG 2008**, Florianópolis, Brazil, 1, p. 396-398, 2008.

NEVES JR, P. T., OLIVEIRA, R. A., POHL, A. A. P., BELTRAO, P. A. C., LUERSEN, M. A., BAVASTRI, C. A. "Sintonização de redes de Bragg usando mola de entalhe," **Anais do MOMAG 2008**, Florianópolis, Brazil, 1, p. 774-776, 2008.

NEVES JR, P. T., BAVASTRI, C. A., OLIVEIRA, R. A., POHL, A. A. P. "Combinação dos métodos dos modos assumidos e matriz de transferência em dispositivos ópticos baseados em redes de Bragg sob deformação longitudinal," **Anais do XXVI Simpósio Brasileiro de Telecomunicações (SBrT 2008)**, Rio de Janeiro, Brazil, 1, p. 1-6, 2008.

7.3 PATENTS

OLIVEIRA, R. A., POHL, A. A. P., CANNING, J., COOK, K., "Viscômetro baseado em rede de Bragg ou em rede de período longo em fibra óptica," **Depositado junto à Agência de Inovação da Universidade Tecnológica Federal do Paraná**, 2011.

POHL, A. A. P., NEVES JR, P. T., OLIVEIRA, R. A., LUERSEN, M. A., BAVASTRI, C. A., PEREIRA, J. T., BELTRÃO, P. A. C. "Sintonizador de rede de Bragg em fibra óptica com mola de entalhe" **Instituto Nacional de Propriedade Industrial (INPI)**, PI0901888-3 A2, depositado em 28/05/2009, publicado em 25/01/2011.

REFERENCES

ABRISHAMIAN, F., SATO, S., IMAI, M. "A new method of solving multimode coupled equations for analysis of uniform and non-uniform fiber Bragg gratings and its application to acoustically induced superstructure modulation," **Optical Review**, 12 (6), p. 467-471, 2005.

ALLSOP, T., EARTHROWL, T., REEVES, R., WEBB, D. J., BENNION, I. "The interrogation and multiplexing of long period grating curvature sensors using a Bragg grating based, derivative spectroscopy technique," **Measurement Science and Technology**, 15, p. 44-48, 2004.

ALLSOP, T., GILLOOLY, A., MEZENTSEV, V., EARTHGROWL-GOULD, T., NEAL, R., WEBB, D. J., BENNION, I. "Bending and orientational characteristics of long period gratings written in D-shaped optical fiber," **IEEE Transactions on Instrumentation and Measurement**, 53 (1), p. 130-135, 2004.

ANDERSON, D. Z., MIZRAHI, V., ERDOGAN, T., WHITE, A. E. "Production of in-fibre gratings using a diffractive optical element," **Electronics Letters**, 29, p. 1659-1660, 1993.

ASHTON, B., CANNING, J. "DC-only Apodisation of Fibre Bragg Gratings," **Proceedings of Australian Conference on Optical Fibre Technology (ACOFT 2002)**, Darling Harbor Sydney, Australia, 2002.

ASHTON, B., CANNING, J., GROOTHOFF, N. "Two-Point Source Interferometric Grating Writing," **Applied Optics**, 43 (15), p. 3140-3144, 2004.

BALL, G. A., GLENN, W. H. "Design of a single-mode linear-cavity erbium fiber laser utilizing Bragg reflectors," **Journal of Lightwave Technology**, 10, p. 1338-1343, 1992.

BARBER, E. M., MUENGER, J. R., VILLFORTH Jr., F. J. "High rate of shear rotational viscometer," **Analytical Chemistry**, 27 (3), p 425-429, 1955.

BEARDS, C. F. "Structural vibration – analysis and damping," **Arnold**, London, 1996

BERTHOLDS, A., DÄNDLIKER, R. "Determination of the individual strain-optic coefficients in single-mode optical fibres," **Journal of Lightwave Technology**, 6 (1), p. 17-20, 1988.

BETZ, D. C., THURSBY, G., CULSHAW, B., STASZEWSKI, W. J. "Acousto-ultrasonic sensing using fiber Bragg gratings," **Smart Materials and Structures**, 12, p. 122-128, 2003.

BHATIA, V. "Applications of long-period gratings to single and multi-parameter sensing," **Optics Express**, 4, p. 457-466, 1999.

BHATIA, V., CAMPBELL, D. K., SHERR, D., D'ALBERTO, T. G., ZABARONICK, N. A., TENEYCK, G. A., MURPHY, K. A., CLAUS, R. O. "Temperature-insensitive and strain insensitive long-period grating sensors for smart structures," **Optical Engineering**, 36, p. 1872-1876, 1997.

BHATIA, V., VENGSARKAR, A. M. "Optical fiber long-period grating sensors," **Optics Letter**, 21 (9), p. 692-694, 1996.

BIDLACK, V. C., FASIG, E. W. "Paint and varnish production," **John Wiley and Sons**, New York, USA, 1951.

BIRKS, T. A., RUSSELL, P. ST. J., PANNELL, C. N. "Low power acousto-optic device based on a tapered single mode fiber," **IEEE Photonics Technology Letters**, 6 (6), p. 725-727, 1994.

BLAKE, J. N., KIM, B. Y., ENGAN, H. E., SHAW, H. J. "Analysis of intermodal coupling in a two-mode fiber with periodic microbends," **Optics Letters**, 12 (4), p. 281-283, 1987.

BLAKE, J. N., KIM, B. Y., SHAW, H. J. "Fiber-optic modal coupler using periodic microbending," **Optics Letters**, 11 (3), p. 177-179, 1986.

BLOCK, U. L., DANGUI, V., DIGONNET, M. J. F., FEJER, M. M. "Origin of apparent resonance mode splitting in bent long-period fiber gratings," **Journal of Lightwave Technology**, 24 (2), p. 1027-1034, 2006.

BORELLI, N., MILLER, R. "Determination of the individual strain-optic coefficients of glass by an ultrasonic technique," **Applied Optics**, 7, p. 745-750, 1968.

BORN, M., WOLF, E. "Principles of Optics," **Pergamon Press**, Oxford, England, 6º Ed., chap. 12, p. 593, 1980.

BOURNE, M. C. "Food texture and viscosity: concept and measurement," **Academy Press**, London, UK, 2002.

BRILLOUIN, L. "Diffusion de la lumière et des rayons X par un corps transparent homogène, influence de l'agitation thermique," **Annales de Physique**, 17 (88), p. 88-122, 1922.

BROWN, R. S., KOZIN, I., TONG, Z., OLESCHUK, R. D., LOOCK, H. P., "Fiber loop ring-down spectroscopy," **Journal of Chemical Physics**, 117, p. 10444-10447, 2000.

BRYAN, W. L., BRYAN, J. M. "Viscometer for in situ monitoring," **United States Patent**, 5.203.203, 1993.

BYRON, K. C., SUGDEN K., BIRCHENO, T., BENNION, I. "Fabrication of chirped Bragg gratings in photosensitive fibre," **Electronics Letters**, 29 (18), p. 1659-1660, 1993.

CANNING J. "Fiber gratings and devices for sensors and lasers," **Lasers and Photonics Reviews**, 2 (4), p. 275-289, Wiley, USA, 2008.

CHEN, T. C., FU, M. Y., "Acoustic-induced tunable wavelength in a tilted fiber Bragg grating," **Japanese Journal of Applied Physics**, 43 (2A), p. L200-L202, 2004.

CHEN, Z., CHIANG, K. S., NG, M. N., CHAN, Y. M., KE, H. "Bent long period fiber gratings for sensor applications," **Proceedings of Advanced Photonic Sensors and Applications**, Singapore, 3897, p. 94-104, 1999.

CHERRY, J. "In Protein Functionality in Foods," **ACS Symposium Series**, American Chemical Society, Washington, DC, 1981.

CHIANG, K. S., LIU, Y., NG, M. N., DONG, X. "Analysis of etched long-period fibre grating and its response to external refractive index," **Electronics Letters**, 36 (11), p. 966-967, 2000.

CULLEN, P. J., DUFFY, A. P., O'DONNELL, C. P., O'CALLAGHAN, D. J. "Process viscometry for the food industry," **Trends in Food Science & Technology**, 11 (12), p. 451-457, 2000.

DAO, T. T., YE, A. X., HUTCHISON, G., HEDMAN, K. "A High-Performance, Fully Self-Contained, Rotational Viscometer," **American Laboratory**, technical article, 2009.

DAVID, P. F., CAMPBELL, A. G. "Viscometer," **United States Patent**, 2.957.339, 1960.

DAVIS, S. S. "Rheological properties of semi-solid foodstuffs: Viscoelasticity and its role in quality control," **Journal of Texture Studies**, 4 (1), p. 15-40, 2007.

DEBYE, P., SEARS, F. W. "On the scattering of light by supersonic waves," **Proceedings of the National Academy of Sciences of the United States of America**, 18 (409), p. 409-414, 1932.

DELGADO-PINAR, M., ZALVIDEA, D., DÍEZ, A., PÉREZ-MILLÁN, P., ANDRÉS, M. V. "Q-switching of an all-fiber laser by acousto-optic modulation of a fiber Bragg grating," **Optics Express**, 14 (3), p. 1106-1112, 2006.

DIEZ, A., DELGADO-PINAR, M., MORA, J., CRUZ, J. L., ANDRÉS, M. V. "Dynamic fiber-optic add-drop multiplexer using Bragg gratings and acousto-optic-induced coupling", **IEEE Photonics Technology Letters**, 15 (1), 2003.

DIMMICK, T., KAKARANTZAS, G., BIRKS, T. A., RUSSELL, P. ST. J. "Narrow-band acousto-optic tunable filter fabricated from highly uniform tapered optical fiber," **Optical Fiber Communication Conference, OSA Technical Digest Series**, (Optical Society of America), paper FB4, 2000.

EGGLETON, B. J., KRUG, P. A., POLADIAN, L., OUELLETE, F. "Long Periodic Superstructure Gratings in Optical Fibres," **Electronics Letters**, 30, p. 1620-1622, 1994.

ELMORE, W. C., HEALD M. A. "Physics of Waves," **Dover**, New York, 1985.

ENGAN, H. E., KIM, B. Y., BLAKE, J. N., SHAW, H. J. "Optical frequency shifting in two-mode optical fibers by flexural acoustic waves," **IEEE Ultrasonic Symposium**, p.435-438, 1986.

ENGAN, H. E., KIM, B. Y., BLAKE, J. N., SHAW, H. J. "Propagation and optical interaction of guided acoustic waves in two-mode optical fibers," **Journal of Lightwave Technology**, 6 (3), p. 428-436, 1988.

ERDOGAN, T. "Fiber grating spectra," **Journal of Lightwave technology**, 15 (8), p. 1277-1294, 1997.

EWINS, D. J. "Modal testing: theory, practice and application," **Exeter: Research Studies Press LTD**, United Kingdom, 2000

FALATE, R., KAMIKAWACHI, R. C., MULLER, M., KALINOWSKI, H. J., FABRIS, J. L. "Fiber optic sensors for hydrocarbon detection," **Sensors and Actuators B: Chemical**, 105 (2), p. 430-436, 2005.

FARONE, W.A., SACHER, R. F., FLECK, C. "Acoustic viscometer and method of determining kinematic viscosity and intrinsic viscosity by propagation of shear waves," **United States Patent**, 6.439.034, 2002.

FERRARIS, C. F. "Measurement of the Rheological Properties of High Performance Concrete: State of the Art Report," **Journal of Research at the National Institute of Standards and Technology**, 104 (5), p. 461-478, 1999.

GIRUTS, E. L., KOPYLOV, S. M. "Emission spectra of dye lasers which use acoustooptic tuning" **Journal of Applied Spectroscopy**, 54 (5), p. 454-458, 1991.

GOTTLIEB, M. S., IRELAND, C. L. M., LEY, J. M. "Electro-optic and acousto-optic scanning and deflection**," Marcel Dekker, Inc.,** New York, 1983.

GOTTLIEB, M. S., MELAMED, N. T., GOODELL, J. B. "Rapid spectral analysis using acousto-optical devices," **Proceedings of SPIE**, 1704, p. 168-179, 1992.

GUAN, B. O., TAM, H. Y., HO, S. L., LIU, S. Y., DONG, X. Y. "Growth of long-period gratings in H_2-loaded fibre after 193 nm UV inscription," **IEEE Photonics Technology Letters**, 12, p. 642-644, 2000.

HAAKESTAD, M. W., ENGAN, H. E. "Acoustooptic properties of a weakly multimode solid core photonic crystal fiber," **Journal of Lightwave Technology**, 24 (2), p. 838-845, 2006.

HAND, D. P., RUSSELL, P. ST. J. "Photoinduced refractive-index changes in germanosilicate fibers," **Optics Letters**, 15, p. 102-104, 1990.

HENSON, W. A., TABER, D. A., BRADFORD, E. B. "Mechanism of film formation of latex paint," **Industrial & Engineering Chemistry Research**, 45 (4), p. 735-739, 1953.

HILL, K. O., FUJII, Y., JOHNSON, D. C., KAWASAKI, B. S. "Photosensitivity in optical fiber waveguides: Application to reflection filter fabrication," **Applied Physics Letters**, 32, p. 647-649, 1978.

HILL, K. O., MALO, B., BILODEAU, F., JOHNSON, D. C. "Photosensitivity in optical fibers," **Annual Review of Materials Research**, 23, p. 125-157, 1993a.

HILL, K. O., MALO, B., BILODEAU, F., JOHNSON, D. C., ALBERT, J. "Bragg gratings fabricated in monomode photosensitive optical fiber by UV exposure through a phase mask," **Applied Physics Letters**, 62, p. 1035-1037, 1993b.

HILL, K. O., MELTZ, G. "Fiber Bragg grating technology fundamentals and overview," **Journal of Lightwave Technology**, 15 (8), p. 1263-1276, 1997.

HILL, P., CANNING, J., SCEATS, M. G., EGGLETON, B. J. Unpublished work, 1994.

HOCKER, G. B. "Fiber-optic sensing of pressure and temperature," **Applied Optics**, 18, p. 1445-1448, 1979.

HOSONO, H., ABE, Y., KINSER, D. L., WEEKS, R. A., MUTA, K. "Nature and origin of the 5-eV band in $SiO_2:GeO_2$ glasses," **Physics Review B**, 46, p. 11445-11451, 1992.

HUANG, D. W., LIU, W. F., WU, C. W., YANG, C. C. "Reflectivity-tunable fiber Bragg grating reflectors," **IEEE Photonics Technology Letters**, 12, p. 176-178, 2000.

HUBNER, J., ZAUNER, D., KRISTENSEN, M. "Strong sampled Bragg gratings for WDM applications," **IEEE Photonics Technology Letters**, 10 (4), p. 552-554, 1998.

HUGHES, T. J. R., "The Finite Element Method – Linear Static and Dynamic Finite Element Analysis," **Englewood Cliffs**, NJ, Prentice-Hall, 1987.

IOCCO, A., LIMBERGER, H. G., SALATHÉ, R. P. "Bragg grating fast tunable filter," **Electronics Letters**, 33 (25), p. 2147-2148, 1997.

IRANY, E. P. "Capillary viscometer," **United States Patent**, 2.343.061, 1944.

JAFFE, H. "Piezoelectric ceramics," **Journal of the American Ceramic Society**, 41 (11), p. 494-498, 1958.

JAMES, S. W., DOCKNEY, M. L., TATAM, R. P. "Simultaneous independent temperature and strain measurement using in-fibre Bragg grating sensors," **Electronics Letters**, 32 (12), p. 1133-1134, 1996.

JAMES, S. W., TATAM, R. P. "Optical fibre long-period grating sensors: characteristics and application," **Measurement Science and Technology**, 14, p. R49-R61, 2003.

JAYARAMAN, V., CHUANG, Z. M., COLDREN, L. A. "Theory, design, and performance of extended tuning range semiconductor lasers with sampled gratings," IEEE **Journal of Quantum Electronics**, 29, p. 1824-1834, 1993.

JIANG, D., CHEN, X., DAI, Y., LIU, H., XIE, S. "A novel distributed feedback fiber laser based on equivalent phase shift," **IEEE Photonics Technology Letters**, 16 (12), p. 2598-2600, 2004.

KAMIKAWACHI R. C. "Dispositivos sensores em fibra para uso em refratometria," **Federal University of Technology – Paraná**, PhD thesis, Brazil, 2007.

KASHYAP, R. "Fiber Bragg Gratings," **Academic Press**, United Kingdom, 1999.

KASHYAP, R., MCKEE, P. F., CAMPBELL, R. J., WILLIAMS, D. L. "Novel method of producing all fibre photoinduced chirped gratings," **Electronics Letters**, 30 (12), p. 996-998, 1994.

KAWASAKI, B. S., HILL, K. O., JOHNSON, D. C., FUJII, Y. "Narrow-band Bragg reflectors in optical fibers," **Optics Letters**, 3 (2), p.66-68, 1978.

KOGELNICK, H. "Filter response of nonuniform almost-periodic gratings," **Bell System Technical Journal**, 55, p. 109-126, 1976.

KOGELNICK, H. "Theory of optical waveguides," **Guided-Wave Optoelectronics**, T. Tamir, Ed. New York: Springer-Verlag, 1990.

KRINGLEBOTN, J. T., ARCHAMBAULT, J. L., REEKIE, L., PAYNE, D. N. "Er^{3+}:Yb^{3+}-co-doped fiber distributed-feedback laser," **Optics Letters**, 19 (24), p. 2101-2103, 1994.

KRUG, P. A., STEPHENS, T., YOFFE, G., OULLETTE, F., HILL, P., DOSHI, G. "270 km transmission at 10 Gb/s in nondispersion shifted fiber using an adjustable chirped 120 mm long fiber Bragg grating dispersion compensator," **Technical Digest Conference on Optical Fiber Communications, OFC'95**, post deadline paper PDP27, 1995.

LAM, D. K. W., GARSIDE, B. K. "Characterization of single-mode optical fiber filters," **Applied Optics**, 20, p. 440-445, 1981.

LEMAIRE, P. J., ATKINS, R. M., MIZRAHI, V., REED, W. A. "High pressure H_2 loading as a technique for achieving ultrahigh UV photosensitivity and thermal sensitivity in GeO_2 doped optical fibres," **Electronics Letters**, 29, p. 1191-1193, 1993.

LI, L. "Formulation and comparison of two recursive matrix algorithms for modeling layered diffraction gratings," **Journal of the Optical Society of America A**, 13 (5), p. 1024-1035, 1996.

LIDE, D. R. "CRC handbook of chemistry and physics," **CRC Press**, Boca Raton, FL, USA, 2008.

LIMBERGER, H. G., FONJALLAZ, P. Y., SALATHÉ, R. P., COCHET, F. "Compaction- and photoelastic-induced index changes in fiber Bragg gratings," **Applied Physics Letters**, 68, p. 3069-3071, 1996.

LIPPMAN, G. "Principe de la conservation de l'électricité," **Annales de chimie et de physique**, 24, 145, 1881.

LIU, W. F., LIU, I. M., CHUNG, L. W., HUANG, D. W., YANG, C. C. "Acoustic-induced switching of the reflection wavelength in a fiber Bragg grating," **Optics Letters**, 25 (18), p. 1319-1321, 2000.

LIU, W. F., RUSSELL, P. ST. J., DONG, L. "100% efficient narrow-band acoustooptic tunable reflector using fiber Bragg grating," **Journal of Lightwave Technology**, 16 (11), p. 1006-1009, 1998.

LIU, W. F., RUSSELL, P. ST. J., DONG, L. "Acousto-optic superlattice modulator using a fiber Bragg grating," **Optics Letters**, 22 (19), p. 1515-1517, 1997.

LUCAS, R., BIQUARD, P., "Propriétés optiques des milieux solides et liquides soumis aux vibrations elastiques ultrasonores," **Journal of Physique Radium**, 3, p. 464-477, 1932.

MALO, B., JOHNSON, D. C., BILODEAU, F., ALBERT, J., HILL K. O. "Single-excimer-pulse writing of fiber gratings by use of a zero-order nulled phase mask: grating spectral response and visualization of index perturbations," **Optics Letters**, 18 (15), p. 1277-1279, 1993.

MARQUES, C. A. F., OLIVEIRA, R. A., POHL, A. A. P., CANNING, J., NOGUEIRA R. N. "Dynamic control of a phase-shifted FBG through acousto-optic modulation," **Optics Communications**, 284, p. 1228-1231, 2011.

MEIROVITCH, L. "Elements of Vibration Analysis," **Singapore: McGraw-Hill**, 1986.

MELTZ, G., MOREY, W. W. "Bragg grating formation and germanosilicate fiber photosensitivity," **Proceedings of SPIE**, 1516, 185, p. 185-199, 1991.

MELTZ, G., MOREY, W. W., GLENN, W. H. "Formation of Bragg gratings in optical fibers by a transverse holographic method," **Optics Letters**, 14, p. 823-825, 1989.

MELTZ, G., MOREY, W. W., GLENN, W. H., FARINA, J. D. "In-fiber Bragg-grating sensors," **Proceedings of OFS·88**, paper ThBB5-1, p. 63-66, 1988.

MINARDO, A., CUSANO, A., BERNINI, R., ZENI, L., GIORDANO, M. "Response of fiber Bragg gratings to longitudinal ultrasonic waves," **IEEE Transactions on Ultrasonics, Ferroelectrics and Frequency Control**, 52 (2), p. 304-312, 2005.

MOKHTAR, M. R., GOH, C. S., BUTLER, S. A., SET, S. Y., KIKUCHI, K., RICHARDSON, D. J., IBSEN, M. "Fibre Bragg grating compression-tuned over 110nm," **Electronics Letters**, 39 (6), p. 509-511, 2003.

NAKATSUKA, H., GRISCHKOWSKY, D., BALANT, A. C. "Nonlinear picosecond-pulse propagation through optical fibers with positive group velocity dispersion," **Physical Review Letters**, 47, p. 910-913, 1981.

NEVES JR., P. T. BAVASTRI, C. A., OLIVEIRA, R. A., POHL, A. A. P. "Combinação dos métodos dos modos assumidos e matriz de transferência em dispositivos ópticos baseados em redes de Bragg sob deformação longitudinal," **Proceedings of the XXVI Simpósio Brasileiro de Telecomunicacões – SBRT 2008**, Rio de Janeiro – Brazil, 2008.

NEVES JR., P. T., "Análise temporal do espectro óptico em redes de Bragg em fibra," **Federal University of Technology – Paraná**, PhD thesis, Brazil, 2008.

NISHII, J., FUKUMI, K., YAMANAKA, H., KAWAMURA, K. "Photochemical reactions in GeO2-SiO2 glasses induced by ultraviolet irradiation: Comparison between Hg lamp and excimer laser," **Physical Review B**, 52, p. 1661-1665, 1995.

OLIVEIRA, R. A., NEVES JR., P. T., PEREIRA, J. T., POHL, A. A. P. "Numerical approach for designing a Bragg grating acousto-optics modulator using finite element and transfer matrix methods," **Optics Communications**, 281, p. 4899-4905, 2008a.

OLIVEIRA, R. A. "Simulação numérica de um modulador acusto-óptico em redes de Bragg a fibra óptica," **Federal University of Technology – Paraná**, Dissertação de Mestrado, 2008b.

OLIVEIRA, R. A., MARQUES, C. A. F., NOGUEIRA, R. N., CANNING, J., POHL, A. A. P. "Fast acousto-optic add-drop based on fiber Bragg grating," **LEOS Annual Meeting Conference Proceedings**, LEOS 09, p. 573-574, 2009a.

OLIVEIRA, R. A. MARQUES, C. A. F., MAYER, C. E. N., PEREIRA, J. T., NOGUEIRA, R. N., POHL, A. A. P. "Single device for excitation of both flexural and longitudinal acousto-optic effects in fiber Bragg gratings," **Proceedings of the Microwave and Optoelectronics Conference (IMOC 2009)**, SBMO/IEEE MTT-S International, 1., p. 546-549, Belém, Pará, Brazil, 2009b.

OLIVEIRA, R. A., NEVES JR., P. T., PEREIRA, J. T., CANNING, J., POHL, A. A. P. "Vibration mode analysis of a silica horn fiber Bragg grating device," **Optics Communications**, 283, p. 1296-1302, 2010a.

OLIVEIRA, R. A., MARQUES, C. A., CANNING, J., NOGUEIRA, R. N., POHL, A. A. P. "Tunable narrow dispersion compensation for independent CWDM channels using acousto-optic effect," **Workshop FOTONICOM/CePOF**, Atibaia, São Paulo, Brazil, 2010b.

OLIVEIRA, R. A., COOK, K., CANNING, J., POHL, A. A. P. "Bragg grating writing in acoustically excited optical fiber," **Proceedings of BGPP 2010**, 2010c.

OLIVEIRA, R. A., COOK, K., CANNING, J., POHL, A. A. P. "Bragg grating writing in acoustically excited optical fiber," **Applied Physics Letters**, 97 (1), 041101, 2010d.

OLIVEIRA, R. A., COOK, K., CANNING, J., POHL, A. A. P. "Complex Bragg grating writing in acoustically excited optical fiber," **Proceedings of ACOFT 2010**, 2010e.

OLIVEIRA, R. A., CANNING, J., NASHQBANDI, M., COOK, K., POHL, A. A. P. "Design of a viscosity sensor using a long period grating acousto-optic modulator," **Proceedings of APOS 2010**, Guangzhou – China (*Best student paper*), 2010f.

OLIVEIRA, R. A., NASHQBANDI, M., COOK, K., CANNING, J., POHL, A. A. P. "Acoustically modulated long period grating sensor for simultaneous viscosity and density measurement," **Proceedings of EWOFS 2010**, Porto – Portugal, 2010g.

OLIVEIRA, R. A., POSSETI, G. R. C., MARQUES, C. A. F., NEVER JR., P. T., COOK, K., KAMIKAWACHI, R. C., BAVASTRI, C., MULLER, M., FABRIS, J. L., CANNING, J., NOGUEIRA, R. N., POHL, A. A. P. "Control of the long period grating spectrum through low frequency flexural acoustic waves," **Measurement Science & Technology**, 22, 045205, p. 1-6, 2011.

OTHONOS, A., KALLI, K. "Fiber Bragg gratings – fundamentals and applications in telecommunications and sensing," **Artech House**, Boston, 1999.

OTHONOS, A., LEE, X., MEASURES, R. M. "Superimposed multiple Bragg gratings," **Electronics Letters**, 30 (23), p. 1972-1974, 1994.

PALDUS, B. A., HARRIS JR, J. S., MARTIN, J., XIE, J., ZAREC, R. N. "Laser diode cavity ring-down spectroscopy using acousto-optic modulator stabilization," **Journal of Applied Physics,** 82 (7), p. 3199-3204, 1997.

PALMER, A. A. "Rotational viscometers," **United States Patent**, 4.045.999, 1977.

PAYNE, E. H. "Capillary viscometer," **United States Patent**, 2.095.282, 1937.

160

PEREZ, I., CUI, H. L., UDD, E. "Acoustic emission detection using fiber Bragg gratings," **Proceedings of SPIE,** 2001.

PI, Physik Instrumente, "Piezoceramic Materials," Available in www.piceramic.com Accessed in: December 08, 2010.

POHL, A. A. P., OLIVEIRA, R. A., MARQUES, C. A., COOK, K., NOGUEIRA, R. N., CANNING, J. "Novel applications of the acousto-optic effect in the control of fiber Bragg grating parameters," **Proceedings of ICTON 2010**, invited paper, Germany, 2010.

PORTMAN JR., J. L., MARGRAF, D. J. "Piezoelectric viscometer," **United States Patent**, 4.799.378, 1989.

POUMELLEC, B., NIAY, P., DOUAY, M., BAYON, J. F. "The UV-induced refractive index grating in Ge:SiO$_2$ preforms: additional CW experiments and the macroscopic origin of the change in index," **Journal of Physics D: Applied Physics**, 29 (7), p. 1842-1856, 1996.

PRIMAK, W., POST, D. "Photoelastic constants of vitreous silica and its elastic coefficient of refractive index," **Journal of Applied Physics**, 30 (5), p. 779, 1959.

REGO, G., MARQUES, P., SANTOS, J., SALGADO, H. "arc-induced long-period grating," **Fiber and Integrated Optics**, 24 (3-4), p. 245-259, 2005.

ROY, R., SCHULZ, P. A., WALTHER, A. "Acousto-optic modulator as an electronically selectable unidirectional device in a ring laser," **Optics Letters**, 12, p. 672-674, 1987.

RUSSELL, P. ST. J. "Bragg resonance of light in optical superlattices," **Physical Review Letters**, 56 (6) p. 596-599, 1986a.

RUSSELL, P. ST. J. "Optical superlattices for modulation and deflection of light," **Journal of Applied Physics**, 59 (10) p. 3344-3355, 1986b.

RUSSELL, P. ST. J., HAND, D. P., CHOW, Y. T., POYNTZ-WRIGHT, L. J. "Optically induced creation, transformation, and organization of defects and color centers in optical fibers," **Proceedings of the International Workshop on Photoinduced Self-Organization Effects in Optical Fiber**, Quebec City, Quebec, Canada, 1516, p.47-54, 1991.

RUSSELL, P. ST. J., LIU, W. F., "Acousto-optic superlattice modulation in fiber Bragg gratings," **Journal of the Optical Society of America A**, 17 (8), p. 1421-1429, 2000.

SANO, Y., YOSHINO, T. "Fast optical wavelength interrogator employing arrayed waveguide grating for distributed fiber Bragg grating sensors," **Journal of Lightwave Technology**, 21, p. 132-139, 2003.

SCEATS, M. G. Private communication with J. Canning, 1994.

SHIMA K., HIMENO K., SAKAI T., OKUDE S., WADA, A. "A novel temperature-insensitive long-period grating using a boron-codoped germanosilicate core-fibre," **Technical Digest OFC'97**, p 347-348, 1997.

SILVA, R. E., OLIVEIRA, R. A., POHL, A. A. P. "Fiber Fabry-Perot interferometer sensor for measuring resonances of piezoelectric elements," **Accepted to Optical Fiber Sensors Conference - OFS 21**, Ottawa, Canada, 2011.

SRIVASTAVA, N., DAVENPORT, R. D., BURNS, M. A., "Nanoliter viscometer for analyzing blood plasma and other liquid samples," **Analytical Chemistry**, 77, p. 383-392, 2005.

STARK, J. H., LAMBIEL, J. C., JUNGO, M. "Capillary viscosimeter," **United States Patent**, 3.864.962, 1975.

SUGDEN, K., ZHANG, L., WILLIAMS, J. A. R., FALLON, R. W., EVERALL, L. A., CHISHOLM, K. E., BENNION, I. "Fabrication and characterization of bandpass filters based on concatenated chirped fiber gratings," **Journal of Lightwave Technology**, 15 (8), p. 1424-1432, 1997.

SUSUKI, O., ISHIWATA, S., HAYASHI, M., OSHIMA, H. "Vibration type rheometer apparatus," **United States Patent**, 4.941.346, 1990.

SUTTERBY, J. L. "Falling sphere viscometer," **Journal of Physics E: Scientific Instruments**, 6, p. 1001-1005, 1973.

TAN, K. M., TAY, C. M., TJIN, S. C., CHAN, C. C., RAHARDJO, H., "High relative humidity measurements using gelatin coated long-period grating sensor". **Sensors and Actuators B: Chemical**, 110, p. 335-341, 2005.

THURSTON, R. N. "Elastic waves in rods and clad rods," **Journal of the Acoustical Society of America**, 64 (1), p. 1-37, 1978.

TREACY, E. B. "Optical pulse compression with diffraction gratings," **Quantum Electronics**, QE-5, p. 454, 1969.

TSUDA, H. "Ultrasound and damage detection in CFRP using fiber Bragg grating sensors," **Composite Science and Technology**, 66, p. 676-683, 2006.

UBBELOHDE, L. "Viscoseweter," **United States Patent**, 2.048.305, 1936.

VENGSARKAR, M., LEMAIRE, P. J., JUDKINS, J. B., BHATIA, V., ERDOGAN, T., SIPE, J. E. "Long-period fiber gratings as band-rejection filtres," **Proceedings of the Conference on Optical Fiber Communication**, Technical Digest Series, paper PD4-2, San Diego, USA, 1995.

VENGSARKAR, M., LEMAIRE, P. J., JUDKINS, J. B., BHATIA, V., ERDOGAN, T., SIPE, J. E. "Long-period fiber gratings as band-rejection filter," **Journal of Lightwave Technology**, 14, p. 58-65, 1996.

WAN X., TAYLOR H. F. "Intrinsic fiber Fabry-Perot temperature sensor with fiber Bragg grating mirrors," **Optics Letters**, 27 (16), p. 1388-1390, 2002.

WANG, Y. P., WANG, D. N., JIN, W., RAO, Y. J., PENG, G. D. "Asymmetric long period fiber gratings fabricated by use of CO_2 laser to carve periodic grooves on the optical fiber," **Applied Physics Letters**, 89 (15), p. 151105-151105-3, 2009.

WARNER, A. W., WHITE, D. L., BONNER, W. A. "Acousto-optic light deflectors using optical activity in paratellurite," **Journal of Applied Physics**, 43 (11), p. 4489-4495, 1972.

WELLER-BROPHY, L. A., HALL, D. G. "Analysis of waveguide gratings: Application of Rouard's method," **Journal of the Optical Society of America A**, 2, p. 863-871, 1985.

WRIGHT, H. A. "Viscometer," **United States Patent**, 4.627.272, 1986.

XU, M. G., ARCHAMBAULT, J. L., REEKIE, L., DAKIN, J. P. "Discrimination between strain and temperature effects using dual-wavelength fibre grating sensors," **Electronics Letters**, 30 (13), p. 1085-1087, 1994.

XU, M. G., DONG, L., REEKIE, L., TUCKNOTT, J. A., CRUZ, J.L. "Temperature-independent strain sensor using a chirped Bragg grating in a tapered optical fibre," **Electronics Letters**, 31 (10), p. 823-825, 1995.

XU, M. G., REEKIE, L., CHOW, Y. T., DAKIN, J. P. "Optical in fibre grating high pressure sensor" **Electronics Letters**, 29 (4), p. 398-399, 1993.

YAMADA, M., SAKODA, K. "Analysis of almost-periodic distributed feedback slab waveguides via a fundamental matrix approach," **Applied Optics**, 26 (16), p. 3474-3478, 1987.

YARIV, A. "Coupled-mode theory for guided-wave optics," **IEEE Journal of Quantum Electronics**, QE-9, p. 919-933, 1973.

YARIV, A., YEH, P. "Optical waves in crystals," **John Wiley & Sons, Inc**, New York, 1984.

YEOM, D. I., STEINVURZEL, P., EGGLETON, B. J., LIM, S. D., KIN, B. Y. "Tunable acoustic gratings in solid-core photonic bandgap fiber," **Optics Express**, 15 (6), p. 3513-3518, 2007.

ZEMON, S. A., DAKSS, M. L. "Acoustoptic modulator for optical fiber waveguides," **United States Patent**, 4.068.191, 1978.

ZIENKIEWICZ, O. C., TAYLOR, R. L. "The finite element method," **The Basis**, vol. 1, Oxford, Butterworth-Heinemann, 2000.

APPENDIX A – The method of assumed modes

A.1   THE LAGRANGE'S EQUATIONS

The method of assumed modes is a technique developed for studying the behavior of geometrically complex mechanical systems submitted to dynamic conditions. It has been mainly applied in the analysis of vibrations in structural engineering (BEARDS, 1996). A length of optical fiber at rest can be considered as a thin cylindrical, linear, homogeneous bar. However, when it is longitudinally pulled or compressed by means of external forces, its dimensions will vary. Yet, the application of such forces is usually accomplished by attaching other elements to the fiber, such as hinges or horns, aggregating more masses and viscous forces to the system, turning its analysis more complex and demanding.

Generally, the modeling of dynamic and complex systems using Newton's vector approach is difficult and lengthy. Alternatively, approximated solutions can be achieved using numerical methods based on Lagrange's equations through scalar formulations. The Lagrange's equations approach has, as advantage, the neglecting of system internal forces and is based on the scalar relationships between the kinetic energy, the potential energy and the work done by non-conservative external forces.

The Lagrangean operator is defined as

$$L \equiv T - V \, , \tag{A.1}$$

where T and V are the kinetic and the potential energy, respectively.

The transition between the Newtonian vector method and the scalar-energy Lagrangean method is developed through the virtual work principle, the D'Alembert's principle and the Hamilton's principle (MEIROVITCH, 1986). With these three principles one can write the Lagrange's equations as a function of generalized coordinates, q, that allow the movement equations of the system to be found

$$\frac{d}{\partial t}\left(\frac{\partial L}{\partial \dot{q}_j} \right) - \frac{\partial L}{\partial q_j} = Q_j \, , \tag{A.2}$$

where Q_j are the generalized forces applied to the system and $\dot{q}_j = \partial q_j / \partial t$.

Assuming that the system does not suffer gyroscopic effects and does not present centrifuge forces, i.e. non rotational system, the potential energy of the system, V, is simplified to the dynamic potential energy U only.

One can write the movement equations in generalized coordinates in matricial form representing the generalized non-conservative forces (external and dissipative) through the contact forces Q_j as well as the reaction forces due to the Rayleigh viscous damping:

$$\mathcal{F} = \frac{1}{2}\sum_{i=1}^{n}\sum_{j=1}^{n}c_{ij}\dot{q}_i\dot{q}_j \,, \tag{A.3}$$

where c_{ij} generates the elements of the damping matrix.

This way, assuming $L = T - U$, the Lagrange's equations are written as

$$\frac{d}{dt}\left(\frac{\partial L}{\partial \dot{q}_j}\right) - \frac{\partial L}{\partial q_j} + \frac{\partial \mathcal{F}}{\partial \dot{q}_j} = Q_j. \tag{A.4}$$

Equation (A.4) leads to a system of differential equations in the following matrix form:

$$\mathbf{M}\{\ddot{q}(t)\} + \mathbf{C}\ \{\dot{q}(t)\} + \mathbf{K}\ \{q(t)\} = \{f(t)\}, \tag{A.5}$$

where

- $\mathbf{M} = [m_{ij}]$ is the n x n-order mass matrix;
- $\mathbf{C} = [c_{ij}]$ is the n x n-order viscous damping matrix;
- $\mathbf{K} = [k_{ij}]$ is the n x n-order stiffness matrix;
- $\{f(t)\}$ is the generalized excitation vector;
- $\{q(t)\}$ is the generalized coordinates vector.

The matrices $\mathbf{M}$, $\mathbf{C}$ e $\mathbf{K}$ are symmetric, have real elements and play an important role on the assumed modes method.

A.2   THE METHOD OF ASSUMED MODES

The method of assumed modes is based on the discretization of a system consisting of N elements and n degrees of freedom in order to find approximated solutions through numerical series. For a particular case, where movement is only observed in one direction (for example, movements originated by pulling the fiber longitudinally), one can assume that the real solution of a problem with known boundary conditions will be found through a product between a conveniently chosen spatial function and a temporal function (described through the generalized coordinate). For the case of a fiber length treated as a linear bar, if one wishes to find the space-time dependent displacement behavior, the displacement function $u(x,t)$ is obtained considering the solution as

$$u(x,t) = \sum_{j=1}^{n}\phi_j(x)q_j(t), \tag{A.6}$$

where $\phi_j(x)$ is called the trial or assumed modes function.

Equation (A.6) shows that the solution is found as a linear combination of a base in n-dimensional space. The one-dimensional strain field $\varepsilon(x,t)$, which is related to the Bragg wavelength shift, is simply found differentiating $u(x,t)$ with respect to x.

The choice of the trial function is not arbitrary. For a system of n degrees of freedom it must satisfy all boundary conditions of the problem and must be differentiable at least for half of the system order (MEIROVITCH, 1986). For example, for a system described as a bar of length l with non-uniform transversal section, fixed in one extreme and loose in the other one, an appropriated trial function could be $\phi_j(x) = \sin\left(\dfrac{(2j-1)\pi x}{2l}\right)$, with $j = 1$ to n. After choosing the trial function, the next step requires the mass, damping and stiffness matrices, as well as the generalized excitation vector, to be obtained. In order to solve (5) it is first necessary to know the density function $\rho(x)$, the area function $S(x)$ and the mass function $m(x) = \rho(x)S(x)$ along the bar.

Assuming the piece of fiber as a homogenous bar with length l, with known area and mass function, the kinetic energy T is given by

$$T = \frac{1}{2}\int_0^l m(x)\left[\frac{\partial u(x,t)}{\partial t}\right]^2 dx = \frac{1}{2}\sum_{i=1}^{n}\sum_{j=1}^{n}\dot{q}_i(t)\dot{q}_j(t)m_{ij}\,,\qquad (A.7)$$

where m_{ij} are the elements of the mass matrix and are found through the following expression

$$m_{ij} = \int_0^l m(x)\phi_i(x)\phi_j(x)dx\,.\qquad (A.8)$$

On the other hand, the dynamic potential energy is given by

$$U = \frac{1}{2}\int_0^l ES(x)\left[\frac{\partial u(x,t)}{\partial t}\right]^2 dx = \frac{1}{2}\sum_{i=1}^{n}\sum_{j=1}^{n}q_i(t)q_j(t)k_{ij}\,,\qquad (A.9)$$

where k_{ij} are the elements of the stiffness matrix and are given by

$$k_{ij} = E\int_0^l S(x)\frac{\partial\phi_i(x)}{\partial x}\frac{\partial\phi_j(x)}{\partial x}dx\,,\qquad (A.10)$$

with E as the Young's modulus. Assuming that the system is impaired by non-proportional damping, which is distributed uniformly along the bar, the elements of the damping matrix are given by

$$c_{ij} = \int_0^l \alpha\phi_i(x)\phi_j(x)dx\,,\qquad (A.11)$$

where α is the viscous damping constant.

A.3   SOLUTION FOR NON-PROPORTIONAL DAMPING

The technique for finding solutions of the real problem consists of variable transforms through some spaces or domains and reduction of the order applied in (A.5). Further, applying inverse transforms, one can obtain the solution for the real system.

System mechanics considers two basic models for the viscous damping: the proportional damping and the non-proportional damping. For the case of proportional damping, the damping matrix is assumed as a linear combination of the mass and/or stiffness matrices, i.e. $C = \alpha M + \beta K$, where α and β are real constants. It is very difficult to measure experimentally the coefficients α e β, as well as to estimate them. However, the numerical process to find solutions for the system is highly simplified since it is not necessary to work on the state space. On the other hand, in the non-proportional damping model there is only one damping coefficient to estimate and the elements of the damping matrix can be easily calculated according to (A.11). Given this condition, the non-proportional damping model is adopted for the calculations that follow.

Solutions of the problem can be found by working on the configuration, state, modal and frequency domains, as will be described next. An overview of the corresponding transformations is seen in figure 1.

A.3.1   Matricial Equation in the Configuration Space

Starting with the problem in the real domain, solutions in the configuration space are given by (A.6). It is important to note that u is a real function and represents the longitudinal displacement at point x and at the time instant t.

In the configuration space, assuming that the mass, damping and stiffness matrices are known, (A.5) is repeated here for convenience

$$M\{\ddot{q}(t)\}+C\{\dot{q}(t)\}+K\{q(t)\}=\{f(t)\}, \tag{A.13}$$

The system response of (A.6) can be separated into the transient and the steady state responses. In order to find the transient response, the homogenous solution of the matricial equation (A.13) is found by setting $f(t)=0$. Knowing the transient response along with a particular solution (the steady state response), and after applying the initial conditions, the complete solution of (A.13) is found.

The reduction of order in (A.13) is done as follows.
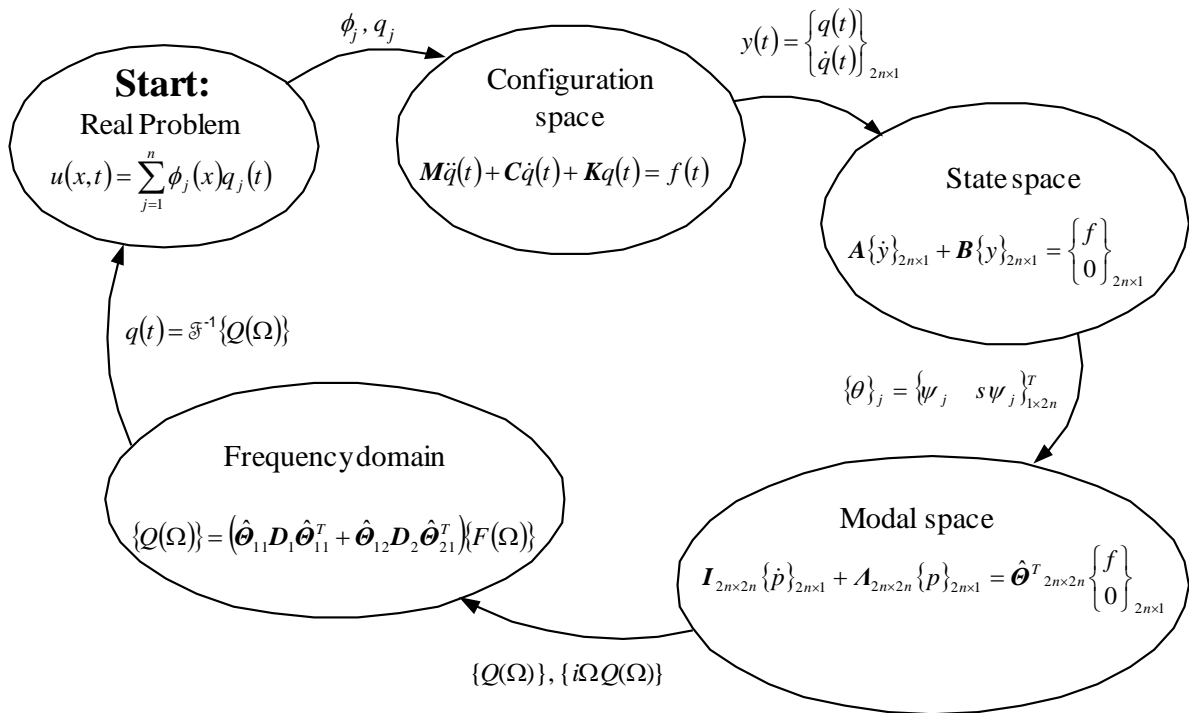
Figure A.1 - Transformation spaces used to find solutions of the displacement function in the non-proportional damping model

A.3.2   Matricial Equation in the State Space

In the configuration space the state variable is defined as

$$y(t) = \left\{ \begin{array}{c} q(t) \\ \hline \dot{q}(t) \end{array} \right\}_{2n\times 1},$$ (A.14)

where the vector $q(t)$ represents the first n elements of the vector y and $\dot{q}(t)$ represents the elements from $n+1$ to $2n$.

Writing (A.14) as

$$\left[C \vdots M \right]_{n\times 2n} \left\{ \dot{y}(t) \right\}_{2n\times 1} + \left[K \vdots \boldsymbol{0} \right]_{n\times 2n} \left\{ y(t) \right\}_{2n\times 1} = \left\{ f(t) \right\}_{n\times 1},$$ (A.15)

a system with n equations and $2n$ unknowns is obtained, where $\left[C \vdots M \right]_{n\times 2n}$ represents a matrix formed by the concatenation of the damping and mass matrices and $\left[K \vdots \boldsymbol{0} \right]_{n\times 2n}$ represents a matrix formed by the concatenation of the stiffness matrix K and a matrix with dimensions $n\times n$ formed by zeros, represented by $\boldsymbol{0}$ in (A.15).

Transforming (A.15) into a system of $2n$ equations and $2n$ unknowns requires the following tautology to be used

$$\left[M \vdots \boldsymbol{0} \right]_{n\times 2n} \left\{ \dot{y}(t) \right\}_{2n\times 1} + \left[\boldsymbol{0} \vdots -M \right]_{n\times 2n} \left\{ y(t) \right\}_{2n\times 1} = \left\{ 0 \right\}_{n\times 1}.$$ (A.16)

Equation (A.16) is true because

$$\dot{y}(t) = \left\{ \begin{array}{c} \dot{q}(t) \\ \hline \ddot{q}(t) \end{array} \right\}_{2n\times1} . \tag{A.17}$$

In other words, the first n elements of $\dot{y}(t)$ are equal to the last n elements of $y(t)$.

This way, concatenating (A.17) with (A.16) results in the matricial equation given in the state space

$$\begin{bmatrix} C & M \\ \hline M & 0 \end{bmatrix}_{2n\times2n} \{\dot{y}(t)\}_{2n\times1} + \begin{bmatrix} K & 0 \\ \hline 0 & -M \end{bmatrix}_{2n\times2n} \{y(t)\}_{2n\times1} = \left\{ \begin{array}{c} f(t) \\ \hline 0 \end{array} \right\}_{2n\times1}, \tag{A.18}$$

which can be written as

$$A_{2n\times2n}\{\dot{y}(t)\}_{2n\times1} + B_{2n\times2n}\{y(t)\}_{2n\times1} = \left\{ \begin{array}{c} f(t) \\ \hline 0 \end{array} \right\}_{2n\times1} . \tag{A.19}$$

A.3.3 Matricial Equation in the Modal Space

Setting $\{f(t)\} = 0$, one can assume the solution of the homogeneous equation as

$$y(t) = \{\theta\}_{2n\times1} e^{st} . \tag{A.20}$$

The first n elements of $\{\theta\}_{2n\times1}$ form the eigenvector ψ in the state space and the remaining rows, from $n+1$ to $2n$, form the vector $s\psi$, which are expressed as

$$\{\theta\}_{2n\times1} = \left\{ \begin{array}{c} \psi \\ \hline s\psi \end{array} \right\}_{2n\times1}, \tag{A.21}$$

Thus, (A.20) can be written as

$$[s\mathbf{A} + \mathbf{B}]\{\theta\}_{2n\times1} = \{0\}_{2n\times1} \quad \therefore \quad \mathbf{B}\{\theta\}_j = \lambda_j \mathbf{A}\{\theta\}_j, \tag{A.22}$$

where $\{\theta\}_j = \{\psi_j \vdots s\psi_j\}^T_{1\times2n}$, with $j = 1, 2,..., 2n$, and

$$\lambda_j = -s_j . \tag{A.23}$$

Note that (A.22) represents an eigenvalue problem whose solution results in $2n$ eigenvalues called λ, as well as a set of $2n$ eigenvectors θ (with dimensions $2n$ x 1) that form the matrix $\boldsymbol{\Theta}_{2n\times2n}$ called the modal matrix in the state space. Matrices A e B are symmetric and real. On the other hand, the matrix $\boldsymbol{\Theta}$ is complex and non-symmetric.

Using ortogonality properties the following relationship is satisfied

$$\tilde{A} = \boldsymbol{\Theta}^T A \boldsymbol{\Theta} = \begin{bmatrix} . & 0 & 0 \\ 0 & \tilde{a}_{kk} & 0 \\ 0 & 0 & . \end{bmatrix} . \tag{A.24}$$

As well as with the eigenfunctions, the eigenvectors can be normalized through the diagonal matrix $\tilde{A}$ forming an ortonormal set represented by the matrix $\hat{\boldsymbol{\Theta}}$ whose elements are found through the expression

$$\hat{\theta}_{jk} = \frac{\theta_{jk}}{\sqrt{\tilde{a}_{kk}}}, \tag{A.25}$$

where $\hat{\theta}$, θ and $\tilde{a}$ are elements of matrices $\hat{\boldsymbol{\Theta}}$, $\boldsymbol{\Theta}$ and $\tilde{A}$, respectively, and $j, k = 1, 2,...,2n$.

The matrix $\hat{\boldsymbol{\Theta}}$ is known as ortonormalized modal matrix and satisfies the following relationships

$$\hat{\boldsymbol{\Theta}}^T B \hat{\boldsymbol{\Theta}} = \Lambda, \tag{A.26}$$

$$\hat{\boldsymbol{\Theta}}^T A \hat{\boldsymbol{\Theta}} = I. \tag{A.27}$$

The matrix I is the identity matrix, with dimensions $2n$ x $2n$, and Λ is denominated the Spectral Matrix in the state space, having the form

$$\Lambda = \begin{bmatrix} \lambda_1 & 0 & 0 & 0 & . & 0 & 0 \\ 0 & \lambda_1^* & 0 & 0 & . & 0 & 0 \\ 0 & 0 & \lambda_2 & 0 & . & 0 & 0 \\ 0 & 0 & 0 & \lambda_2^* & . & 0 & 0 \\ . & . & . & . & . & . & . \\ 0 & 0 & 0 & 0 & . & \lambda_n & 0 \\ 0 & 0 & 0 & 0 & . & 0 & \lambda_n^* \end{bmatrix}, \tag{A.28}$$

where λ_j^* is the complex conjugate of λ_j.

From (A.23), assuming $\lambda_j = -s_j = -(\beta_j + i\gamma_j)$ and using ortogonality relationships (EWINS, 2000), it is possible to demonstrate that γ_j are the damping natural frequencies of each mode of vibration. Furthermore, the natural frequencies ω_j of the damped system are given by the absolute values of λ_j, i.e.

$$\omega_j = \sqrt{\beta_j^2 + \gamma_j^2}, \tag{A.29}$$

and the relationship between the modal damping, ξ_j, and each mode is given by

$$\xi_j = -\frac{\beta_j}{\omega_j}. \tag{A.30}$$

Once matrix $\hat{\boldsymbol{\Theta}}$ is known, one can work in the modal space using the following transformation

$$y(t) = \hat{\boldsymbol{\Theta}}\{p(t)\}_{2n\times 1}. \tag{A.31}$$

Since $y(t)$ is real and $\hat{\boldsymbol{\Theta}}$ is a complex matrix, p also must be a complex vector, which is called the Main Generalized Coordinate.

Substituting (A.31) in (A.19) results

$$A\hat{\boldsymbol{\Theta}}\{\dot{p}\}_{2n\times1} + B\hat{\boldsymbol{\Theta}}\{p\}_{2n\times1} = \left\{\begin{array}{c} f \\ \cdots \\ 0 \end{array}\right\}_{2n\times1}.$$

(A.32)

Multiplying both sides of this equation by $\hat{\boldsymbol{\Theta}}^T$ and applying the ortogonality relationship (A.26) and (A.27) one reaches the modal space where (A.32) is reduced to

$$\hat{\boldsymbol{\Theta}}^T\left(A\hat{\boldsymbol{\Theta}}\dot{p} + B\hat{\boldsymbol{\Theta}}p\right) = \hat{\boldsymbol{\Theta}}^T\left\{\begin{array}{c} f \\ \cdots \\ 0 \end{array}\right\} \quad \therefore \quad I\dot{p} + \Lambda p = \hat{\boldsymbol{\Theta}}^T\left\{\begin{array}{c} f \\ \cdots \\ 0 \end{array}\right\},$$

(A.33)

Note that (A.33) is a first order differential equation in matrix form where Λ is the spectral matrix and $\hat{\boldsymbol{\Theta}}^T$ is the transposed modal matrix.

A.3.4 Matricial Equation in the Frequency Domain

Often, in order to find the steady state solution, the transformation of the following equation system into the frequency domain is convenient

$$\{\dot{p}(t)\}_{2n\times1} + \Lambda_{2n\times2n}\{p(t)\}_{2n\times1} = \hat{\boldsymbol{\Theta}}^T{}_{2n\times2n}\{g(t)\}_{2n\times1},$$

(A.34)

where

$$\{g(t)\}_{2n\times1} = \left\{\begin{array}{c} f(t) \\ \cdots \\ 0 \end{array}\right\}_{2n\times1}.$$

(A.35)

Since the system described by (A.34) is decoupled, one can represent the total system by n discrete elements with only one freedom degree (with mass, stiffness and damping characteristics), where each element is excited by the respective frequency Ω.

This way, transforming (A.34) into the frequency domain gives

$$(i\Omega I + \Lambda)\{P(\Omega)\} = \hat{\boldsymbol{\Theta}}^T\{G(\Omega)\}.$$

(A.36)

Since $y(t) = \hat{\boldsymbol{\Theta}}\{p(t)\}$, the response in the frequency domain is

$$Y(\Omega) = \hat{\boldsymbol{\Theta}}D^{-1}\hat{\boldsymbol{\Theta}}^T\{G(\Omega)\},$$

(A.37)

where $D = i\Omega I + \Lambda$.

Eventually matrix D can become singular (e. g. when the damping is very small); in this case, it is possible to find $Y(\Omega)$ by calculating the pseudo-inverse of D.

From (A.14) the vector $Y(\Omega)$ can be written as

$$Y(\Omega) = \left\{ \frac{Q(\Omega)}{i\Omega Q(\Omega)} \right\} . \tag{A.38}$$

Matrices $\hat{\boldsymbol{\Theta}}$, $\boldsymbol{D}$, and $\hat{\boldsymbol{\Theta}}^T$ can be partitioned generating four submatrices allowing (A.37) to be described as

$$Y(\Omega) = \left\{ \frac{Q(\Omega)}{i\Omega Q(\Omega)} \right\} = \begin{bmatrix} \hat{\boldsymbol{\Theta}}_{11} & \hat{\boldsymbol{\Theta}}_{12} \\ \hat{\boldsymbol{\Theta}}_{21} & \hat{\boldsymbol{\Theta}}_{22} \end{bmatrix} \begin{bmatrix} \boldsymbol{D}_1 & \boldsymbol{0} \\ \boldsymbol{0} & \boldsymbol{D}_2 \end{bmatrix} \begin{bmatrix} \hat{\boldsymbol{\Theta}}_{11}^T & \hat{\boldsymbol{\Theta}}_{12}^T \\ \hat{\boldsymbol{\Theta}}_{21}^T & \hat{\boldsymbol{\Theta}}_{22}^T \end{bmatrix} \left\{ \frac{F(\Omega)}{0} \right\} . \tag{A.39}$$

If one wishes to find only the vector $\{Q(\Omega)\}_{n\times 1}$, the final solution is given by reducing (A.39) to

$$\{Q(\Omega)\} = \left(\hat{\boldsymbol{\Theta}}_{11} \boldsymbol{D}_1 \hat{\boldsymbol{\Theta}}_{11}^T + \hat{\boldsymbol{\Theta}}_{12} \boldsymbol{D}_2 \hat{\boldsymbol{\Theta}}_{21}^T \right) \{F(\Omega)\} . \tag{A.40}$$

Finally, the solution in the real domain is obtained through the inverse Fourier transform in order to find the vector $\{q(t)\}_{n\times 1}$, which is then applied in (A.6) to give the system displacement as a function of time.

Figure 1 shows the steps over the spaces to find $q(t)$, departing from (A.6).

Note that the methodology used to find the $q(t)$ involves transformations to intermediary spaces that have no physical meaning (for example, state space and modal space).

A.4   GENERAL RESPONSE FOR AN HARMONIC SOURCE OF EXCITATION

In order to find the transient response of the system it is first necessary to obtain the solution of the homogenous equation (A.35) assuming $f(t) = 0$. Knowing the transient and the steady state responses the solution is complete.

For instance, let us assume that the system is described as a bar of length l with non-uniform transversal section, fixed in one extreme and loose in the other one, and excited at its free end by an harmonic source dependent of time. The mathematical model of this source is represented by complex exponential functions of the form

$$f_0(t) = F(\Omega) e^{i\Omega_0 t} + F^*(\Omega) e^{-i\Omega_0 t} , \tag{A.41}$$

where $F(\Omega)$ and $F^*(\Omega)$ are the complex and complex conjugated amplitudes, respectively, and Ω_0 is the angular frequency of the signal.

A possible trial function for this system is $\phi_j(x) = \sin\left(\frac{(2n-1)\pi x}{2l} \right)$, from which one can find the generalized force

$$f_j(t) = \left(F(\Omega)_j e^{i\Omega_0 t} + F^*(\Omega)_j e^{-i\Omega_0 t} \right) \sin\left(\frac{(2n-1)\pi\, l}{2l} \right) =$$
$$= (-1)^{j-1} \left(F(\Omega)_j e^{i\Omega_0 t} + F^*(\Omega)_j e^{-i\Omega_0 t} \right)$$

(A.42)

where j is used to define the excitation point of the harmonic function.

Assuming the complex amplitude in the form of

$$F(\Omega) = \frac{F_0 - iF_0}{2},$$

(A.43)

and substituting (A.43) in (A.41) one obtains:

if
$$f(t) = F_0 \cos(\Omega_0 t) \;\Rightarrow\; F(\Omega) = \frac{F_0}{2},$$

(A.44)

and if
$$f(t) = F_0 \sin(\Omega_0 t) \;\Rightarrow\; F(\Omega) = -i\frac{F_0}{2}.$$

(A.45)

Assuming a sinusoidal source, the steady state solution in the state space is given by

$$\left\{ \begin{array}{c} q^p(t) \\ \hline \dot{q}^p(t) \end{array} \right\}_{2n\times 1} = \left\{ \begin{array}{c} Q_0(\Omega) \\ \hline i\Omega_0 Q_0(\Omega) \end{array} \right\}_{2n\times 1} e^{i\Omega_0 t} + \left\{ \begin{array}{c} Q_0^*(\Omega) \\ \hline i\Omega_0 Q_0^*(\Omega) \end{array} \right\}_{2n\times 1} e^{-i\Omega_0 t},$$

(A.46)

where the complex amplitude vector is given by

$$\left\{ \begin{array}{c} Q_0(\Omega) \\ \hline i\Omega_0 Q_0(\Omega) \end{array} \right\}_{2n\times 1} = \hat{\boldsymbol{\Theta}} \boldsymbol{D}^{-1} \hat{\boldsymbol{\Theta}}^T \left\{ \begin{array}{c} -i\dfrac{F_0}{2}(-1)^{j-1} \\ \hline 0 \end{array} \right\}_{2n\times 1},$$

(A.47)

with $\boldsymbol{D} = i\Omega_0 \boldsymbol{I} + \boldsymbol{\Lambda}$.

Therefore, the displacement function in the steady state is given by

$$u^p(x,t) = \sum_{j=1}^{n} \sin\left(\frac{(2j-1)\pi x}{2l} \right) q_j^p(t),$$

(A.48)

where $q_j^p(t)$ are the elements of the generalized coordinates vector

$$\{q^p(t)\}_{n\times 1} = \{Q_0(\Omega)\}_{n\times 1} e^{i\Omega_0 t} + \{Q_0^*(\Omega)\}_{n\times 1} e^{-i\Omega_0 t}.$$

(A.49)

The transient time solution is obtained solving the system

$$\dot{p}_j + \lambda_j p_j = 0 \quad, \quad j = 1, 2,\ldots, 2n.$$

(A.50)

The solutions of each equation of the system follow the expression

$$p_j = b_j e^{-\lambda_j t} = b_j e^{s_j t},$$

(A.51)

where $s = -\lambda$ and b_j are the elements of the vector b related to the initial conditions.

Since $y = \left\{ \begin{array}{c} q(t) \\ \dot{q}(t) \end{array} \right\}_{2n\times 1}$ and $\hat{\boldsymbol{\Theta}} = \left[\begin{array}{c} \hat{\theta} \\ s\hat{\theta} \end{array} \right]_{2n\times 2n}$, substituting (A.51) in (A.31) gives the solution

of the homogenous equation in the state space and is expressed as

$$\begin{Bmatrix} \overline{q^h(t)} \\ \dot{q}^h(t) \end{Bmatrix}_{2n\times1} = \begin{bmatrix} \hat{\theta} \\ \overline{\phantom{s\hat{\theta}}} \\ s\hat{\theta} \end{bmatrix}_{2n\times2n} \begin{bmatrix} \cdot & 0 & 0 \\ 0 & e^{-\lambda_j t} & 0 \\ 0 & 0 & \cdot \end{bmatrix}_{2n\times2n} \{b\}_{2n\times1} =$$

$$= \hat{\boldsymbol{\Theta}} \begin{bmatrix} \cdot & 0 & 0 \\ 0 & e^{-\lambda_j t} & 0 \\ 0 & 0 & \cdot \end{bmatrix}_{2n\times2n} \{b\}_{2n\times1} \qquad (A.52)$$

Thus, the displacement is achieved according to

$$u(x,t) = \sum_{j=1}^{n} \phi_j(x) q_j^p(t) + \sum_{j=1}^{n} \phi_j(x) q_j^h(t), \qquad (A.53)$$

where $q_j^h(t)$ are the elements of the vector

$$\{q^h(t)\}_{n\times1} = [\hat{\theta}]_{n\times2n} \begin{bmatrix} \cdot & 0 & 0 \\ 0 & e^{-\lambda_j t} & 0 \\ 0 & 0 & \cdot \end{bmatrix}_{2n\times2n} \{b\}_{2n\times1}. \qquad (A.54)$$

It is now necessary to apply the initial conditions in order to find the elements of the vector b in order to completely define the displacement function. Assuming that the displacement is null along the bar at the time instant $t = 0$, one obtains $e^{i\Omega_0 \cdot 0} = 1$. The displacement function can be written as

$$u(x,t) = 0 = \sum_{j=1}^{n} \phi_j(x) \left(\{Q_0(\Omega)\}_{n\times1} + \{Q_0^*(\Omega)\}_{n\times1} \right) +$$

$$+ \sum_{j=1}^{n} \phi_j(x) \left([\hat{\theta}]_{n\times2n} \{b\}_{2n\times1} \right) \qquad (A.55)$$

This way, from (A.55) we have

$$[\hat{\theta}]_{n\times2n} \{b\}_{2n\times1} = - \left(\{Q_0(\Omega)\}_{n\times1} + \{Q_0^*(\Omega)\}_{n\times1} \right). \qquad (A.56)$$

Expanding (A.56) in the state space, the right side can be replaced by (A.52) regardless of the temporal matrix. Analogously, the right side can be replaced by (A.46), which, in turn, can be simplified and results in

$$\hat{\boldsymbol{\Theta}} \{b\}_{2n\times1} = \begin{Bmatrix} -2\Re\{Q_0(\Omega)\} \\ \overline{} \\ 2\Omega_0 \Im\{Q_0(\Omega)\} \end{Bmatrix}_{2n\times1} \quad \therefore$$

$$\therefore \{b\}_{2n\times1} = \hat{\boldsymbol{\Theta}}^{-1} \begin{Bmatrix} -2\Re\{Q_0(\Omega)\} \\ \overline{} \\ 2\Omega_0 \Im\{Q_0(\Omega)\} \end{Bmatrix}_{2n\times1}, \qquad (A.57)$$

Using the property given in (A.27), it is possible to show that $\hat{\boldsymbol{\Theta}}^{-1} = \hat{\boldsymbol{\Theta}}^T A$, which is applied in (A.57) and results in

$$\{b\}_{2n\times 1} = \hat{\boldsymbol{\Theta}}^T A \left\{ \frac{-2\Re\{Q_0(\Omega)\}}{2\Omega_0\Im\{Q_0(\Omega)\}} \right\}_{2n\times 1} , \tag{A.58}$$

defining the displacement function completely.

APPENDIX B – Parameters used in the simulations

Table B.1 shows the value for the constants and coefficients used during the numerical simulations. Some of the terms had to be adjusted in order to match the grating spectrum achieved experimentally, once the simulations can be used also for calculations of some experimental parameters. For instance, a term that had to be adjusted is the fiber core UV-induced index modulation, which varies from $\delta n_{eff} = (1 \text{ to } 5) \times 10^{-4}$ depending on the laser and fiber conditions.

Simulation parameters such as number of matrices (if one considers the TMM) and number of elements (FEM) or even degrees of freedom (AMM) were set in order to provide an accurate result, taking account the computational limitations.

Table B.1 - Values for the coefficients and constants used in the numerical simulations

	Parameter	Description	Value
Constant	n_{eff}	Effective index	1,45610764539747
	p_{11}	Strain-tensor coefficients	0,121
	p_{12}		0,17
	σ	Poisson's ratio	0,17
	v	FBG fringe visibility	1
	p_e	FBG strain-optic coefficient	-0,22 nm/με
	E	Young's modulus of silica	72,9 GPa
	ρ	Silica density	2.200 g/m³
	c_{ext}	Extensional velocity in silica	5.740 m/s
	α	LPG thermal expansion coefficient	5×10^{-5} /°C
Variable	P_0	Load applied on the base of silica horn	0 – 10 N
	δn_{eff}	UV-induced index modulation	$1 - 5 \times 10^{-4}$
	l_g	Grating length	25 – 50 mm
	o	LPG thermal-optic coefficient	$2 - 4 \times 10^{-5}$ /°C
	p	LPG strain-optic coefficient	-0,5 – -0,7 nm/με
	M	Number of matrices for TMM	200 – 800
	$\kappa_{ac}l$	AC coupling coefficient $\times$ grating length	3 – 8

Figure B.1 shows the comparison between experimental and simulation spectrum considering an acoustic excitation at $f = 1,021$ MHz. The PZT was driven by $V_{PZT} = 10$ V, and, the value of the correspondent load applied on the basis of the horn was found to be $P_0 = 1$ N, which matches the experimental spectrum. Additionally, the index modulation also had to be adjusted through the product $\kappa_{ac} l_g$, in order to match the amplitude and bandwidth of the spectrum. In this case, $\delta n_{eff} = 1 \times 10^{-4}$, which corresponds to $\kappa_{ac} l_g = 6$. For comparison purposes, if the index modulation is varied from $\kappa_{ac} l_g = 2$ to 10, for instance, the spectrum is strongly modified, as one can see in figure B.2.
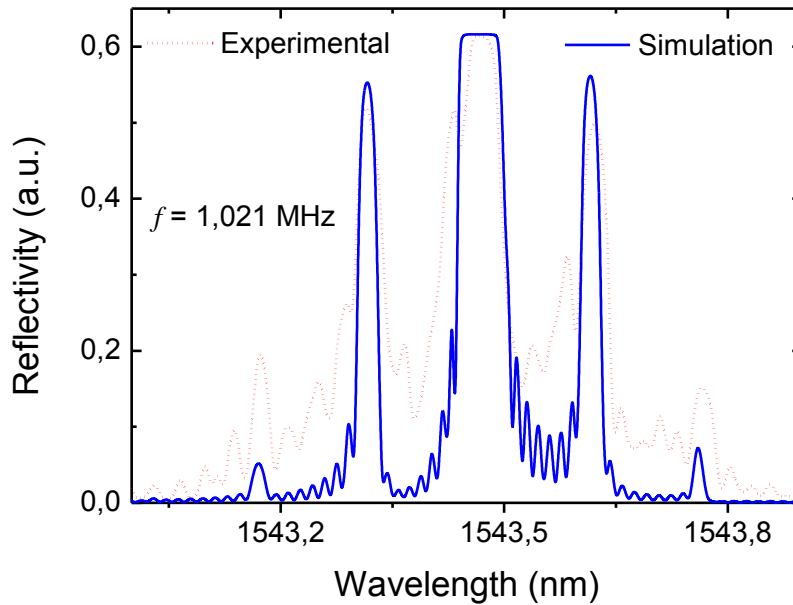
Figure B.1 - Experimental and simulated results for $f = 1,021$ MHz acoustic wave excitation.
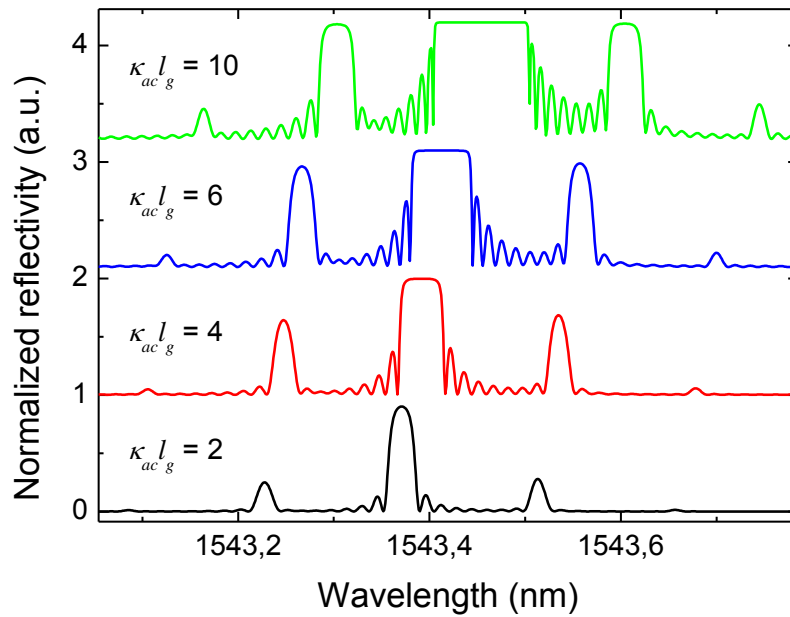
Figure B.2 - Behavior of the simulated FBG spectrum when the index modulation is varied through the product $\kappa_{ac}\, l_g$.

Another example of how the simulation parameters were adjusted to fit the experimental spectrum is given by the load applied on the base of the silica horn. Once the maximum strain achieved within the fiber varies depending on the RF frequency, different values for the load at each resonance are found. Figures B.3 (figure 4.10) and B.4 (figure 4.12) exemplifies this assertion. The maximum load achieved when the PZT is driven by $V_{PZT} = 10$ V and $f = 60,6$ kHz is $P_0 = 0,042$ N. When $f = 53,3$ kHz, the corresponding load is $P_0 = 0,06$ N.
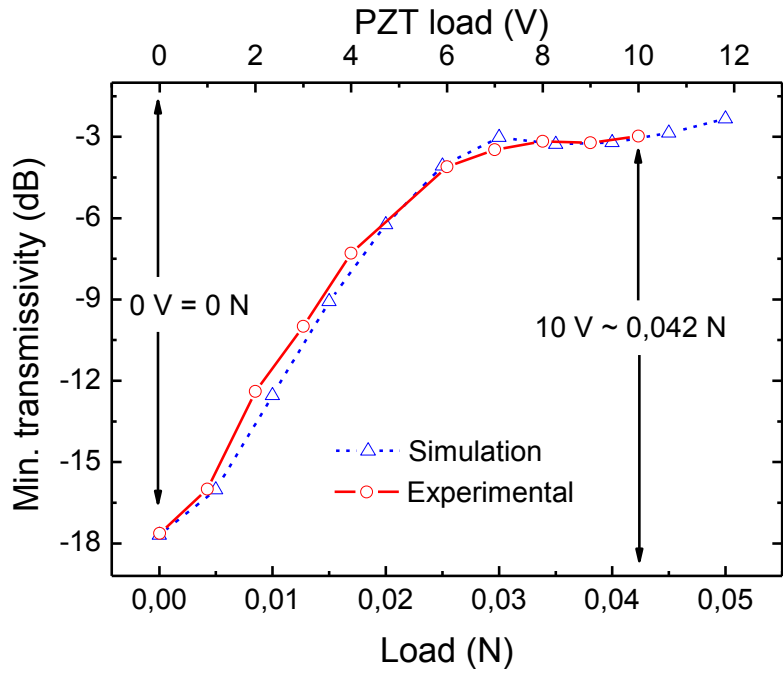
Figure B.3 - Considering f = 60,6 kHz, **the corresponding maximum load achieved through numerical simulation was** P_0 = 0,042 N.
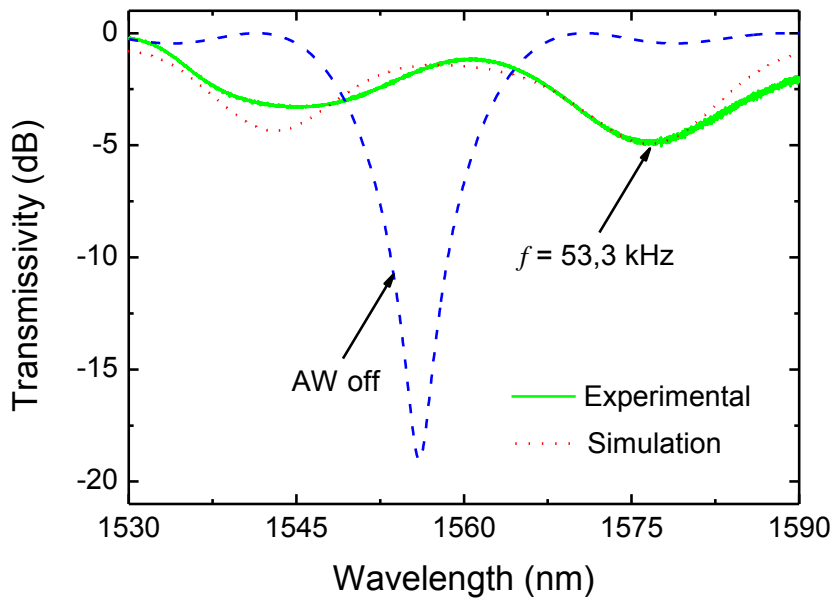

Figure B.4 - When f = 53,3 kHz **and** V_{PZT} = 10 V, P_0 = 0,06 N.